Universität Hamburg

DER FORSCHUNG | DER LEHRE | DER BILDUNG

Electron Spin Resonance Studies on Spin-Orbit Interactions in Graphene

Dissertation

zur Erlangung des Doktorgrades

an der Fakultät für Mathematik, Informatik und Naturwissenschaften

Fachbereich Physik

der Universität Hamburg

vorgelegt von

Jonas Sichau

- Hamburg, 2019 -

GUTACHTER DER DISSERTATION:

Prof. Dr. Robert H. Blick

Prof. Dr. Hans P. Oepen

ZUSAMMENSETZUNG DER PRÜFUNGSKOMMISSION:

Prof. Dr. Robert H. Blick

Prof. Dr. Hans P. Oepen

Prof. Dr. Daniela Pfannkuche

Prof. Dr. Wolfgang J. Parak

Dr. Lars Tiemann

DATUM DER DISPUTATION:

30.09.2019

VORSITZENDE DER PRÜFUNGSKOMMISSION:

Prof. Dr. Daniela Pfannkuche

VORSITZENDER DES FACH-PROMOTIONSAUSSCHUSSES PHYSIK:

Prof. Dr. Michael Potthoff

LEITER DES FACHBEREICHS PHYSIK:

Prof. Dr. Wolfgang Hansen

DEKAN DER FAKULTÄT MIN:

Prof. Dr. Heinrich Graener

Abstract

In the early years of the rise of graphene, Kane and Mele [Phys. Rev. Lett. 95, 226801 (2005)] predicted that spin-orbit interactions would induce a topological state of matter at sufficiently low energies. This spin-Hall insulating state would be gapped in the bulk, while supporting spin transport along the sample boundaries. The size of the intrinsic gap has been the subject of theoretical discussions as it has not been measured until recently. Resistively-detected electron spin resonance at low temperatures is proven to be a suitable experimental method to probe the low-energy regime in graphene by coupling charge carriers of opposite spin in an external magnetic field via microwave excitation. The observed features in the sample resistivity can be linked to the band structure of graphene, which is described by a numerical model. The size of the intrinsic spin-orbit bulk band gap of graphene is determined to be 42.2 µeV. The experiments yield indications of a phase transition from the spin-Hall insulating state to the Dirac semi-metallic state at an external magnetic field of 0.38 T. Additionally, the robustness of the g-factor of the charge carriers against variations of the sample geometry and the carrier density is confirmed. However, g shifts between values of 1.81 and 2.03 when the external magnetic field direction is altered. By employing a microscopic theory to the angular dependence of the g-factor, the mixing parameter of the p- and d-orbitals in graphene as well as the atomic spin-orbit coupling are extracted. In a separate experiment, graphene is directly placed on Pt/Co/Pt magnetic nanoparticles, which are found to enhance the features of the electron spin resonance in graphene by a factor ≥ 5 without affecting the value of the g-factor. Variations of the magnetic field angle yield indications of interactions between the microwaves and the magnetic moments of the nanoparticles, which affect the resistivity of the graphene.

Zusammenfassung

Im Zeitraum nach der experimentellen Entdeckung von Graphen sagten Kane und Mele [Phys. Rev. Lett. 95, 226801 (2005)] voraus, dass die Spin-Bahn-Wechselwirkung der Ladungsträger einen topologischen Zustand bei ausreichend geringen Energien erzeugt. Dieser isolierende Spin-Hall Zustand weist eine Bandlücke im Bulk auf, während Spin-Transport am Probenrand möglich ist. Die Größe der intrinsischen Bandlücke ist Gegenstand von theoretischen Debatten, da bis vor kurzem noch kein genauer Wert gemessen wurde. Widerstands-detektierte Elektronen-Spin-Resonanz bei Tieftemperaturen stellt sich als geeignete experimentelle Methode heraus, um den Niedrigenergie-Bereich in Graphen zu messen. Hierbei werden Ladungsträger mit entgegengesetztem Spin in einem Magnetfeld über Mikrowellenstrahlung gekoppelt. Die beobachteten Widerstandsänderungen im Graphen spiegeln die Bandstruktur wider, welche mit Hilfe eines numerischen Modells berechnet wird. Die Größe der intrinsischen Bulk-Bandlücke von Graphen wird mit 42.2 µeV bestimmt. Die Experimente lassen Rückschlüsse zu auf einen Phasenübergang vom isolierenden Spin-Hall-Zustand zum Dirac-Halbmetall-Zustand bei einem äußeren Magnetfeld von 0.38 T. Zusätzlich wird die Invarianz des g-Faktors der Ladungsträger gegenüber der Probengeometrie und der Ladungsträgerdichte gezeigt. Allerdings variiert g zwischen Werten von 1.81 bis 2.03, wenn die Richtung des äußeren Magnetfeldes geändert wird. Indem eine mikrospkopische Theorie auf die Messergebnisse der Winkelabhängigkeit des g-Faktors angewandt wird, kann sowohl der Misch-Paramter der p- und d-Orbitale in Graphen, als auch die atomistische Spin-Bahn-Wechselwirkung extrahiert werden. In einem separaten Experiment wird Graphen direkt mit Pt/Co/Pt Nanopartikeln in Kontakt gebracht, welche das Elektronen-Spin-Resonanz-Signal um einen Faktor ≥ 5 erhöhen, ohne den g-Faktor zu beinflussen. Winkeländerungen des äußeren Magnetfeldes lassen Rückschlüsse zu, die auf Wechselwirkungen zwischen der Mikrowellenstrahlung und den magnetischen Momenten der Nanopartikel hindeuten, welche wiederum den spezifischen Widerstand von Graphen beeinflussen.

Contents

Abbreviations

2D	two-dimensional
AC	alternating current
AFM	atomic force microscopy
CNP	charge neutrality point
CVD	chemical vapor deposition
DI	deionized
DOS	density of states
EBL	electron beam lithography
EG	exfoliated graphene
ESR	electron spin resonance
h-BN	hexagonal boron nitride
ISOC	intrinsic spin-orbit coupling
LDOS	local density of states
LL	Landau levels
QHE	quantum Hall effect
RD-ESR	resistively-detected electron spin resonance
SEM	scanning electron microscope
SHI	spin Hall insulator
SOC	spin-orbit coupling
VTI	variable temperature insert
WAL	weak antilocalization
WL	weak localization

1 Introduction

The experimental realization of graphene in 2004 [1, 2] has caused rapidly increasing research activity on the subject, leading to more than 70,000 publications in the following years [3]. The main reasons for this vast interest are the intrinsic two-dimensional nature and the unique band structure of graphene [4–6]. It is often idealized as a Dirac semi-metal, with the valence and conduction bands touching at the so-called Dirac points of the Brillouin zone. Due to the linear dispersion relation near the Dirac points, charge carriers behave like free massless fermions [7, 8] and travel at the Fermi velocity $v_F \approx c_0/300$, with c_0 being the speed of light in vacuum. The linear dispersion allows to study quantum effects in graphene even at room temperature [9, 10]. In the early years of the rise of graphene, Kane and Mele (2005) [11, 12] predicted that spin-orbit interactions would induce a spin-Hall insulating state. This novel electronic state of matter would be chiral and gapped in the bulk, i.e., near the Dirac points, while supporting spin transport along the sample boundaries. The size of the bulk gap has been estimated by controversial studies to be in the range of 1 µeV to 100 µeV [11, 13–17]. The low energy regime is extremely difficult to resolve and it took until 2012 before Mani *et al.* [18] were able to conduct experiments with µeV accuracy in epitaxial graphene using resistively-detected electron spin resonance, RD-ESR, performed at low temperatures. ESR is spin-sensitive and couples charge carriers of opposite spin by microwave excitation, which can be detected as a change of the resistance of the graphene. With this experimental tool at hand, it is now possible to resolve the intrinsic band gap of graphene and probe additional spin-related quantities, such as the magnitude of the atomic spin-orbit coupling. In this thesis, resistively-detected electron spin resonance is employed to explore intrinsic spin-related phenomena in graphene in order to expand the understanding of its fundamental properties, which is necessary to fuel future research. Additionally, the influence of extrinsic parameters is studied, with the prospect of controlling the intrinsic properties as well as enhancing the experimental technique of resistively-detected electron spin resonance.

This thesis is structured as follows:

- Chapter 2 provides the reader with essential theoretical concepts regarding the electronic properties of graphene as well as the experimental techniques to probe these properties.
- Chapter 3 introduces the sample fabrication, which is based on an approach by T. Lyon *et al.* (2017) [19], and presents the investigated samples in detail.
- Chapter 4 describes the experimental equipment and its operating principles.
- Chapter 5 analyzes the magnetoresistance properties and the intrinsic spin-orbit coupling gap of graphene by employing the technique of resistively-detected electron spin resonance. Additionally, a theory, developed by M. Prada, is presented to interpret the experimental findings.
- Chapter 6 investigates electron spin resonance in graphene at different angles of the externally applied magnetic field. By studying the behavior of the g-factor, it is possible to access additional intrinsic low-energy quantities of graphene. The theoretical model was developed by M. Prada.
- Chapter 7 studies the influence of magnetic nanoparticles on graphene. The electron spin resonance signal is found to be greatly enhanced and possible spin-valve-like effects are discussed.
- Chapter 8 summarizes the findings of the preceding chapters and presents the reader with future improvements to the experiments and ideas to tune the intrinsic properties of graphene.

Various topics presented in this thesis have been part of peer-reviewed publications, such as the sample fabrication [19], the g-factor dependence on the charge carrier density [20], and the determination of the size of the intrinsic spin-orbit coupling gap in graphene [21]. Publications addressing the results of the angle-dependent electron spin resonance as well as weak localization effects are in preparation. Furthermore, the influence of strain on the Dirac point in topological insulator nanowires has been investigated [22]. This topic is not discussed in detail as it would have been beyond the scope of this work.

2 Theory

This chapter addresses the theoretical concepts necessary to interpret the results presented in this work. The following sections describe the fundamental structural and electronic properties of graphene, the behavior of graphene in magnetoresistance experiments, and the mechanisms behind spin-orbit coupling and electron spin resonance.

2.1 Graphene Basics

2.1.1 Lattice and Band Structure

Graphene is a two-dimensional layer of carbon atoms which are arranged in a hexagonal structure, i.e., a structure consisting of two interleaving triangular sublattices A and B, as shown in Fig. 2.1. Each carbon atom has four valence states; three of those form the in-plane σ bands by sp^2 hybridization, which are responsible for the robustness of graphene. The remaining valence state forms an out-of-plane p_z orbital that corresponds to the π band, which gives rise to a cone-shaped dispersion [4, 15] being described in this section.

The lattice structure and the tight binding approach to derive the electronic band structure of graphene were detailed by Castro Neto *et al.* (2009) [23] and are summarized below. The lattice vectors are given by

$$\mathbf{a}_1 = \frac{a}{2}(3,\sqrt{3}), \quad \mathbf{a}_2 = \frac{a}{2}(3,-\sqrt{3}), \tag{2.1}$$

with $a \approx 1.42\,\text{Å}$ being the distance between two neighboring carbon atoms. The nearest neighbor vectors can be written as

$$\boldsymbol{\delta}_1 = \frac{a}{2}(1,\sqrt{3}), \quad \boldsymbol{\delta}_2 = \frac{a}{2}(1,-\sqrt{3}), \quad \boldsymbol{\delta}_3 = -a(1,0), \tag{2.2}$$

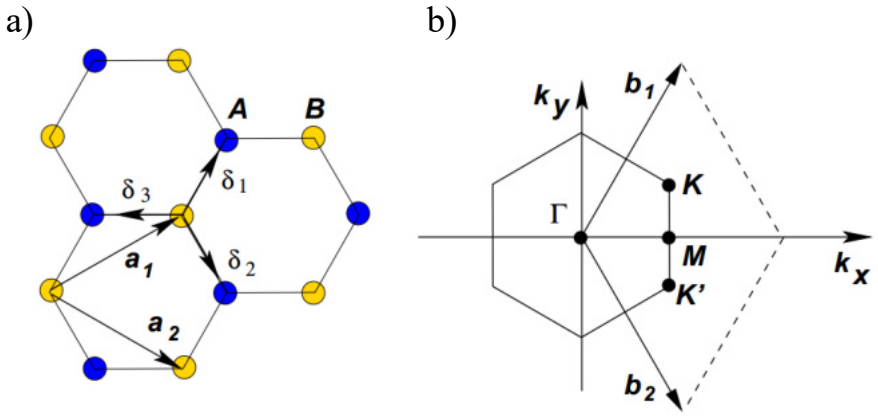

Fig. 2.1. **(a)** Graphene lattice structure in real space. Each colored dot represents a carbon atom, with sublattices *A* and *B* denoted in blue and yellow, respectively. Vectors $\mathbf{a}_{1,2}$ are the lattice vectors and $\boldsymbol{\delta}_{1,2,3}$ the nearest neighbor vectors. **(b)** Graphene lattice in momentum space. Regions of linear dispersion, the so-called 'Dirac cones', are located at the **K** and **K'** points, which stem from the different sublattices.
Reprinted figure with permission from A. H. Castro Neto, F. Guinea, N. M. R. Peres, K. S. Novoselov, and A. K. Geim. The electronic properties of graphene. Reviews of Modern Physics 81, 109162 (2009). Copyright 2009 by the American Physical Society [23].

while the second nearest neighbor vectors are given by

$$\boldsymbol{\delta}'_{1,2} = \pm\mathbf{a}_1, \quad \boldsymbol{\delta}'_{3,4} = \pm\mathbf{a}_2, \quad \boldsymbol{\delta}'_{5,6} = \pm(\mathbf{a}_2 - \mathbf{a}_1). \tag{2.3}$$

In momentum space, the lattice vectors turn into

$$\mathbf{b}_1 = \frac{2\pi}{3a}(1,\sqrt{3}), \quad \mathbf{b}_2 = \frac{2\pi}{3a}(1,-\sqrt{3}). \tag{2.4}$$

The **K** and **K'** points, or 'Dirac points', in reciprocal space display extraordinary properties and play an important role in the physics of graphene. Their coordinates are given by

$$\mathbf{K} = \left(\frac{2\pi}{3a}, \frac{2\pi}{3\sqrt{3}a}\right), \quad \mathbf{K}' = \left(\frac{2\pi}{3a}, -\frac{2\pi}{3\sqrt{3}a}\right). \tag{2.5}$$

A tight-binding Hamiltonian modeling electrons that can hop to nearest and second nearest neighbor atoms in graphene can be written as

$$\begin{aligned}\hat{H}_0 = &- t \sum_{\langle i,j\rangle,\sigma} \left(\hat{a}^\dagger_{\sigma,i}\hat{b}_{\sigma,j} + \text{H.c.}\right) \\ &- t' \sum_{\langle\langle i,j\rangle\rangle,\sigma} \left(\hat{a}^\dagger_{\sigma,i}\hat{a}_{\sigma,j} + \hat{b}^\dagger_{\sigma,i}\hat{b}_{\sigma,j} + \text{H.c.}\right).\end{aligned} \tag{2.6}$$

Here, t and t' are the nearest neighbor and second nearest neighbor hopping parameters, respectively, with energies $t \approx 2.8\,\text{eV}$ and $0.02t \lesssim t' \lesssim 0.2t$ [24]. The operator $\hat{a}_{\sigma,i}$ ($\hat{a}^\dagger_{\sigma,i}$) annihilates (creates) an electron with spin σ ($\sigma = \uparrow, \downarrow$) on site $\mathbf{R}_i$ on sublattice A, and accordingly the operator $\hat{b}_{\sigma,i}$ ($\hat{b}^\dagger_{\sigma,i}$) on sublattice B. This Hamiltonian results in the following energy bands:

$$\begin{aligned}E_\pm(\mathbf{k}) &= \pm t\sqrt{3 + f(\mathbf{k})} - t' f(\mathbf{k}), \\ f(\mathbf{k}) &= 2\cos\left(\sqrt{3}k_y a\right) + 4\cos\left(\frac{\sqrt{3}}{2}k_y a\right)\cos\left(\frac{3}{2}k_x a\right).\end{aligned} \tag{2.7}$$

The + and - signs correspond to the π and $\pi*$ bands (i.e., the cones), respectively, and the resulting band structure is shown in Fig. 2.2. The dispersion around the Dirac point shown in the zoomed-in region can be obtained by expanding the energy bands of Eq. 2.7 in the vicintiy of **K** (and **K'** accordingly) by assuming $\mathbf{k} = \mathbf{K} + \mathbf{q}$ and $|\mathbf{q}| \ll |\mathbf{K}|$ [4]:

$$E_\pm(\mathbf{q}) \approx \pm v_F|\mathbf{q}| + O[(q/K)^2], \tag{2.8}$$

where $\mathbf{q}$ is the momentum relative to **K** and $v_F = 3ta/2 \approx 10^6\,\text{m/s}$ is the Fermi velocity. In graphene, the dispersion relation is linear in momentum in the vicinity of the **K** and **K'** points, as it is the case for free massless particles, and v_F is independent of energy and momentum. Thus, the charge carriers follow the equation for massless Dirac fermions

$$v_F[\hat{\sigma}\cdot(-i\boldsymbol{\nabla})]\Psi(\mathbf{r}) = E\Psi(\mathbf{r}), \tag{2.9}$$

with $\hat{\sigma} = (\sigma_x, \sigma_y, \sigma_z)$ being the Pauli matrix and $\Psi(\mathbf{r})$ the fermion wave function; therefore **K** and **K'** are dubbed 'Dirac points'.

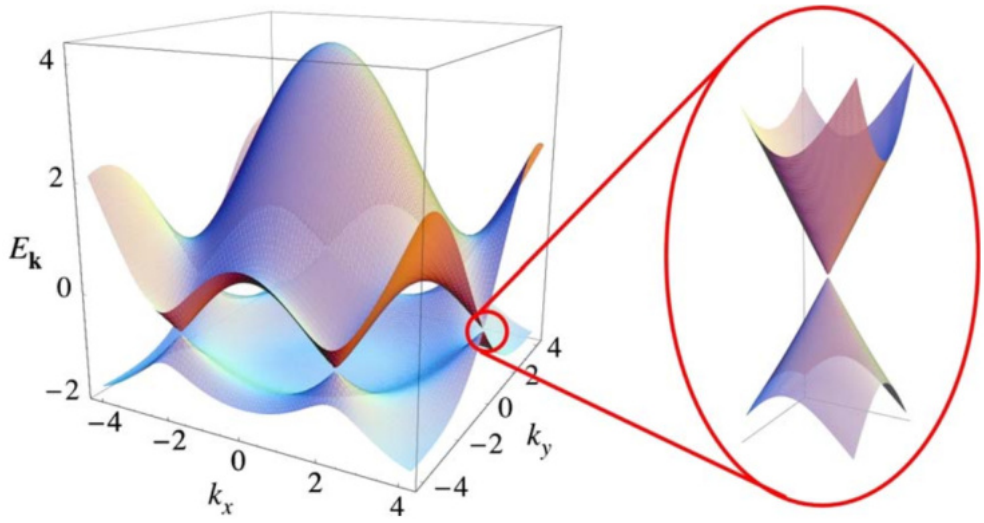

Fig. 2.2. Dispersion relation of a single layer of graphene, with the zoomed-in area showing the region of linear dispersion near one of the Dirac points. States of positive (negative) energy E_k, i.e., the upper (lower) cone, are electron-like (hole-like) states. Reprinted figure with permission from A. H. Castro Neto, F. Guinea, N. M. R. Peres, K. S. Novoselov, and A. K. Geim. The electronic properties of graphene. Reviews of Modern Physics 81, 109162 (2009). Copyright 2009 by the American Physical Society [23].

At the Fermi energy, $|\mathbf{q}| = k_F$ and thus,

$$E_F = \hbar k_F v_F. \tag{2.10}$$

The Fermi wave vector is defined as

$$k_F = \sqrt{\frac{4\pi n}{g_s g_v}} = \sqrt{\pi n}, \tag{2.11}$$

with $g_s = 2$ as the spin degeneracy due to the two spin states ($\uparrow$, $\downarrow$) and $g_v = 2$ as the valley degeneracy due to the two energetically equivalent valleys **K** and **K'** (stemming from the two sublattices A and B of the hexagonal lattice). It is worth noting that k_F solely depends on the charge carrier density n. The Fermi wavelength is then given by

$$\lambda_F = \sqrt{\frac{2\pi}{n}}. \tag{2.12}$$

2.1.2 Density of States

The density of states (DOS) for a hexagonal net was first described by Hobson *et al.* (1953) [25] and was presented for ideal and infinite graphene specifically by Castro Neto *et al.* (2009) [23]. Starting point is the tight-binding Hamiltonian from Eq. 2.6, where the second nearest neighbor hopping parameter $t' = 0$. An analytical expression can be derived for this particular case:

$$\rho(E) = \frac{4}{\pi^2}\frac{|E|}{t^2}\frac{1}{\sqrt{Z_0}}\mathbf{F}\left(\frac{\pi}{2},\sqrt{\frac{Z_1}{Z_0}}\right),$$

with

$$Z_0 = \begin{cases} \left(1+\left|\frac{E}{t}\right|\right)^2 - \frac{\left[(E/t)^2-1\right]^2}{4}, & -t \le E \le t \\ 4\left|\frac{E}{t}\right|, & -3t \le E \le -t \vee t \le E \le 3t, \end{cases} \tag{2.13}$$

$$Z_1 = \begin{cases} 4\left|\frac{E}{t}\right|, & -t \le E \le t \\ \left(1+\left|\frac{E}{t}\right|\right)^2 - \frac{\left[(E/t)^2-1\right]^2}{4}, & -3t \le E \le -t \vee t \le E \le 3t, \end{cases}$$

and $\mathbf{F}(\pi/2,x)$ being the complete elliptic integral of the first kind. The corresponding diagram is shown in Fig. 2.3.

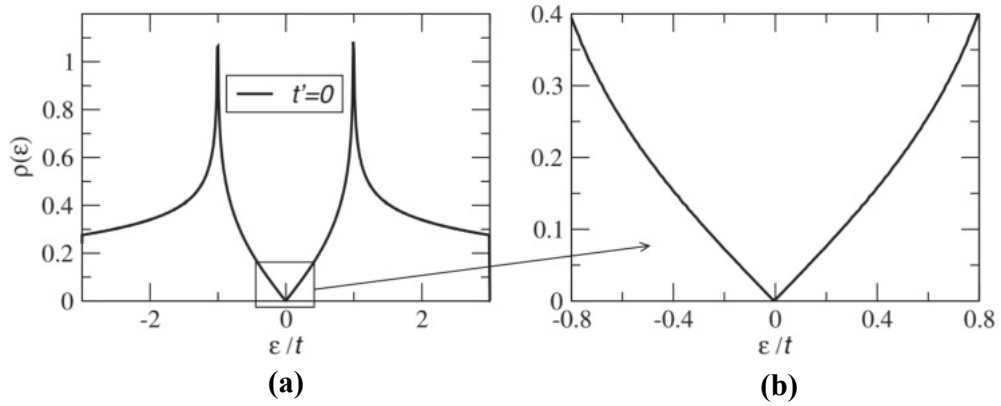

Fig. 2.3. **(a)** Density of states per unit cell as a function of energy in units of the hopping parameter t. **(b)** Zoom-in close to zero energy with an approximately linear DOS $\rho \propto |\epsilon|$.

Reprinted figure with permission from A. H. Castro Neto, F. Guinea, N. M. R. Peres, K. S. Novoselov, and A. K. Geim. The electronic properties of graphene. Reviews of Modern Physics 81, 109162 (2009). Copyright 2009 by the American Physical Society [23].

2.1.3 Spin and Sublattice Spin

As mentioned briefly in Section 2.1.1, in the vicinity of the Dirac points, the charge carriers in graphene exhibit spin and valley degeneracy (which is connected to the sublattice degeneracy) g_s and g_v, respectively, resulting in a four-fold degeneracy. A mathematical description of those degeneracies and their implications for the band structure are laid out in the following paragraphs and were originally developed by Kane & Mele (2005) [11].

The spin degree of freedom can be written as $\{\uparrow,\downarrow\}$, while the sublattice states around A and B atoms of the lattice are given by $\{u_A^K,u_B^K\}$. Due to the similar formalism compared to real spin, the sublattice states are also referred to as 'sublattice spin' or 'pseudospin' states. The wave function then becomes $\Psi_K = [\{\uparrow,\downarrow\} \otimes \{u_A^K,u_B^K\}]$ [23, 26–28], and the Pauli matrices s_i and σ_i act on real spin and pseudospin, respectively. The effective mass Hamiltonian for such a wave function reads [11, 21, 29]

$$\hat{H}(\mathbf{q},\tau) = \hbar v_F \mathbb{I}_2 \otimes (\tau\sigma_x q_x + \sigma_y q_y), \tag{2.14}$$

with $\tau = \pm 1$ labeling the valleys **K** and **K'**, and $\mathbb{I}_2$ being the unitary 2×2 matrix.

The four-fold degeneracy is protected by sublattice symmetry [27] only at **K** and **K'**, while everywhere else $\hat{\sigma}$ and $\mathbf{q}$ are collinear and thus eigenstates of the Hermitian, unitary helicity operator [29–33]

$$\hat{h}_q = \hat{\sigma} \cdot \mathbf{q}/|\mathbf{q}|. \tag{2.15}$$

Note that in graphene, helicity is not defined as the projection of real spin onto the direction of propagation, but as the projection of the pseudospin. Additionally, helicity is equal to chirality and the latter term will be used in the remainder of this work [29, 34].

It follows directly from Eq. 2.14 and 2.15 that near a fixed Dirac point, chirality for electrons is inverted with respect to holes. Additionally, chirality for bands in one valley is inverted with respect to the other valley, as shown in Fig. 2.4. Thus, holes near the **K** point exhibit the same chirality as electrons near **K'** and vice versa.

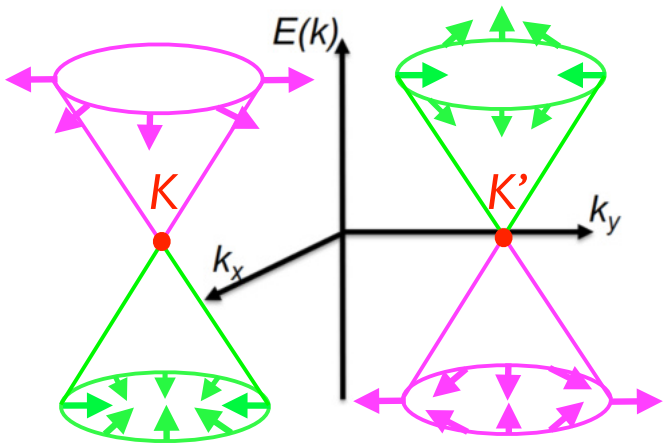

Fig. 2.4. Schematic dispersion of graphene around the **K** and **K'** points. The arrows and colors represent chirality, with magenta being negative and green positive. Figure adopted from private communications with M. Prada.

2.1.4 Intrinsic Spin-Orbit Coupling Gap

At energies very close to the Dirac points, the band structure of graphene changes significantly when intrinsic spin-orbit coupling (ISOC) is introduced. The possible mechanisms behind this ISOC dictate its magnitude and are discussed below. The corresponding Hamiltonian near the Dirac points [11, 12, 27] is given by

$$\hat{H}_{ISOC} = \lambda_I \tau s_z \otimes \sigma_z, \tag{2.16}$$

with λ_I accounting for the magnitude of the ISOC. Parity, time-reversal, sublattice, and planar crystal symmetries are preserved. In combination with the Hamiltonian from Eq. 2.14, the new eigenvalues can be calculated as

$$E(\mathbf{q}) = \pm\sqrt{(v_F\mathbf{q})^2 + \lambda_I^2}. \tag{2.17}$$

Thus, the resulting energy gap due to ISOC is $\Delta_I = |2\lambda_I|$, as shown in Fig. 2.5 and its size is a matter of vivid discussion. Kane *et al.* [12] (2005) first predicted it to be in the range of 100 µeV, before Min *et al.* (2006) [13] and Yao *et al.* (2007) [14] reported values of the order of 1 µeV. However, Gmitra *et al.* (2009) [15], Konschuh *et al.* (2010) [16] and Boettger *et al.* (2007) [17] estimated values of ∼25-50 µeV using first-principles calculations. The difference between these values arises mainly from whether to take into account the nominally unoccupied *d* orbitals in graphene. The findings of larger values for the ISOC gap support

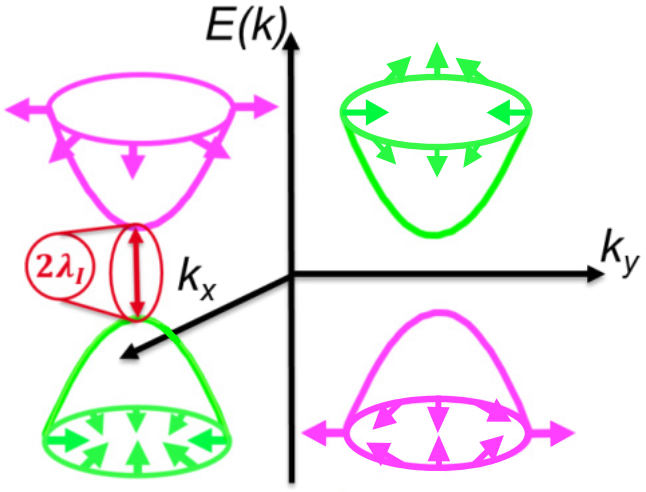

Fig. 2.5. Schematic dispersion of graphene around the **K** and **K'** points including the intrinsic spin-orbit coupling gap of magnitude $\Delta_I = |2\lambda_I|$. The arrows and colors represent chirality, with magenta being negative and green positive. Figure adopted from private communications with M. Prada.

the view that the d orbitals can be used for hopping events by electrons (recall Section 2.1.1) which results in a finite mean occupation and thus in a contribution to the ISOC. Furthermore, the d orbitals give the dominant contribution to Δ_I due to the higher overlap with the p_z orbital (remember: p_z corresponds to the π bands and thus the carriers in the Dirac cones) compared to the sp^2 orbitals. The splitting depends linearly on the splitting of the d states and only quadratically on the splitting induced by the sp^2 orbitals [15]. Nevertheless, this debate is still ongoing, since no precise value has been found, mostly owed to the small energy range making experimental accessibility difficult.

2.1.5 Rashba Spin-Orbit Coupling

In addition to the ISOC in graphene, extrinsic effects can influence the size of the spin-orbit coupling (SOC) gap, i.e., the application of an electric field perpendicular to the graphene plane or the interaction of graphene with a substrate, dopants, and impurities break the planar mirror symmetry of the crystal structure. These effects can give rise to an additional term in the Hamiltonian [11, 35], most prominently the Rashba spin-orbit coupling:

$$\hat{H}_R = \lambda_R(\hat{\sigma}_x \tau s_y - \hat{\sigma}_y s_x), \tag{2.18}$$

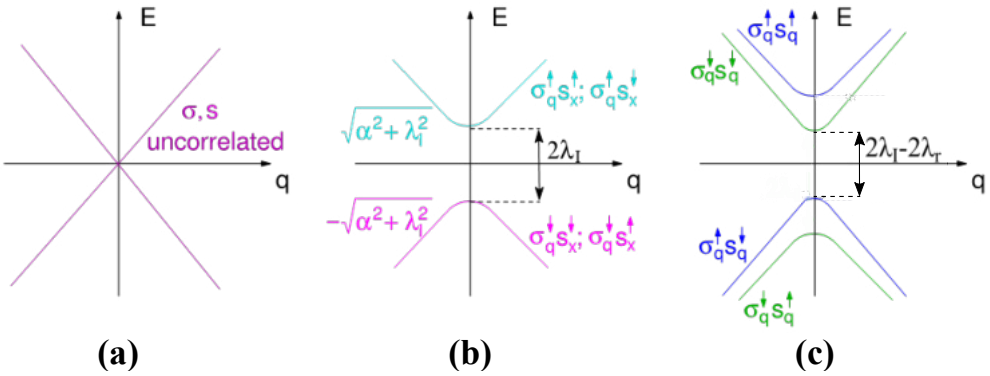

Fig. 2.6. Schematic representation of the band structure (a) with no SOC (b) with an ISOC gap determined by λ_I, and (c) with both intrinsic and extrinsic SOC, such that $\lambda_I > \lambda_R$. Figure adopted from Sichau *et al.* (2019) [21], Supplemental Material.

with λ_R determining the magnitude of the Rashba SOC. This new term in the Hamiltonian results in modified eigen-energies [15] given by

$$E(\mathbf{q}) = \mu\lambda_r + \nu\sqrt{(\hbar v_F \mathbf{q})^2 + (\lambda_r - \mu\lambda_I)^2}, \tag{2.19}$$

where $\mu = \pm 1$ and $\nu = \pm 1$. As a consequence, the band structure exhibits four energy bands instead of previously two, and the size of the band gap is then $\Delta E = 2(\lambda_I - \lambda_r)$. The gap, and therefore the chirality picture, described in the previous section stays intact as long as $\lambda_I > \lambda_r$. For $\lambda_I \leq \lambda_r$, the gap opens up again, but this time as a trivial insulator. Thus, in order to measure the ISOC gap, it is necessary to keep the Rashba SOC contribution minimal. A summary of the influence of the discussed types of SOC on the band structure is displayed in Fig. 2.6.

2.2 Lateral Confinement Effects

2.2.1 Sample Boundaries

The previous sections described an ideal, infinite sheet of graphene. It is essential, however, to consider real-life finite graphene samples and the influence of sample boundaries in order to understand and interpret experimental results. There are two edge types, the armchair and the zigzag edges, as shown in Fig. 2.7. Other edge types are either combinations of the two, or form due to defects, e.g., vacancies or interstitials [36]. The calculations presented in this

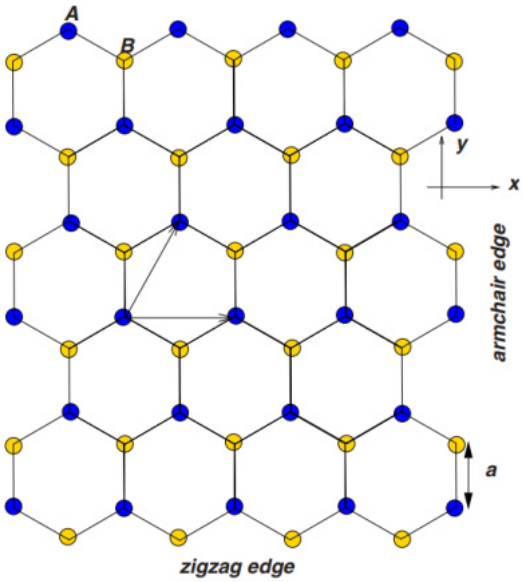

Fig. 2.7. Zigzag and armchair edges in graphene. The zigzag edge type exhibits only *A* atoms on one edge and only *B* atoms on the opposing edge, while the armchair type shows *ABAB* sequences on both sides.
Reprinted figure with permission from A. H. Castro Neto, F. Guinea, N. M. R. Peres, K. S. Novoselov, and A. K. Geim. The electronic properties of graphene. Reviews of Modern Physics 81, 109162 (2009). Copyright 2009 by the American Physical Society [23].

work focus on the zigzag edge type. While all the aforementioned edge types are likely to occur in real samples, they would yield qualitatively similar results, since one can assume the bulk-edge correspondence and the continuum limit [37] for the samples presented in this work.

The intrinsic energy gap at the Dirac points (see Section 2.1.4) is still present in finite samples and originates from the bulk of graphene. Topologically protected eigenstates emerge within the gap, connecting the bulk bands diagonally, i.e., electrons from **K** with holes from **K'** and vice versa, because they share the same chirality. A schematic drawing of the resulting band structure is shown in Fig. 2.8. Those midgap states are localized at the sample boundaries and are called 'edge states'. They exhibit collinear spin **s** and pseudospin $\hat{\sigma}$, which is also collinear with **q** [21].

A quantitative analysis of the band structure is performed by numerical tight-binding calculations for a honeycomb lattice that is infinite along one direction and terminated by a zigzag edge along the perpendicular direction. A detailed description of this calculation was presented by Sichau *et al.* (2017) [21]. The first several hundred of the lowest energy bands were calculated and an excerpt

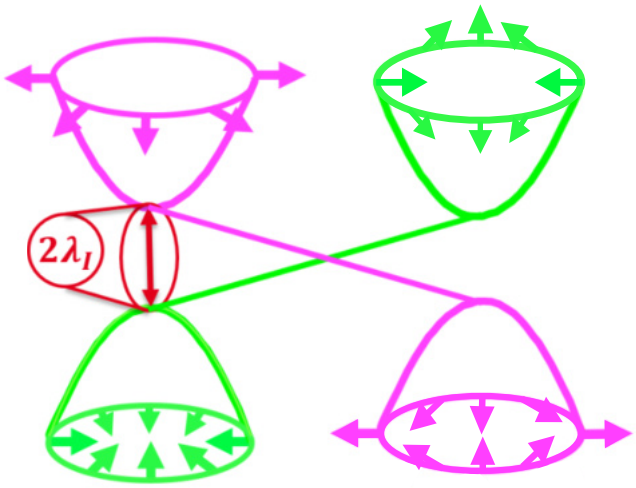

Fig. 2.8. Schematic dispersion of graphene around the **K** and **K'** points including the intrinsic spin-orbit coupling gap of magnitude $\Delta_I = |2\lambda_I|$ and the midgap states that are located on the sample edges. The arrows and colors represent chirality, with magenta being negative and green positive. Figure adopted from private communications with M. Prada.

is shown in Fig. 2.9, with the bands colored according to their chirality (see Eq. 2.15). The similarity between this figure and the schematic in Fig. 2.8 is obvious, even though the bands within the gap are much flatter. This flatness represents a high local density of states (LDOS), since many eigenstates exist in a narrow window of energy.

Fig. 2.10a shows a 10,000-fold zoom into the low energy range at the band gap to resolve the linear dispersion of the edge states. Here, the brightness of the bands represents the LDOS, which is much higher at the edges than in the bulk.

Additionally, for the sake of simplicity, the two-fold sublattice degeneracy of the midgap states is artificially lifted by focusing on the eigenstates of one edge (one sublattice) only, in this case edge E1 (see Fig. 2.10b). In this picture, the focus lies on the electron spin, with spin-up states colored in green and spin-down states in magenta. From the slope of the two crossing edge bands one can extract the respective charge carrier velocity $v = {\mathrm{d}E(k)}/{\mathrm{d}k}$. On E1, it is negative for carriers with spin down and positive for spin up. It is easy to transfer this situation to edge E2, which is simply the mirror-reflected E1, i.e., spin up becomes spin down and vice versa, while the direction of transport remains unchanged. This entails major consequences: The direction of transport

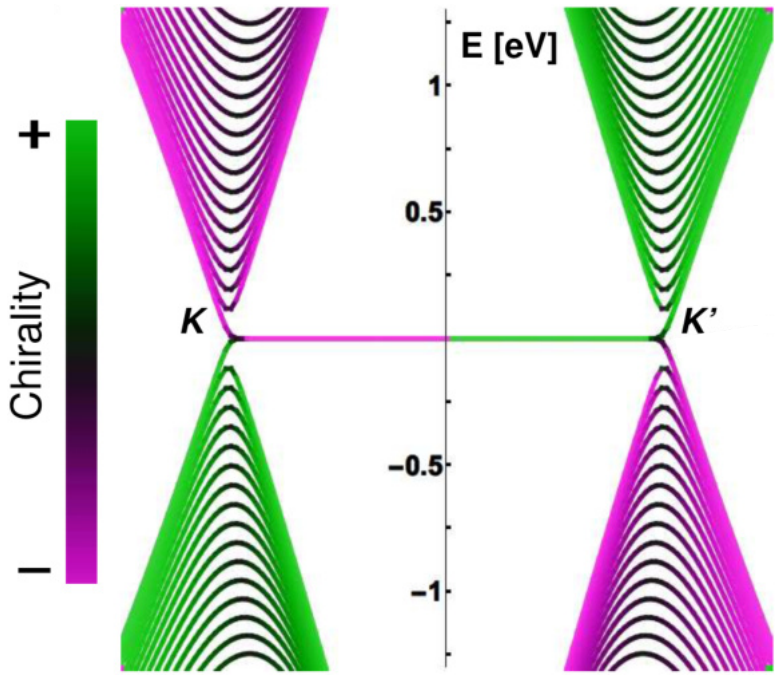

Fig. 2.9. Energy bands of a finite graphene sample. The bulk is gapped at the **K** and **K'** points, with helical edge states connecting the bulk bands diagonally through the gap. However, they appear horizontal due to the size of the energy gap compared to the scale of the whole band structure. The flatness of the edge states is associated with a high LDOS. Figure adopted from Sichau *et al.* (2019) [21].

is spin-dependent at each edge, as depicted in Fig. 2.10b, and while the Fermi energy lies within the gap, current can only flow at the edges. As mentioned previously, these eigenstates are topologically protected, and this phase of matter is termed spin Hall insulator (SHI).

2.2.2 Density of States with Edges

For graphene with boundaries, the density of states is calculated numerically [38–41]. Defects in the lattice, deformations or impurities can lead to similar effects [42–45]. The result is usually a finite DOS at zero energy and those states are localized at the edges, as shown in Fig. 2.11.

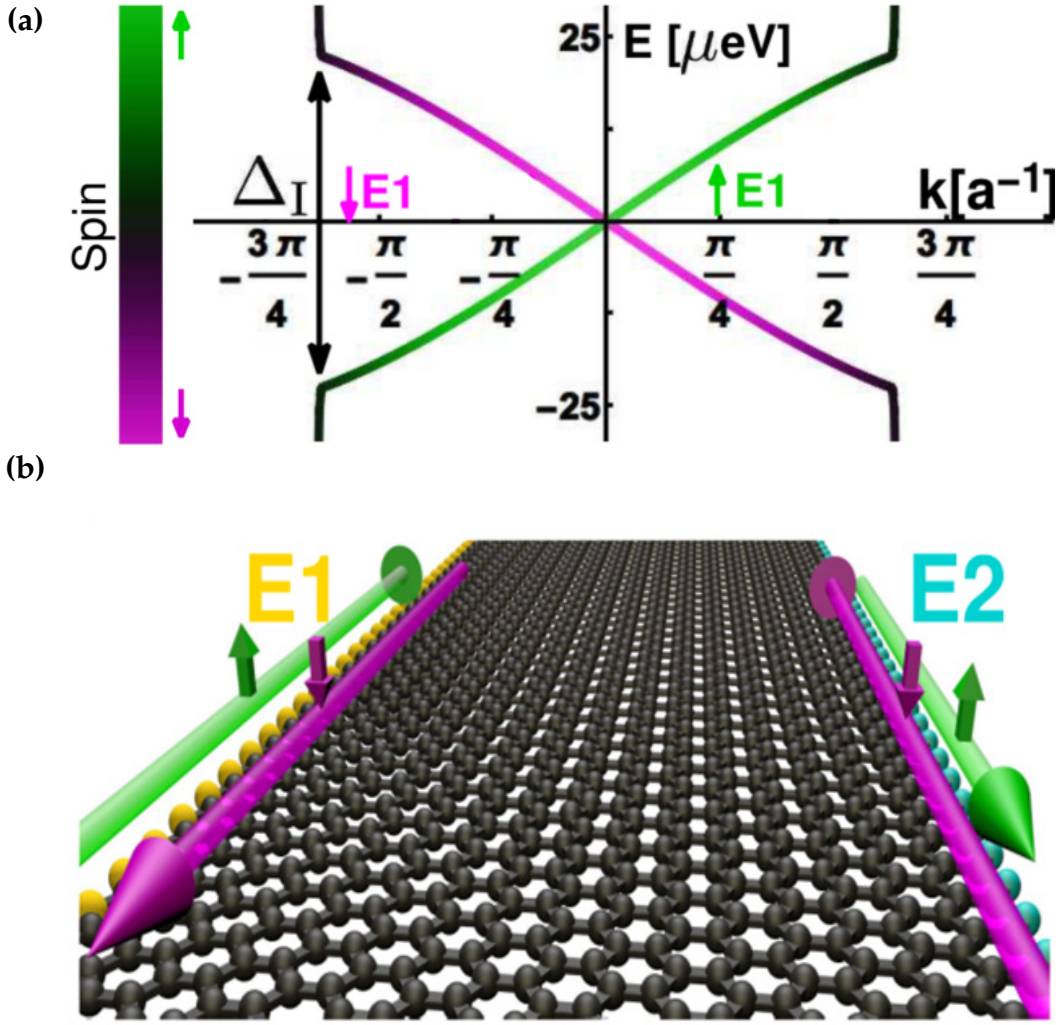

Fig. 2.10.
(a) Zoom-in on the edge states within the bulk band gap for edge E1. Green and magenta denote spin up and spin down, respectively, while black indicates eigenstates with bulk character. The bulk band gap Δ_I is assumed to be caused by ISOC. Edge states with spin up (down) travel with positive (negative) velocity, which can be derived from the slope of the bands. Figure adopted from Sichau *et al.* (2019) [21]. **(b)** Schematic illustration of the edge modes. Charge carrier transport is spin-dependent, thus depicting the SHI phase of graphene.

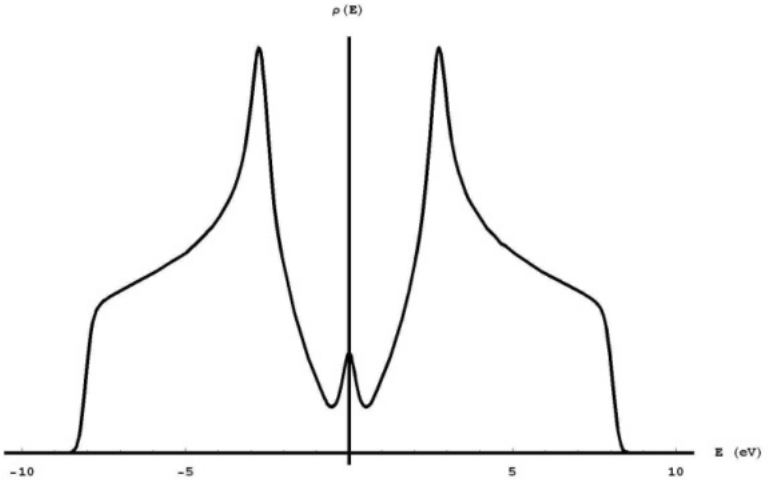

Fig. 2.11. Density of states for a graphene ribbon with zigzag edges. As opposed to ideal, infinite graphene, there is a finite number of states around zero energy that are localized at the edges.
Reprinted figure with permission from A. Carpio, L. L. Bonilla, F. de Juan, and M. A. H. Vozmediano. Dislocations in graphene. New Journal of Physics, 10(5), 053021 (2008) [43].

2.2.3 Density of States with Doping

The consequences of introducing realistic carrier doping to the DOS calculations are described by Sichau *et al.* (2017) [21]. Electron-electron interactions are considered by employing a mean-field Hubbard model which adds an on-site Coulomb repulsion term to the tight binding Hamiltonian of Eq. 2.6:

$$\hat{H}_U^{MF} = U \sum_{i,\sigma} \langle \hat{n}_{i,\sigma} \rangle \hat{n}_{i,\sigma} - UN \sum_i \langle \hat{n}_{i\downarrow} \rangle \langle \hat{n}_{i\uparrow} \rangle. \tag{2.20}$$

The result is a shift in the DOS, so that doping with electrons (holes) would move the zero energy peak from Fig. 2.11 to $E > 0$ ($E < 0$). In Fig. 2.12, the shift is calculated for a typical charge carrier density for the samples presented in this work of $\sim 2 \cdot 10^{11}\,\mathrm{cm}^{-2}$ electrons. The Fermi energy E_F is 0.8 meV away from the peak at half-filling E_{HF}. At absolute zero, all edge states would be filled. Due to finite temperatures, however, charge carriers can be found at higher energies and thus open up eigenstates within the band gap. This is important for the interpretation of experimental data in the following chapters.

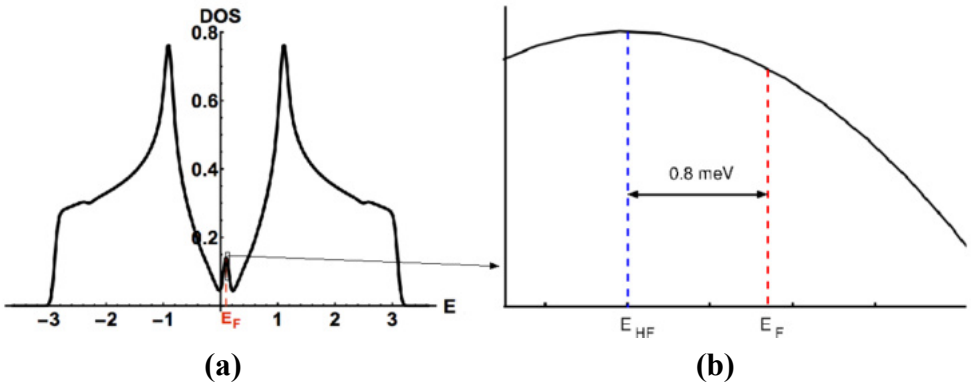

Fig. 2.12. **(a)** Density of states for a doped sample with $n \approx 2 \cdot 10^{11}\,\mathrm{cm}^{-2}$. The zero energy peak is shifted to the right. **(b)** Zoom-in of the center DOS peak. It occurs at half-filling E_{HF}, with the Fermi energy shifted by 0.8 meV to the right. Figure adopted from Sichau *et al.* (2019) [21], Supplemental Material.

2.2.4 Control of the Charge Carrier Density

The control of the charge carrier density via electrostatic gating is linked to the capacitance between sample and (metallic) gate. This section summarizes the work of T. Lyon (2017) [46] on the topic.

When graphene is placed on an insulator, typically an oxide like SiO_2, the charge carrier density n can be controlled by a back-gate. The geometric gate capacitance is calculated as

$$n = \frac{C_g}{e}(V_g - V_{CNP}) + n^*, \tag{2.21}$$

where V_g is the applied gate voltage and V_{CNP} the gate voltage of the Dirac point or charge neutrality point (CNP). n^* is the carrier density due to charged impurities on the graphene and the SiO_2-graphene interface. The calculation of n^* was developed by Adam *et al.* (2007) [47] and the details can be found in their work. The value for the samples presented in this work is of the order of $n^* \approx 1.5 \cdot 10^{11}\,\mathrm{cm}^{-2}$ [19]. It is necessary to determine the gate capacitance as precisely as possible to calculate the charge carrier density n. The geometric capacitance is influenced by the thickness t_{ox} and the relative permittivity κ of the oxide:

$$C_{ox} = \frac{\kappa \epsilon_0}{t_{ox}}, \tag{2.22}$$

with ϵ_0 being the vacuum permittivity. In this work, all substrates have

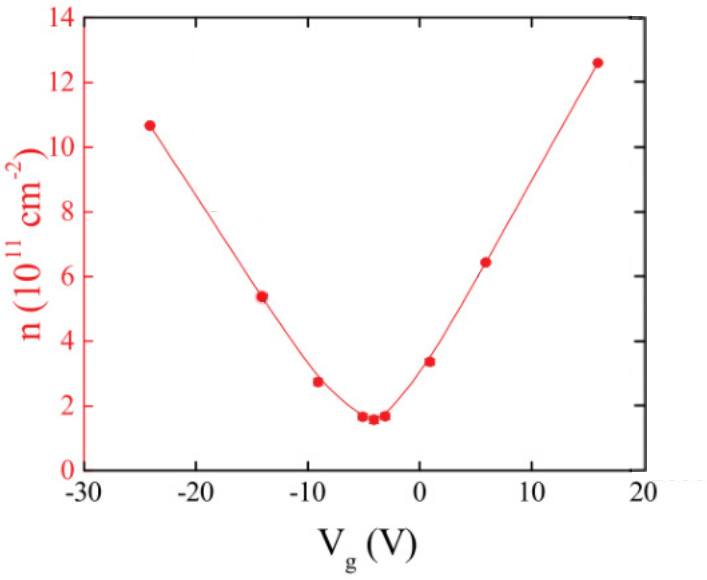

Fig. 2.13. Charge carrier density n versus gate voltage V_g for a real graphene sample with $V_{CNP} = -4\,\mathrm{V}$. The linear region away from the Dirac point is dominated by the geometrical capacitance while the curved non-zero minimum is caused by charged impurities.
Reprinted and modified figure with permission from T. J. Lyon *et al.* (2017) [20].

a $t_{ox} = 300\,\mathrm{nm}$ thick layer of SiO_2 with a relative permittivity of $\kappa = 3.9$, resulting in a capacitance of $C_{ox} = 115\,\mathrm{aF/\mu m^2}$. Other capacitances like the quantum capacitance [48] are modeled as being in series with the geometric capacitance. However, they are negligible due to the oxide layer in the samples being so thick. Since a thick oxide leads to a small C_{ox}, it becomes the dominant capacitance when modeled in series. In contrast to ideal graphene, the carrier density vs. voltage dependence is slightly rounded and non-zero in the vicinity of $V_g = V_{CNP}$ due to charged impurities [47] and the finite temperature that thermally activates carriers. A typical example of carrier density in dependence of gate voltage is shown in Fig. 2.13 [20].

2.3 Magnetoresistance

Magnetoresistance measurements can be performed to study the electrical resistance of low-dimensional charge systems in an external magnetic field. This is usually done at low temperatures in order to minimize the influence of phonons and access the necessary energy scale to observe quantum effects, i.e., $k_B T \approx E_F$. The standard measurement setup for a two-dimensional (2D) system is a Hall

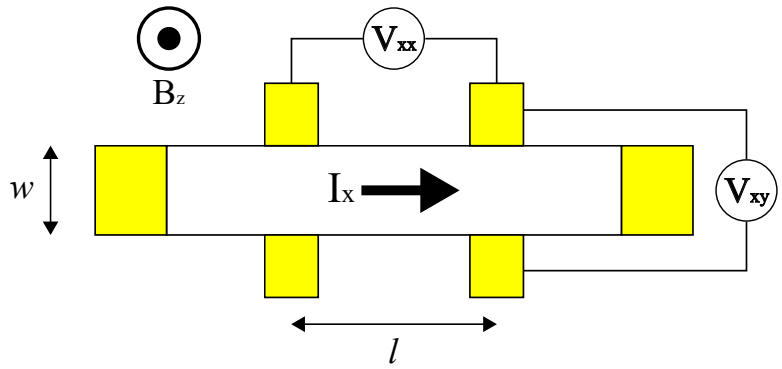

Fig. 2.14. Typical Hall bar geometry and measurement setup. The electrical current I_x flows in x-direction, longitudinal and transverse voltages V_{xx} and V_{xy}, respectively, are measured by the indicated contacts, and the magnetic field B_z is perpendicular to the plane. Width w and length l of the setup are shown as well.

bar geometry as depicted in Fig. 2.14, with source and drain contacts for the electrical current, along with additional contact pairs to measure longitudinal and transverse voltages. The magnetic field is oriented perpendicularly to the sample plane.

2.3.1 Hall and Quantum Hall Effects in Graphene

When a magnetic field $\mathbf{B}$ is applied perpendicularly to the current flow through a conductor, the Lorentz force $\mathbf{F_L} = q\mathbf{v} \times \mathbf{B}$ accelerates the charge carriers to one side of the conductor, where the accumulated charges generate an electric field that acts perpendicularly to the current direction. The resulting Coulomb force $\mathbf{F_C} = q\mathbf{E}$ compensates the Lorentz force and a constant Hall voltage, V_{xy}, can be measured between opposite sample edges. For a 2D system like graphene, the Hall resistivity is given by

$$\rho_{xy} = \frac{V_{xy}}{I_x}, \tag{2.23}$$

while the longitudinal resistivity along the current direction can be written as

$$\rho_{xx} = \frac{w}{l}\frac{V_{xx}}{I_x}, \tag{2.24}$$

using the notation from Fig. 2.14. These quantities can also be expressed in terms of the components of the conductivity and resistivity tensors [49], i.e.,

$$\rho_{xx} = \frac{\sigma_{xx}}{\sigma_{xx}^2 + \sigma_{xy}^2}, \tag{2.25}$$

$$\rho_{xy} = \frac{\sigma_{xy}}{\sigma_{xx}^2 + \sigma_{xy}^2}. \tag{2.26}$$

In contrast to the three-dimensional case, the units of resistivity ρ (conductivity σ) and resistance R (conductance G) are identical and are given in Ω (S). Magnetoresistance measurements are the tool of choice to determine a multitude of transport properties, such as the charge carrier density n, which can be extracted from the Hall resistivity [49]:

$$n = \frac{B}{e\rho_{xy}} = \left(e\frac{\mathrm{d}\rho_{xy}}{\mathrm{d}B}\right)^{-1}. \tag{2.27}$$

The charge carrier mobility is given by

$$\mu = \frac{1}{en\rho_{xx}(B=0)}, \tag{2.28}$$

and both n and μ are necessary to obtain the mean free path l_m of the charge carriers, which describes the length scale of ballistic transport [50, 51]:

$$l_m = \frac{h\mu}{2e}\sqrt{\frac{n}{\pi}}. \tag{2.29}$$

The corresponding transport scattering time τ_l is then given by

$$\tau_l = \frac{l_m}{v_F}. \tag{2.30}$$

The above quantities can be influenced by charged impurities [47], vacancies in the lattice and grain boundaries[52–55], which are typical for graphene that was manufactured by chemical vapor deposition. Another aspect distinct for graphene are intrinsic ripples [56, 57] that occur even when placed on a flat surface, inducing an electrochemical potential variation.

At sufficiently low temperatures and high magnetic fields, the charge carriers are forced on discrete quantized orbits called Landau levels (LL). To define their eigen-energies, it is necessary to introduce the magnetic length l_B, which is the smallest cyclotron radius possible due to the uncertainty principle. For 2D systems, it is in general given by [34]

$$l_B = \sqrt{\frac{\hbar}{eB}}, \tag{2.31}$$

and for massless charge carriers as in graphene, the corresponding cyclotron frequency

$$\omega_c = \sqrt{2}\frac{v_F}{l_B} = v_F\sqrt{\frac{2eB}{\hbar}}, \tag{2.32}$$

with the factor $\sqrt{2}$ stemming from the quantization of the system [23]. The introduction of minimal coupling to Eq. 2.9, i.e., $-i\boldsymbol{\nabla} \rightarrow -i\boldsymbol{\nabla} + e\mathbf{A}/c$, results in the LL eigen-energies [5]

$$E_N = \pm\hbar\omega_c\sqrt{N} = \pm v_F\sqrt{2e\hbar BN}, \tag{2.33}$$

with the LL index $N = 0,1,2,....$ Each Landau level in graphene is four-fold degenerate due to spin and sublattice degeneracy, and in real samples, these sharp energies are broadened due to disorder.

The quantum Hall effect (QHE) can be observed if the separation of LLs is greater than the thermal broadening of the Fermi edge, $\Delta E_N \gg k_B T$. Due to the square root dependence of E_N in graphene, this is possible even at room temperature [9].

When the magnetic field is constant and the Fermi energy is shifted through the spectrum of LLs, e.g., by changing the gate voltage V_g, there are no conduction channels available as long as E_F is in between two levels, resulting in $\sigma_{xx} = 0$. Thus, according to Eq. 2.26, $\rho_{xx} = 0$ and $\rho_{xy} = 1/\sigma_{xy} = \text{const}$. When E_F is crossing a LL, conduction is possible and ρ_{xy} changes. For graphene, plateaus of constant resistivity (conductivity) appear at values of [34]

$$\rho_{xy} = \pm\frac{h}{\nu e^2} \qquad \left(\sigma_{xy} = \pm\nu\frac{e^2}{h}\right), \tag{2.34}$$

with + and - denoting electrons and holes, respectively, and the filling factor

$$\nu = 4(N + \frac{1}{2}), \tag{2.35}$$

where the factor 4 arises from the four-fold degeneracy, and N is again the LL index. Hence, the distance between two neighboring conductivity plateaus is $4e^2/h$. In contrast to other 2D systems such as two-dimensional electron gases, no plateau appears at $N = 0$ due to the presence of a LL (see

Eq. 2.33). Instead, possible filling factors are derived from half-integer values (see Eq. 2.35), thus terming the phenomenon 'half-integer QHE' [7, 8, 58]. An exemplary measurement is shown in Fig. 2.15.

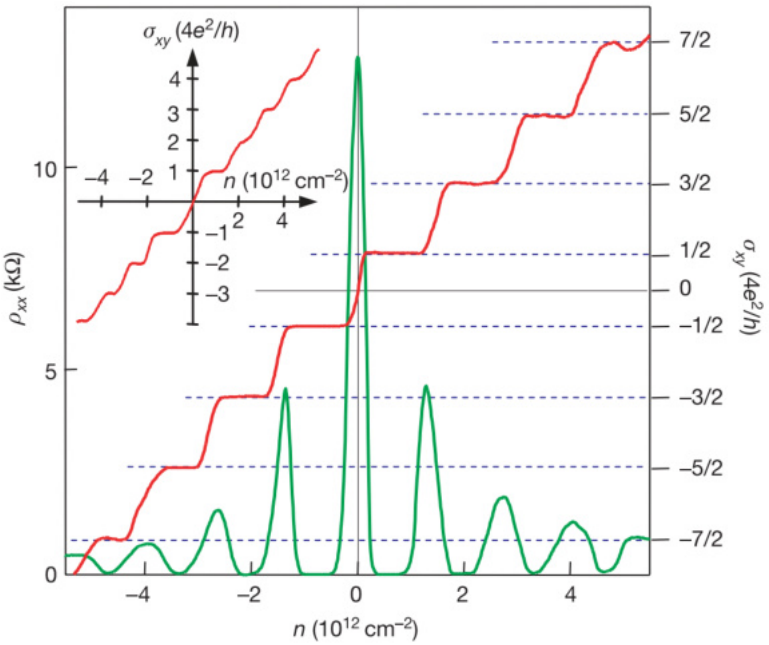

Fig. 2.15. Half-integer quantum Hall effect in graphene at $B = 14\,\mathrm{T}$ and $T = 4\,\mathrm{K}$. The Hall conductivity σ_{xy} (red) as a function of charge carrier density n exhibits plateaus at half-integer values. Conductivity instead of resistivity is plotted to avoid the discontinuity at $n \approx 0$. The zero-resistivity minima of ρ_{xx} (green) coincide with the plateaus of σ_{xy}. The inset shows the QHE for bilayer graphene.
Reprinted by permission from: Springer Nature. Nature. Two-dimensional gas of massless Dirac fermions in graphene. K. S. Novoselov, A. K. Geim, S. V. Morozov, D. Jiang, M. I. Katsnelson, I. V. Grigorieva, S. V. Dubonos, and A. A. Firsov. Copyright 2005 [7].

2.3.2 Two Carrier Transport

As mentioned in Section 2.2.4, in graphene under realistic conditions, the charge carrier density n is finite at the Dirac point. The main reasons are charged impurities, random potential fluctuations responsible for electron and hole puddles [59], and thermal broadening, which causes fluctuations in electron and hole densities. Nevertheless, the point at which the charge carrier density is at its minimum is referred to as the CNP, and electrons and holes exhibit equal, yet finite concentrations in this regime, both contributing to transport [60, 61].

At magnetic fields where no Landau quantization is present (i.e., $\omega_c\tau << 1$, where ω_c is the cyclotron frequency), one can evaluate transport by employing

the Drude model, as presented by Hilke *et al.* (2014) [61]. Simple assumptions are $\rho_{xx}^{\eta} = \sigma_{\eta}^{-1}$, and $\rho_{xy}^{\eta} = \text{sign}(q_{\eta})B/e\eta$, with $\eta = n$ or p for electron or hole densities, respectively, and the total resistivity $\rho_{tot} = (\hat{\sigma}_n + \hat{\sigma}_p)^{-1}$. The field dependence of magnetoresistivity can then be written as

$$\rho_{tot} = \frac{(np)^2(\sigma_n + \sigma_p) + B^2\sigma_n\sigma_p(n^2\sigma_p + p^2\sigma_n)}{(np)^2(\sigma_n + \sigma_p)^2 + B^2(\sigma_n\sigma_p)^2(n-p)^2}, \tag{2.36}$$

and the relative field dependence is given by

$$\frac{\Delta\rho_{xx}}{\rho_{xx}} = \frac{\rho_{xx}(B) - \rho_{xx}(0)}{\rho_{xx}(0)} = \frac{(B/B_0)^2}{1 + (B/B_1)^2}, \tag{2.37}$$

with

$$\begin{aligned} B_0 &= \frac{enp(\sigma_n + \sigma_p)}{\sqrt{\sigma_n\sigma_p}(p\sigma_n + n\sigma_p)} \approx \frac{en_0\rho_{max}^2}{\rho_{xx}}, \\ B_1 &= \frac{enp(\sigma_n + \sigma_p)}{|n-p|\sigma_n\sigma_p} \approx \frac{n_0 B_0}{|n-p|}, \end{aligned} \tag{2.38}$$

where $\rho_{max} \equiv \rho_{xx}(0)$ at the CNP, and n_0 is the residual charge carrier density at the CNP. As long as $B \leq B_1$, Eq. 2.36 gives a parabolic contribution to the resistivity.

2.3.3 Disorder Corrections

The quantum interference effect of weak localization (WL) stems from coherent backscattering due to disorder under the assumption that the phase coherence time τ_ϕ is much larger than the elastic scattering time τ_p. In diffusive transport, charge carriers then have an increased probability to scatter in a closed loop back to their point of origin, resulting in a reduced conductivity [62–65].

As shown in Fig. 2.16, charge carriers can be scattered by impurities and they have a certain quantum mechanical probability amplitude of moving on self-intersecting paths. The conductance diminishes at $B = 0$ if the enhanced backscattering of the electrons leads to a mean non-zero phase difference and an overall constructive interference.

In contrast to the three-dimensional case, the probability of self-intersecting paths is much larger in 2D systems and WL potentially adds a large correction to the classical Drude conductivity.

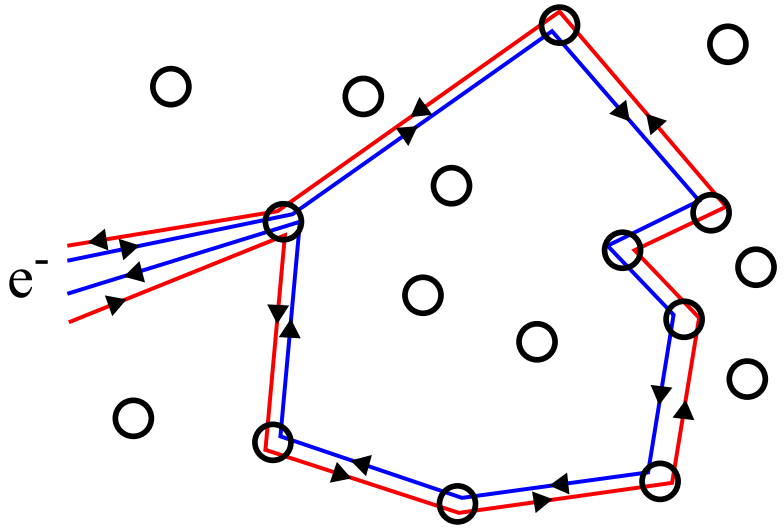

Fig. 2.16. Schematic depiction of an electron being scattered by impurities. The blue and red paths represent clockwise and counter-clockwise trajectories, respectively, resulting in quantum corrections to the classical Drude conductivity.

By applying a magnetic field, however, the time-reversal symmetry between the two paths is destroyed and the interference vanishes, which suggests employing a magnetic field to detect the effect.

Furthermore, if strong spin-orbit coupling is introduced to the system, the spin will be associated with the momentum of the charge carriers and the wave functions of clockwise and counter-clockwise paths are of opposite signs, i.e., an effective π phase shift is induced. Hence, the interference becomes destructive, backscattering is now suppressed and conductivity enhanced. This effect is termed weak antilocalization (WAL).

Graphene is known to exhibit relatively weak spin-orbit coupling, but it is peculiar in the regard that it has chiral charge carriers (see Section 2.1.3). Under the condition that there is no scattering between the **K** and **K'** valleys, chirality results (similar to strong SOC) in a Berry phase of π, meaning that one trajectory experiences a π phase shift after completing a closed loop with respect to the counter-propagating trajectory, i.e., the WL effect is turned into WAL.

In a simple model, one can assume that if intervalley scattering is suppressed and hence, intravalley scattering is dominant, WL can be observed. On the other hand, intervalley scattering can be caused by ripples and sharp defects, and, if dominant, favors WAL [66]. In terms of characteristic scattering times, the condition is $\tau_* \ll \tau_i$ for WL, and $\tau_i \ll \tau_*$ for WAL, with τ_* (τ_i) denoting intravalley (intervalley) scattering.

A mathematical model to evaluate localization effects in magnetoresistance measurements in graphene was developed by McCann *et al.* (2006) [67]:

$$\begin{aligned}
\rho(B) - \rho(0) &= -\frac{e^2\rho^2}{\pi h}\left[F\left(\frac{B}{B_\phi}\right) - F\left(\frac{B}{B_\phi + 2B_i}\right) - 2F\left(\frac{B}{B_\phi + B_i + B_*}\right)\right], \\
F(z) &= \ln z + \Psi\left(\frac{1}{2} + \frac{1}{z}\right), \\
B_{\phi,i,*} &= \frac{\hbar}{4De}\tau^{-1}_{\phi,i,*},
\end{aligned} \tag{2.39}$$

where Ψ is the digamma function, D is the diffusion constant, and τ_ϕ is the phase coherence time.

With this model, it is possible to verify the assumptions about the scattering rates from above. If $\Delta\rho \equiv \rho(B) - \rho(0)$ is negative, WL is observed and hence, the first term in square brackets in Eq. 2.39 contributes to WL while the second and third terms contribute to WAL accordingly. In a perfect system where both intra- and intervalley scattering are absent, $\tau_{i,*} \to \infty$ and $B_{i,*} \to 0$, meaning $\Delta\rho$ is dominated by $-2F(B/B_\phi)$, bringing the system into the WAL regime. However, in the case of a realistic sample, scattering mechanisms are present and their magnitude is important. For dominant intervalley scattering $\tau_i \ll \tau_* < \tau_\phi$ and therefore $B_* + B_i \approx B_i > B_\phi$, which results in $\Delta\rho > 0$, and the system shows WAL. When intravalley scattering is dominant, $\tau_* \ll \tau_i$ and $B_* \gg B_i$, the third term vanishes, $\Delta\rho < 0$, and the system exhibits WL.

2.4 Electron Spin Resonance

The experimental technique of electron spin resonance (ESR) uses electromagnetic radiation to study the interaction of electron spins with a magnetic field. It is sensitive to the energy splitting which electrons experience due to the possible spin orientations with respect to the magnetic field vector. The radiation frequency has to match the energy or time scale of the processes involved in the study, and the magnitude of magnetic fields applied in this work corresponds to frequencies in the GHz regime.

This chapter discusses the fundamental concepts of ESR and focuses specifically on resistively-detected electron spin resonance (RD-ESR), a technique that

relies on the influence of electron spin excitation on the overall resistivity of a sample.

2.4.1 Fundamentals of ESR

In this section, the basic principles of ESR are explained for the case of a single electron. The electron spin $\boldsymbol{s}$ is associated with a magnetic moment $\boldsymbol{\mu} = -g\mu_B\boldsymbol{s}$, where g is the g-factor ($g \approx 2.0023$ for the free electron), and μ_B is the Bohr magneton. When an external magnetic field, e.g., $\boldsymbol{B} = B_z\hat{\boldsymbol{e}}_z$, is applied, the magnetic moment of the electron will align collinearly with the field, so that the Zeeman energy can be written as

$$E_Z = g\mu_B\boldsymbol{s}\cdot\boldsymbol{B} = g\mu_B m_S B_z, \tag{2.40}$$

with the eigenvalues $m_s = \pm 1/2$, referred to as "spin-up" and "spin-down" states of the z-component of the spin operator $\boldsymbol{s}$. Note that there are $2s+1$ Zeeman levels in more complex systems, and $-s \leq m_s \leq s$. The resulting energy difference ΔE_Z between the two states is termed Zeeman splitting. When a photon γ with frequency ν fulfills the resonance condition (see Fig. 2.17)

$$E_\gamma = h\nu = g\mu_B|\Delta m_s|B_z = \Delta E_Z, \tag{2.41}$$

a spin flip can be induced via interaction with the electron, i.e., for a transition from spin down to spin up, the photon is absorbed by the electron, while it is emitted in the reverse process. In addition to the energy of the photon, the orientation of its magnetic field vector $\boldsymbol{B}_\gamma$ plays a significant role. In this work, loop antennas are used to transmit linearly polarized light, and thus, $\boldsymbol{B}_\gamma$ has to be perpendicular to the magnetic moment $\boldsymbol{\mu}$ of the electron (and therefore the external magnetic field $\boldsymbol{B}$), so it can act as a tipping field to induce the spin flip.

In a more detailed analysis of the phenomenon (see Fig. 2.18), one finds that $\boldsymbol{\mu}$ does not align with the magnetic field, but precesses around $\boldsymbol{B}$, while $\boldsymbol{B}_\gamma$ oscillates in a direction perpendicular to $\boldsymbol{B}$. However, this uniaxial oscillation can be interpreted as a superposition of two circularly polarized fields that precess in opposite directions around $\boldsymbol{B}$. When $\boldsymbol{\mu}$ and $\boldsymbol{B}_\gamma$ are in resonance, $\boldsymbol{\mu}$ flips by precessing around $\boldsymbol{B}_\gamma$.

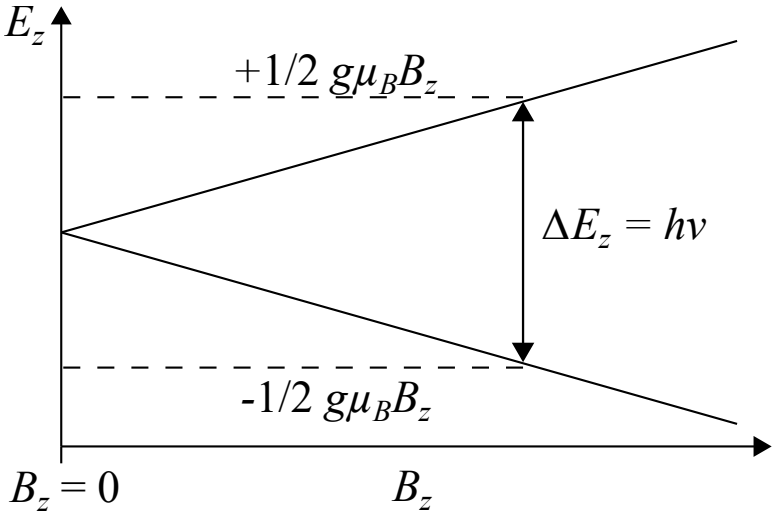

Fig. 2.17. Zeeman splitting of electron spins in a magnetic field. A transition from spin down to spin up state can be induced by absorption of a photon which meets the resonance condition from Eq. 2.41.

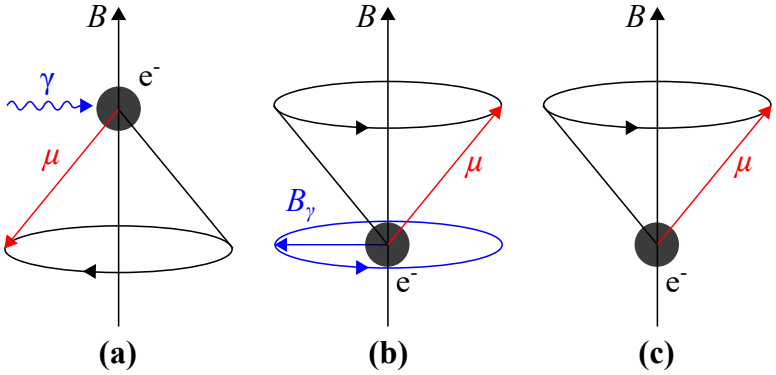

Fig. 2.18. (a) Orientation of the external magnetic field and the magnetic moment of the electron in the spin-down configuration, with $\boldsymbol{\mu}$ precessing around $\boldsymbol{B}$. A photon γ is about to interact with the electron e^-. **(b)** The magnetic field vector $\boldsymbol{B}_\gamma$ of the linearly polarized photon is oscillating perpendicularly to $\boldsymbol{B}$. The resonance frequency is met and $\boldsymbol{\mu}$ is flipped. **(c)** The electron is in the spin-up state after photon absorption.

In addition to energy conservation, the angular momentum L has to be conserved during the process, and in the case of graphene, this is also true for the pseudospin σ (a photon does not carry pseudospin). Hence, the quantum mechanical selection rules for ESR can be summarized as

$$\Delta s = 0, \qquad \Delta m_s = \pm 1, \qquad \Delta\sigma = 0, \qquad \Delta L = 0. \tag{2.42}$$

Since, in the case of graphene, the Maxwell-Boltzmann distribution dictates

that the spin down state is energetically favorable, more electrons are generally found in this state which results in a net absorption of radiation. The Maxwell-Boltzmann distribution for the ratio of electrons with opposing spins is given by

$$\frac{N_\uparrow}{N_\downarrow} = \exp\left(-\frac{\Delta E_Z}{k_B T}\right) = \exp\left(-\frac{g\mu_B B_z}{k_B T}\right), \tag{2.43}$$

with $N_\uparrow$ and $N_\downarrow$ representing the number of spin-down and spin-up states, respectively, and k_B being the Boltzmann constant. Assuming a g-factor of 1.952 [20] for graphene and a moderate magnetic field of 1 T yields a temperature-dependent distribution of the electron spins, which is shown in Fig. 2.19. Up to temperatures of around 20 K, the ratio is clearly distinguishable from 1. However, even for higher temperatures there is a slight imbalance of carriers, which, e.g., is exploited in magnetic resonance imaging, a technique used in the medical field.

In a typical ESR measurement, a sample is placed into a variable magnetic field, irradiated by microwaves of constant frequency, and the absorption is measured by a spectrometer. The expected line shape [68] of an ESR spectrum is shown in Fig. 2.20.

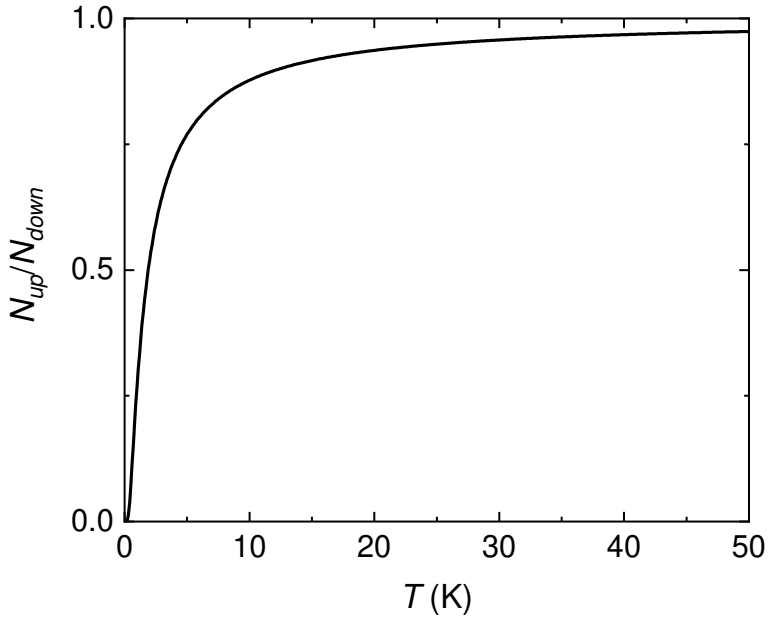

Fig. 2.19. Maxwell-Boltzmann distribution in graphene for the ratio of spin-up and spin-down electrons in dependence of temperature, assuming $B_z = 1$ T and $g = 1.952$ [20].

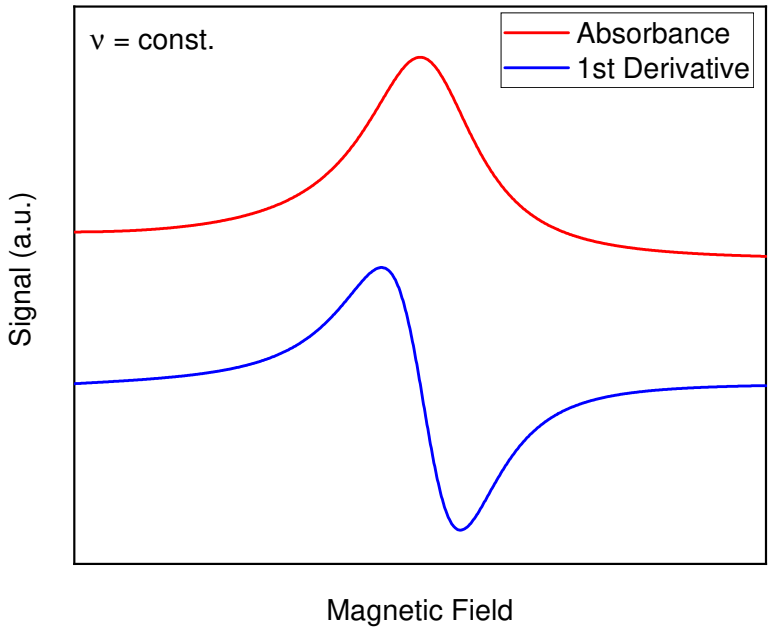

Fig. 2.20. Expected line shape of a typical ESR measurement at constant frequency ν, with the absorption spectrum (red) and its derivative (blue).

Resistively Detected ESR in Graphene

In order to resolve the band structure of graphene in the vicinity of the SOC gap via RD-ESR, the Fermi energy should lie within the thermal energy range $\Delta E = k_B T$ of the Dirac points. Thus, when a magnetic field is applied, a spin-selective excitation of electrons from the lower Dirac cone to the upper one is possible, while still respecting selection rules. The conductance (resistance) then increases (decreases) under resonant absorption due to the activation of charge carriers, resulting in a measurable effect.

However, in the RD-ESR spectra, various sources which might obscure the resonance signal have to be considered. Since in such an experiment, microwave radiation is applied to a sample at low temperatures ($T \leq 4\,\mathrm{K}$), an overall thermal increase of the conductance is observed as more charge carriers become available at the Fermi energy. The changes in resistance due to thermal activation can mask the changes resulting from resonant absorption. Moreover, two carrier transport and WL effects might result in dominant signals, depending on the magnetic field strength, i.e., two-carrier transport at high fields, and WL at low fields.

A simple method to enhance the resonance signal is to perform a background measurement, which is subtracted from the subsequently acquired ESR data.

Ideally, in addition to the resonance signal, only the WL feature will remain in the adjusted data due to the temperature sensitivity of the WL effect.

2.4.2 The *g*-Factor

The g-factor of graphene can be determined by finding the dependence of the radiation frequency ν on the resonance peak position in magnetic field B_{res} (see Eq. 2.41), while already accounting for a possible energy gap Δ:

$$g = \frac{h}{\mu_B}\frac{\partial \nu}{\partial B_{res}} + \Delta. \tag{2.44}$$

The zero-field gap might occur when an electron is placed into an atomic lattice, e.g., due to spin-orbit coupling corrections discussed in Section 2.1. Moreover, the g-factor is not always isotropic in a lattice since electrostatic fields can shift the orbital energies. Interaction between magnetic impurities can also influence the resonance field and cause variations in the g-factor. Thus, a description as a tensor needs to be introduced:

$$\hat{g} = \begin{pmatrix} g_x & 0 & 0 \\ 0 & g_y & 0 \\ 0 & 0 & g_z \end{pmatrix}. \tag{2.45}$$

From this tensor, the effective g-factor can be derived as

$$g_{\text{eff}} = \sqrt{g_x^2 \sin^2\Theta\cos^2\Phi + g_y^2 \sin^2\Theta\sin^2\Phi + g_z^2\cos^2\Theta}, \tag{2.46}$$

with the angles Θ and Φ between magnetic field and the principal axis of $\hat{g}$. In essence, angle dependent ESR measurements of the g-factor give access to the tensor $\hat{g}$ of the system. Note that the g-factor which is determined by ESR differs from the enhanced g-factor that can be derived from the coincidence technique (typically employed in semiconductor physics), where quantum oscillations of the conductivity are studied in tilted magnetic fields. Here, the spin splitting is enhanced by exchange interactions, resulting in higher values of g [69–71].

2.4.3 Spin Relaxation

Spin lifetimes in graphene are theoretically predicted to be in the microsecond regime [72, 73], however, numerous experimental results prove a discrepancy of a few orders of magnitude and range from tens of picoseconds to some

nanoseconds [74–80]. The origin of this discrepancy is the subject of many discussions [79, 81–86], and Han *et al.* (2014) [81] give a structured overview on the possible spin relaxation mechanisms and examine their involvement in the reduced lifetimes.

Mainly two processes have been attributed to spin relaxation in the past, the Elliott-Yafet and the Dyakonov-Perel mechanisms.

In the Elliott-Yafet relaxation, spin flips are induced by scattering processes, since SOC mixes the spin-up state with the spin-down state in the eigenstates of the tight-binding Hamiltonian. The component of the opposite spin is rather small in each respective spin state, but is sufficient to induce a flip after up to a million scattering events, even if nominally, the impurity or phonon scattering process is spin-conserving. This results in a spin relaxation rate of

$$1/\tau_{EY} \approx \lambda_I/(E_F\tau_p), \tag{2.47}$$

where τ_p is the elastic scattering time (see Section 2.3.3), and λ_I is the SOC parameter (see Section 2.1.4). Calculating the spin relaxation time with characteristic values for graphene results in $\tau_{EY} \approx 1\,\mu s$ [81].

For the Dyakonov-Perel mechanism, spin precession between two scattering events is assumed and SOC results in a Rashba-like field along which the electron spin precesses. With each scattering event, the SOC field changes its orientation randomly and thus, the precession aligns accordingly. Simply put, the higher the scattering rate, the more random the precession becomes and the faster the spin information is lost. In contrast to the Elliott-Yafet mechanism, the spin relaxation rate increases proportionally with the elastic scattering time:

$$1/\tau_{DP} \approx \lambda_R^2\tau_p, \tag{2.48}$$

with λ_R being the Rashba SOC parameter (see Section 2.1.5). Again, with characteristic values for graphene, one receives $\tau_{DP} \approx 1\,\mu s$ [81], which is of equal magnitude as the Elliott-Yafet mechanism.

In experimental studies, the Elliott-Yafet relaxation has been found to be dominant in monolayer graphene [76, 77, 79] as the spin lifetime τ_s increases with the diffusion constant D of the Drude model, where $D = 1/2v_F l_m$, such that $\tau_s \propto \tau_p$.

For bilayer graphene, the opposite has been observed ($\tau_s \propto 1/\tau_p$), and hence, the Dyakonov-Perel spin relaxation seems to be the governing mechanism here [79, 87].

However, some studies exist claiming that the Dyakonov-Perel relaxation in monolayer graphene [88] and Elliott-Yafet in bilayer graphene [89], respectively, are dominant, emphasizing that this topic remains unsolved.

In addition to the two types of spin relaxation discussed above, another mechanism has been proposed by Tuan *et al.* (2014) [82], the pseudospin-driven relaxation. Here, the entanglement of spin and pseudospin (see Section 2.1.4) results in fast spin dephasing in the ballistic transport limit, i.e., in pristine graphene, which, however, has not yet been experimentally realized.

Furthermore, the spin relaxation rate seems to be insensitive to the underlying substrate [90–93] and thus charge carrier mobility [94], which excludes charged impurity scattering as the source of short spin lifetimes.

One of the few possibilities left are scattering events due to magnetic moments that can arise from adatoms or vacancies [95, 96]. These magnetic moments can induce a spin flip similar to the process illustrated in Fig. 2.17, yielding spin relaxation times of around 100 ps with only 1 ppm of magnetic impurities.

In summary, the topic of spin relaxation in graphene is still worth investigating.

Ultimately, in an ESR experiment, the spin lifetime τ_s can be extracted by calculating

$$\tau_s = \frac{\hbar}{2\Delta E_{res}}, \tag{2.49}$$

where

$$\Delta E_{res} = h\frac{\partial \nu}{\partial B_{res}}\Delta B_{res}, \tag{2.50}$$

with ΔB_{res} being the half-width of the resonance peak (see Fig. 2.18). This yields access to the spin diffusion length

$$\lambda_s = \sqrt{D\tau_s}. \tag{2.51}$$

3 Sample Fabrication

In this chapter, the fabrication methods for the graphene samples presented in this work are discussed in detail. This mainly includes in-house substrate preparation and processing of graphene which was produced by chemical vapor deposition (CVD). The intentions behind choosing CVD graphene are to produce large-scale samples with the aim of facilitating mass-production in the future. The procedure described in the following sections is based on a wet transfer method and was established by X. Liang *et al.* (2011) [97] and T. Lyon *et al.* (2017) [19]. Additionally, various substrate geometries and the corresponding preparation methods are described.

3.1 Graphene Cleaning

The CVD graphene used in the majority of the presented experiments is provided on a sheet of Cu foil by the company Graphenea [98] (see Fig. 3.1a). In the first step, the graphene is spin-coated with a protective layer of "Microchem 950 PMMA A4" at 6000 rpm for one minute and dried at room temperature. It is then cut into pieces of $\sim 1\,\text{cm} \times 1\,\text{cm}$ size which are placed to float on a 1:20 solution of $Fe_3(NO_3)_3 \cdot 9H_2O$ and deionized (DI) water for ten hours in order to etch away the Cu (see Fig. 3.1b). Afterwards, the graphene/PMMA stack is cleaned several times in pure DI water for a minimum of five minutes each time to eliminate residues of the etching solution. Any remaining inorganic contaminants are subsequently removed by placing the graphene into a 1:1:60 solution of $HCl/H_2O_2/H_2O$ for 15 minutes. After several intermediate cleaning steps in DI water, organic contaminants are removed in a 1:1:300 solution of $NH_4OH/H_2O_2/H_2O$ for five minutes. In the last step, the graphene/PMMA stack is cleaned again in DI water before it is ready to be transferred onto a substrate, as shown in Fig. 3.1c.

3.2 Substrate Preparation

The substrate for all the in-house fabricated samples is a *p*-doped Si wafer with a 300 nm thick layer of thermally grown SiO_2 on top. While other substrate choices would be possible without significantly modifying the outlined fabrication procedure, SiO_2 on Si yields the advantage of being an affordable and standard material in the semiconductor industry as well as offering the opportunity to apply a back-gate voltage due to the insulating oxide.

The wafer is cleaved into $\sim 1.2\,\text{cm} \times 1.2\,\text{cm}$ pieces, i.e., slightly bigger than the graphene flakes in order to avoid overlap of the graphene with the substrate edges, which can cause damage to the graphene layer. The wafer is then sonicated and cleaned in acetone and isopropanol. At this point, lithography can be employed to pattern the surface in any desired manner. The different sample geometries and related procedures are described in the next section, however, for now a flat substrate is assumed.

The wafer is exposed to an O_2 plasma in a "TePla 100-E Plasma System" at 300 W for ten minutes. This process makes the substrate more hydrophilic and enables the graphene to adhere to the surface more readily and reduces breakage [19]. For optimal results, the transfer of the graphene onto the substrate should be conducted within one minute after the plasma treatment [99]. The floating graphene/PMMA stack is scooped up from underneath the surface with the wafer and then dried in an oven at 150 °C for 15 minutes.

For optimal removal of the protective PMMA layer, the sample is placed into acetic acid [100] and then cleaned with acetone and isopropanol. The result is shown in Fig. 3.1d.

3.3 Hall Bar Definition

For the definition of a Hall bar structure, the sample is first spin-coated with lift-off remover "Microchem LOR 5A" at 6000 rpm for one minute and then baked at 160 °C for another minute, followed by a layer of photoresist "Microchem S1805" spin-coated at 6000 rpm and a baking step at 115 °C for one minute each. The sample is exposed to a contact pattern of a Hall bar geometry, as, e.g., shown in Fig. 3.4a, by a $13\,\text{mWcm}^{-2}$ UV lamp for 4.2 seconds and it is developed in "Microchem MF-319" for 45 seconds. A 10 nm thick adhesion layer of Ni and 100 nm of Au are deposited to form Ohmic contacts (see Fig. 3.2). During lift-off in acetone, only the photoresist along with the excess Au is

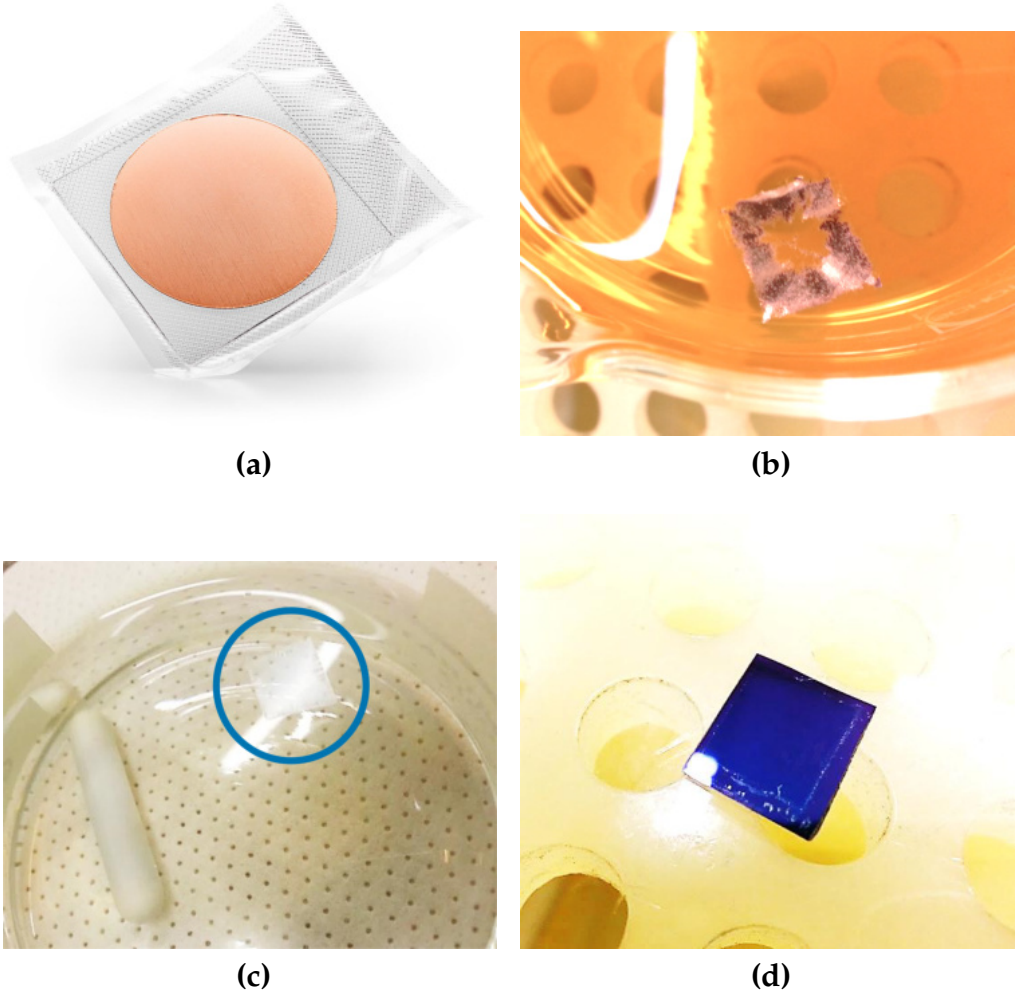

(a) **(b)**

(c) **(d)**

Fig. 3.1. Graphene at different stages in the fabrication process. **(a)** Monolayer graphene on Cu foil supplied by Graphenea [98]. **(b)** Cu/graphene/PMMA stack in the $Fe_3(NO_3)_3$ etching solution with the center region already etched away. **(c)** Clean graphene/PMMA in DI water. **(d)** Graphene transferred onto SiO_2/Si with the PMMA removed.

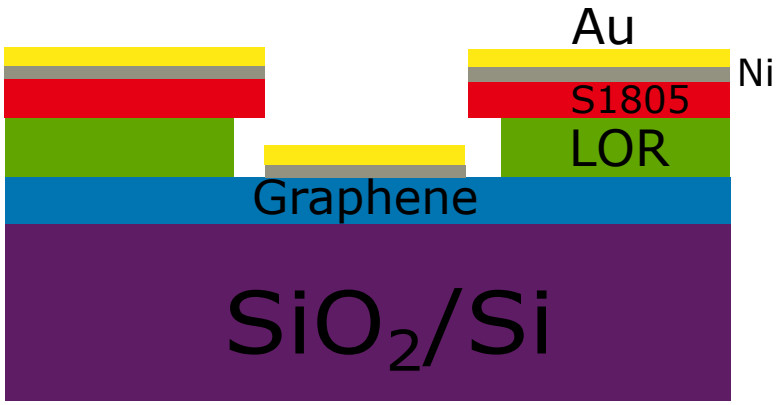

Fig. 3.2. Side cut of the sample after metal deposition. The LOR forms an undercut to assure well-defined Ni/Au contacts (center), while also protecting the graphene during the subsequent lift-off (sides).

removed, while the layer of LOR protects the graphene from damage. Note that it is of utmost importance to never sonicate the sample when performing lift-off, otherwise the graphene will be severely damaged; it is advised to rather squish acetone onto the submerged sample with a one-way pipette. Once the lift-off is complete, the LOR is dissolved in "Microchem Remover 1165".

In order to etch away the excess graphene, the sample undergoes a photolithography procedure with identical parameters as described above, with the difference of applying a thicker resist, "Microchem S1813", as well as a different exposure pattern, i.e., one that compliments the Hall bar structure (see Fig. 3.4b). The graphene is then removed by placing the sample into the aforementioned O_2 plasma for four minutes at 300 W. A summary of the entire work flow is shown in Fig. 3.3.

3.4 Sample Geometries

In order to study the influence of extrinsic factors on the electronic structure of graphene, samples of various geometries are prepared. Detailed information about all the samples presented in this work is listed in this section, and in addition, fabrication steps complementing the ones outlined above are described if necessary. An overview of all the samples is given in Tab. 3.1.

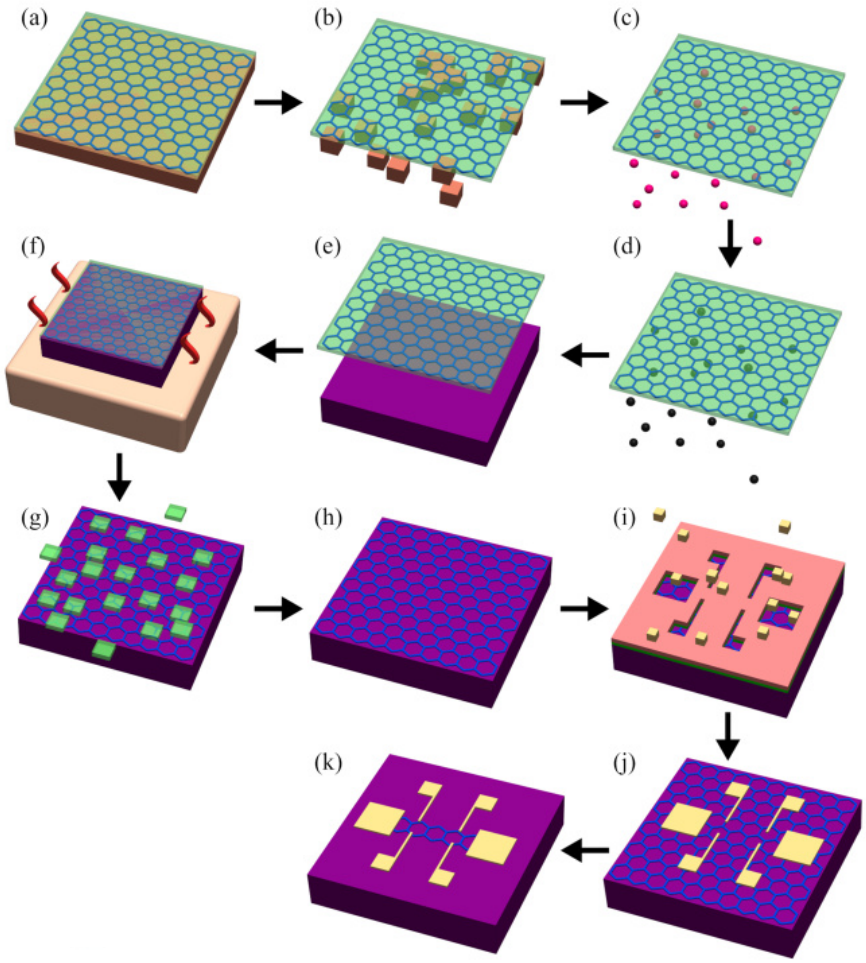

Fig. 3.3. Work flow diagram of the sample fabrication. The sample is spin-coated with PMMA **(a)**, before the copper is etched away **(b)**, and the graphene is cleaned of inorganic **(c)** and organic **(d)** contaminants. It is then transferred onto an SiO_2/Si wafer **(e)**, dried **(f)**, and the PMMA is removed **(g)**, with the result shown in **(h)**. Ohmic contacts are deposited **(i)** and lift-off is performed **(j)**, before the excess graphene is removed and the sample is completed **(k)**.
Reprinted figure from T. J. Lyon *et al.* (2017) [19], with permission from AIP Publishing.

Tab. 3.1. Overview of the three sample types. They differ in terms of the contact layout, the structure of the substrate, and the size of the graphene sheet.

Component	Substrate Structure	Period (nm)	Length (µm)	Width (µm)
1	Corrugation	200	200	22
2	Flat	None	1920	66
3	Pt/Co/Pt Nanodot Array	70	200	22

3.4.1 Sample 1

Sample 1 is a 200 µm × 22 µm graphene sheet in a classical Hall bar geometry with a distance of 100 µm between the inner longitudinal probe contacts and of 16 µm between the transverse contacts, as shown in Fig. 3.4.

The SiO_2 substrate is corrugated, with a period of 200 nm and a depth of $\sim$ 20 nm, resulting in an effective one-dimensional potential along the Hall bar (see Fig. 3.5). The trenches are patterned prior to the graphene transfer, which requires electron beam lithography (EBL) due to the dimensions of the structure. In order to make the EBL process compatible with the photolithography of Section 3.3, alignment markers are necessary.

Therefore, the alignment markers are patterned by spin-coating the 1.2 cm × 1.2 cm wafer piece from Section 3.2 with "Microchem S1805" at 6000 rpm for one minute and baking it at 115 °C for another minute. Afterwards, it is exposed to the photolithography mask shown in Fig. 3.6a, and developed in "Microchem MF-319" for 45 seconds. Subsequently, a 40 nm layer of Au/Pd is sputtered onto the substrate, before lift-off is performed.

The EBL recipe used here requires to spin-coat the sample with "Microchem 950 PMMA A4" at 6000 rpm for one minute, followed by a baking step at 160 °C for two minutes. The sample is exposed to the pattern shown in Fig. 3.6b with an area dosage of 100 $\mu C/cm^2$ using a "Zeiss SUPRA 55" scanning electron microscope (SEM), before the sample is developed in "Allresist Developer AR 600-56" for five minutes. Note that after development, isopropanol is commonly used as a stopper for EBL resists as opposed to DI water for photolithography resists.

The PMMA structure on top of the substrate can now be used as a mask for reactive ion etching, which is a mostly unidirectional etching process, and hence, is preferred over more uniform processes like HF wet etching.

A "Sentech ICP-RIE plasma etcher SI 500" with an ICP power of 225 W,

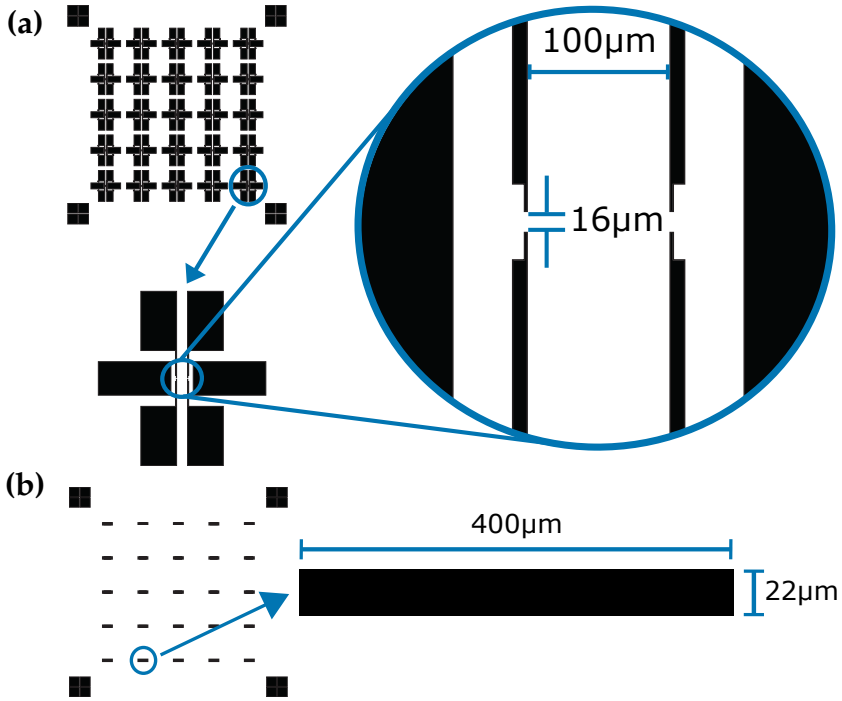

Fig. 3.4. (a) Contact pattern for an array of Hall bar structures for the whole wafer and the zoom-in to one single structure. **(b)** Layout which complements the pattern from (a) to protect the graphene between the contacts during the etching process (see Fig. 3.3k), with the whole wafer mask on the left, single bar on the right. Note that the protected area of 400 µm length is larger than the distance of 200 µm between the outer contacts to ensure overlap between the graphene and the contacts.

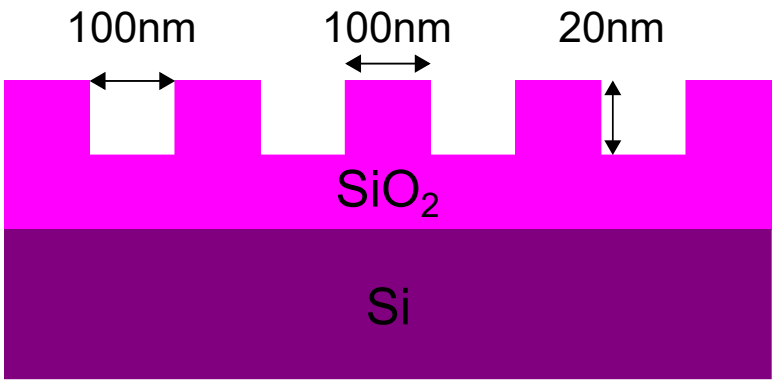

Fig. 3.5. Schematic side view of the substrate of sample 1. Trenches of the indicated dimensions are etched into the SiO_2. Not to scale.

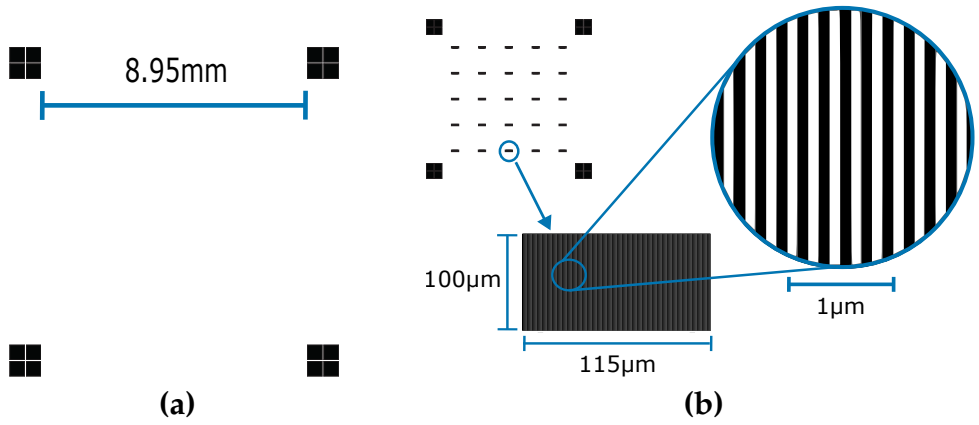

Fig. 3.6. (a) Alignment marker pattern to ensure compatibility of EBL and photolithography processes. **(b)** EBL structure with a 5×5 array of trench patterns with a 200 nm period.

an RF power of 45 W, a C_4F_8 gas flow of 20 sscm, and an etch time of 15 seconds is used to etch trenches of $\sim$ 20 nm depth into the SiO_2. As a general empirical guideline, the etch depth should not exceed $\sim$ 20 % of the trench width, since otherwise the graphene tends to break due to stress when put on such a structure.

After removing the PMMA in acetone and following the remaining steps described in Section 3.2, the substrate is ready for graphene transfer and Hall bar definition.

An optical image of the finished sample 1 is shown in Fig. 3.7, along with an SEM image and an atomic force microscopy (AFM) trace to verify the geometry of the trenches.

3.4.2 Sample 2

Sample 2 is a flat 1.92 mm $\times$ 66 µm graphene sheet in a classical Hall bar geometry, and is one order of magnitude larger than sample 1. Additionally, a different contact layout for the Hall bar definition is used. Due to the availability of space, there are six inner contacts instead of four, and the longitudinal distance between two neighboring (opposing) contacts is 500 µm (60 µm), as shown in Fig. 3.8. An optical image of the finished sample is shown in Fig. 3.9.

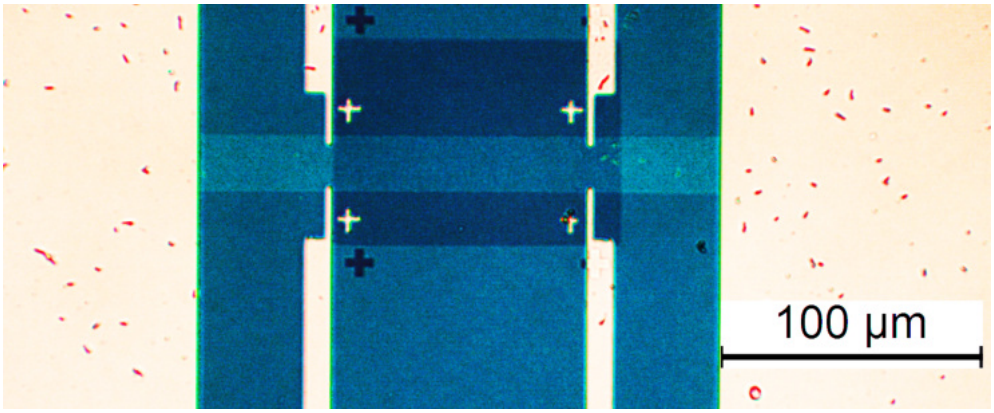

(a)

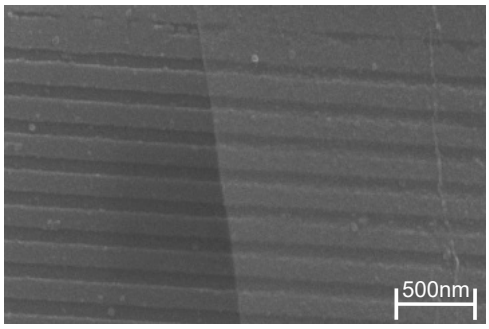

(b)

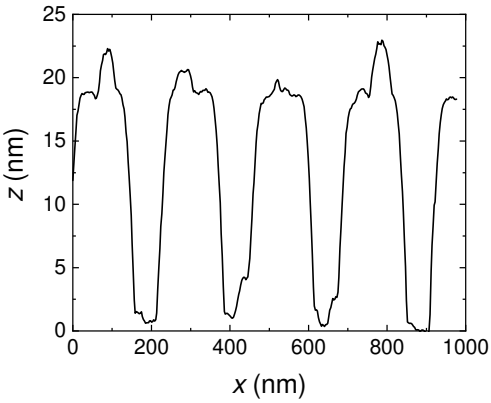

(c)

Fig. 3.7. (a) Optical micrograph of the finished sample 1. The Au contacts are shown in light yellow, while the three shades of blue are, from light to dark, the graphene bar, the flat substrate, and the etched corrugation underneath the graphene, respectively. Some small contaminants on the right side are visible, but they are sufficiently far away from the probing contacts. Contrast is enhanced for visibility. **(a)** SEM image of graphene on the corrugated pattern (light gray, right) and the pattern without graphene on top (dark gray, left). **(b)** AFM trace on an arbitrary spot of the corrugated structure. The average etch depth is $\sim 20\,\mathrm{nm}$.

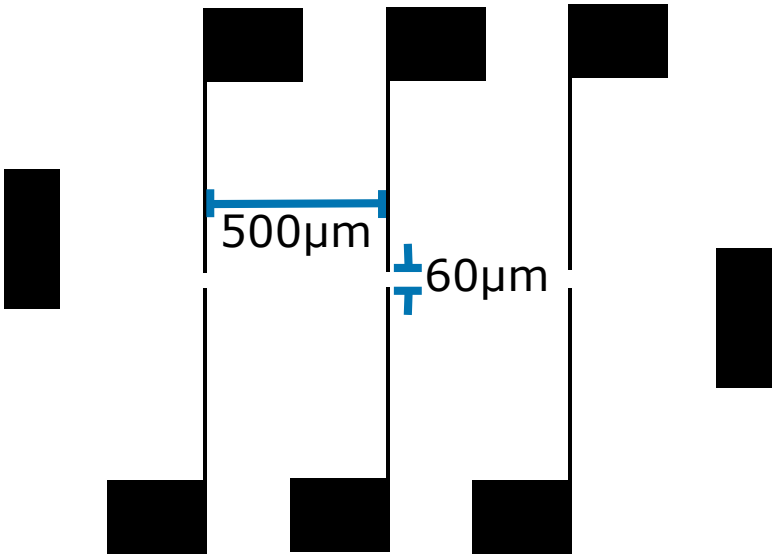

Fig. 3.8. Cutout of the photolithography mask for sample 2. The distance between the outer contacts is 1.92 mm, the other dimensions are as indicated.

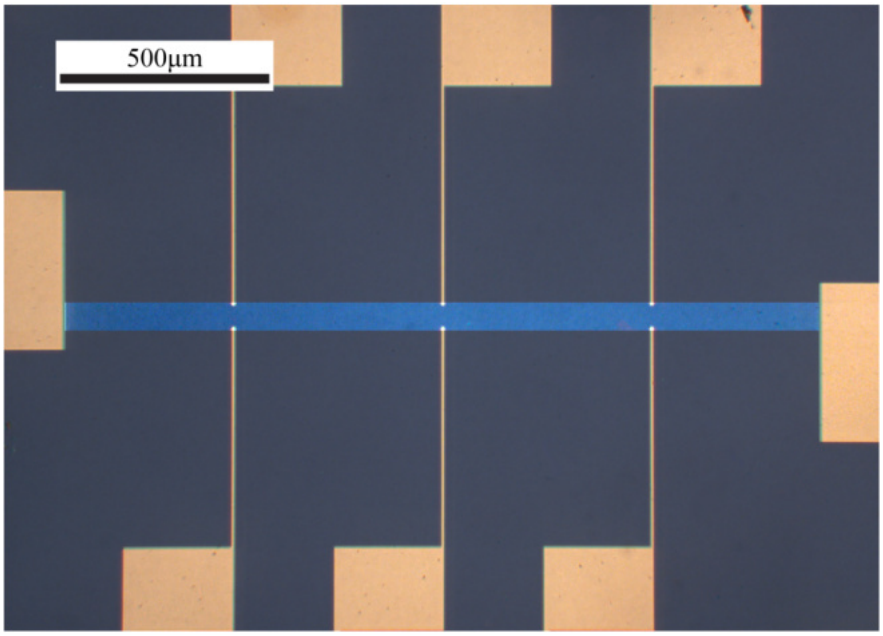

Fig. 3.9. Optical micrograph of sample 2 [46]. Dark and light blue denote substrate and graphene, respectively, while the Au contacts are shown in ocher. Considering the millimeter size of the graphene sheet, it is more or less free of any visible imperfections. Contrast is enhanced for visibility.

3.4.3 Sample 3

The substrate of sample 3 is a flat Si wafer with a 290 nm thick layer of thermally grown SiO_2 on top. Prior to the graphene transfer, magnetic nanodots are deposited on the substrate by the group of Prof. H. P. Oepen from the Universität Hamburg, Germany. The fabrication and characterization of these nanodots are detailed in the works of Stillrich *et al.* (2008) [101] and Neumann *et al.* (2012) [102], and a short outline of the fabrication processes is given in this section.

A Pt/Co/Pt film with perpendicular magnetic anisotropy and a total thickness of around 6 nm is deposited on the substrate via magnetron sputtering. Afterwards, diblock copolymer micelles with a SiO_2 core are used to create a closely packed array on top of the Pt/Co/Pt film. The average distance between the cores is around 70 nm. An O_2 etching step then removes the polymer and leaves only the SiO_2 cores on the surface, which can subsequently be used as a mask for ion milling. This transfers the structure of the cores to the magnetic film, and thus, an array of magnetic nanodots is produced. A schematic depiction of this process is shown in Fig. 3.10, while Fig. 3.11 is an SEM image of the final structure. It is apparent that the resulting dots exhibit a short-range hexagonal order, but the lack of any type of long-range order.

The graphene is then transferred onto the substrate and patterned into a Hall bar layout (200 µm × 22 µm) as outlined in Section 3.3, with the graphene being in contact with the magnetic nanodots. An optical micrograph of the final sample 3 is shown in Fig. 3.12.

3.5 Bonding and Sample Mount

Before the sample is glued into the chip carrier, the bottom of the carrier has to be cut off (see Fig. 3.13) to provide close-proximity access for the microwave frequency antenna, which is necessary for the ESR experiments. Thus, the sample is glued as close as possible to the cut, with the graphene Hall bar being parallel to the edge. "Leitsilber mit Pinsel 3 g Inhalt" from "Conrad Electronic SE" is used as glue, which is a conductive silver paint and thus allows for the application of a back-gate voltage during the measurements.

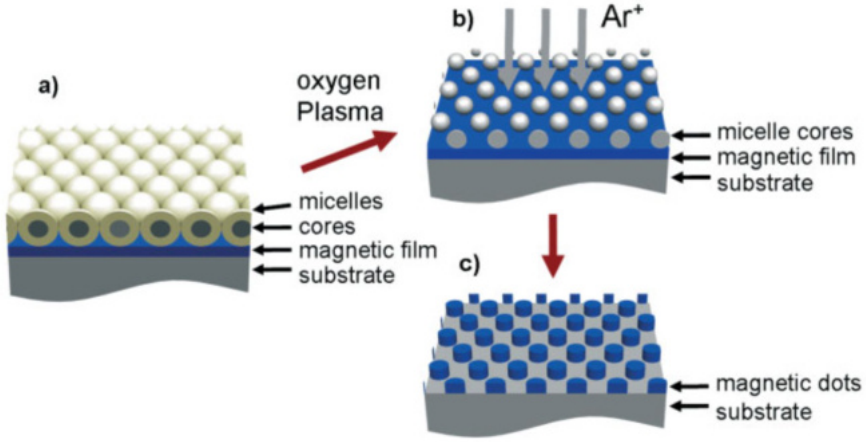

Fig. 3.10. Schematic depiction of the sample processing steps. **(a)** An array of diblock copolymer micelles with a SiO_2 core is placed on top of a $\sim$ 6 nm thick Pt/Co/Pt magnetic multilayer. **(b)** The micelles are etched away by O_2 plasma, leaving behind the SiO_2 cores. **(c)** The cores are used as a shadow mask to transfer their structure to the multilayer via ion milling, resulting in an array of magnetic nanodots.
Reprinted figure with permission from H. Stillrich, A. Frömsdorf, S. Pütter, S. Förster, and H. P. Oepen. Sub-20 nm Magnetic Dots with Perpendicular Magnetic Anisotropy. Advanced Functional Materials, 18.1, 76-81 (2008). Copyright 2008 WILEY-VCH Verlag GmbH & Co. KGaA, Weinheim [101].

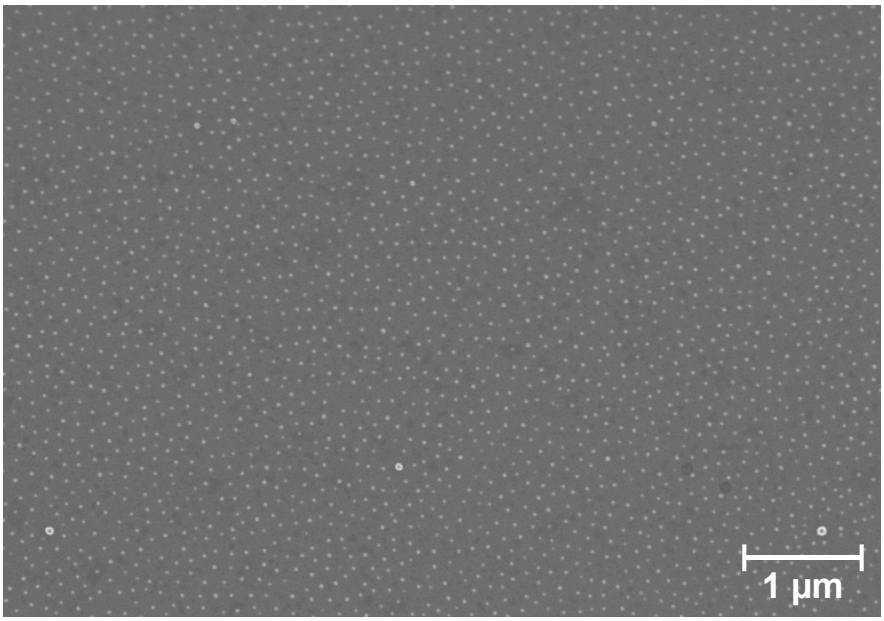

Fig. 3.11. SEM image of an array of Pt/Co/Pt nanodots (light gray dots) on top of a SiO_2/Si substrate (dark gray). The average distance between the dots is $\sim$ 70 nm and a hexagonal short-range order is discernible.

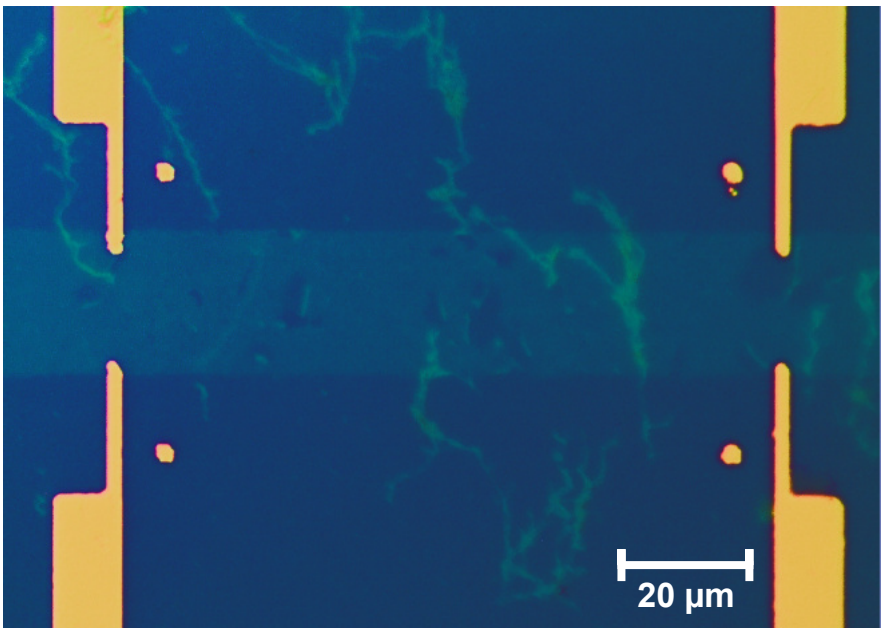

Fig. 3.12. Optical micrograph of the finished sample 3. Dark and light blue denote substrate and graphene, respectively, while the Au contacts are shown in dark yellow. Some tears in the graphene are visible as dark blue patches in the Hall bar, as well as some PMMA residues (turquoise).

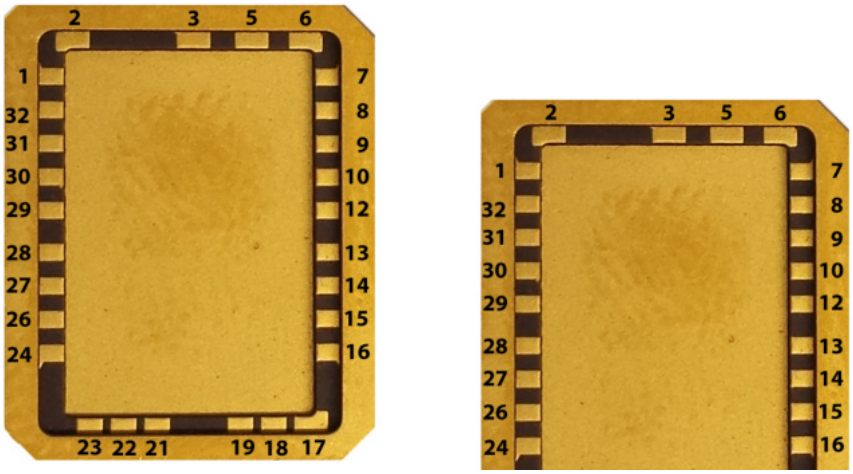

(a) **(b)**

Fig. 3.13. (a) Leadless ceramic chip carrier with Au contacts. **(b)** Chip carrier with the bottom part cut off.

Once the glue has dried, a lot of care should be taken during the wire bonding procedure to avoid cracks in the thin oxide layer of the wafer, and thus leakage currents when applying a back-gate voltage. Instead of bonding directly from

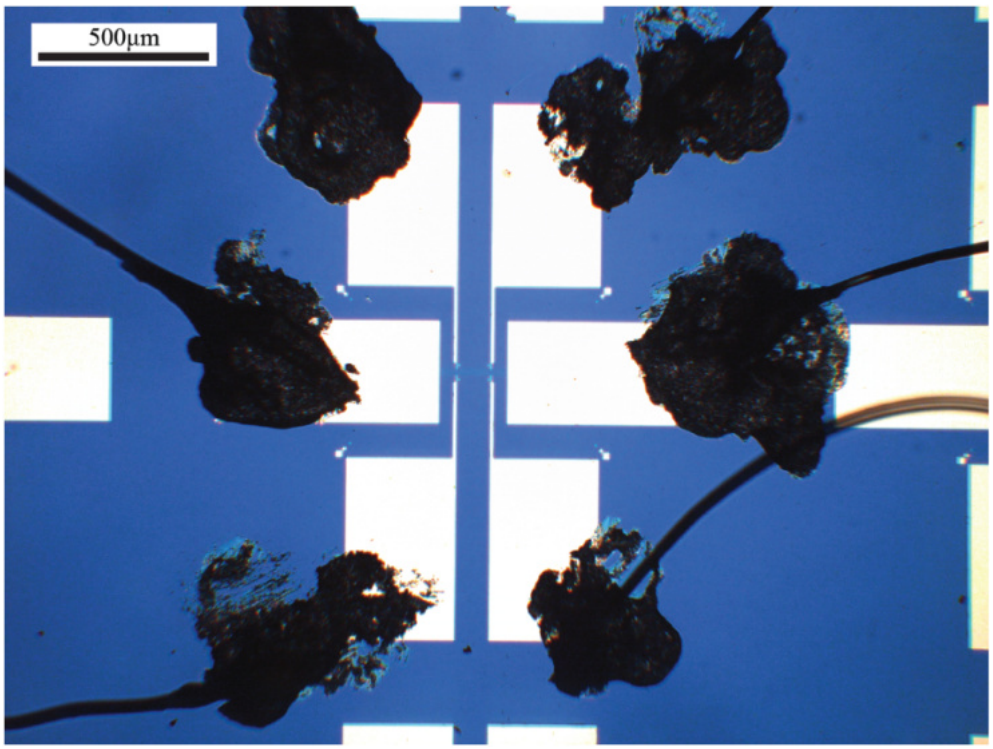

Fig. 3.14. Optical micrograph of the bonded sample 1. The wires are glued to the Au contacts pads with small drops of conductive silver paint.

the Au contact pads of the chip carrier to those of the Hall bar, it is advised to bond from the pads of the carrier to the bottom area of the carrier in the vicinity of the Hall bar. Subsequently, the latter bond should be detached, the wire bent manually onto the desired pad of the Hall bar, and finally glued to said pad with a small drop of silver paint. As an example, the successfully bonded sample 1 is shown in Fig. 3.14.

3.5.1 Thermal Annealing

Thermal annealing is an essential step in the fabrication of high quality CVD graphene samples, as it removes charged impurities, such as water [1], from the surface and therefore shifts the CNP close to zero back-gate voltage, which is illustrated in Fig. 3.15. A detailed discussion regarding the benefits of thermal annealing of the described samples was presented by T. Lyon *et al.* (2017) [19].

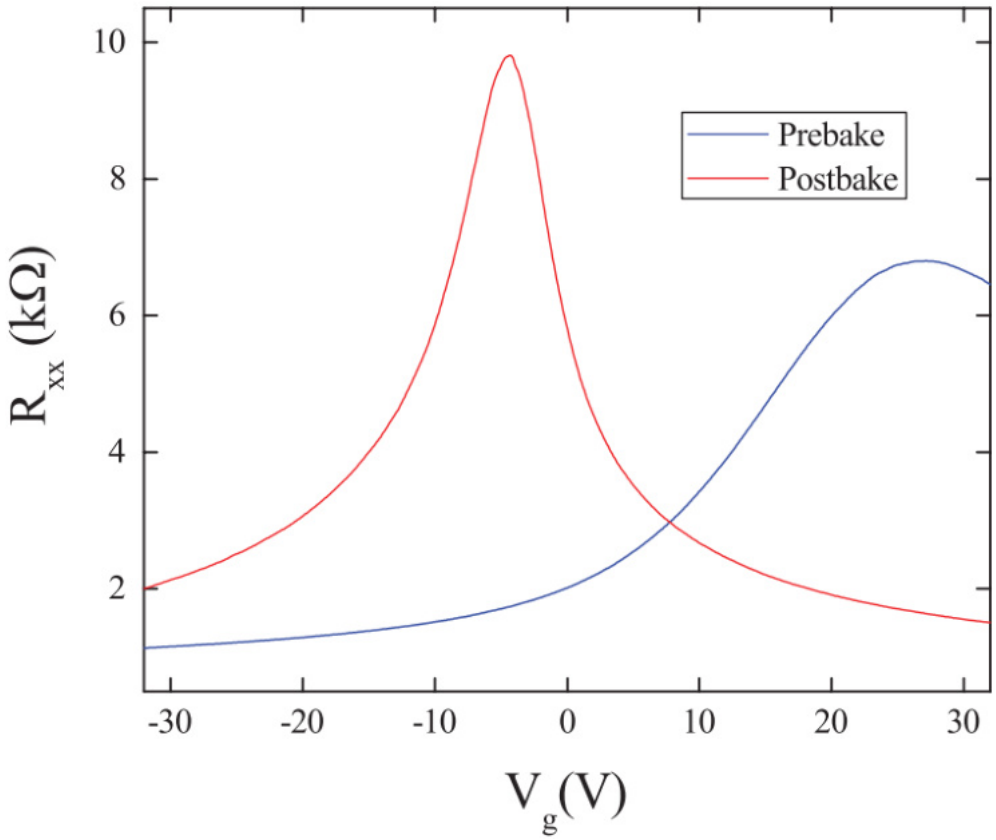

Fig. 3.15. Total sample resistance versus back-gate voltage before (blue) and after (red) the annealing step. The CNP shifts from $V_{g,pre} = 27\,\mathrm{V}$ to $V_{g,post} = -4\,\mathrm{V}$ while the peak resistance increases substantially, which indicates that impurities responsible for *p*-doping of the graphene, e.g., water [1], have been removed during annealing.
Reprinted figure from T. J. Lyon *et al.* (2017) [19], with permission from AIP Publishing.

There are two thermal annealing steps: First, the sample is placed into a rapid thermal annealing oven under vacuum and baked at 350 °C for 16 hours. Second, it is quickly removed and placed into a probe and baked in a tube oven under vacuum at 130 °C for 72 hours. Since the probe can be sealed, the sample is not exposed to atmosphere while it is placed from the oven into the measurement setup. However, a small amount of (inert) He exchange gas is introduced into the probe to speed up the sample cool-down. An alternative to the annealing steps would be the introduction of a capping layer to prevent the graphene from adsorbing impurities, but empirically, such a layer has negatively influenced the ESR signal in graphene.

4 Experimental Equipment

This chapter describes the various experimental setups that are used to perform low-temperature magnetoresistance and RD-ESR measurements of the samples presented in Chapter 3. All cryostat systems are from the company "Oxford Instruments", and are called "Hermes", "Kronos", and "Prometheus" for easier referral in the text. The systems are detailed with their respective features and temperature ranges, followed by the corresponding electrical equipment, i.e., lock-ins, frequency generators, and source measure units.

4.1 Hermes: Cryostat with 4.2 K Constant Temperature

Hermes is a liquid ^{4}He cryostat with a superconducting magnet which can reach fields of $|B| = 8\,\mathrm{T}$. The temperature is kept constant at 4.2 K for the measurements presented in this work. The probe for this system is placed into the liquid He bath, but it can be evacuated to a pressure of $\sim 1 \cdot 10^{-3}$ mbar which is essential to the sample quality (see Section 3.5.1). The probe features a high-frequency semi-rigid coaxial cable ending in a loop antenna close to the sample mount (see Fig. 4.1). Through this antenna, a microwave frequency signal can be applied during the RD-ESR measurements. A schematic of Hermes and the probe is shown in Fig. 4.2.

4.2 Kronos: Cryostat with Variable Temperature Insert

Kronos is a cryostat with a variable temperature insert (VTI), i.e., the space for the probe is thermally separated from the liquid He bath, however, the He flow into that space can be controlled via a needle valve. By pumping on the sample space and adjusting the He flow, it is possible to reach temperatures down to 1.4 K, as depicted in the phase diagram in Fig. 4.3. The superconducting magnet is capable of producing fields of $|B| = 10\,\mathrm{T}$. Similar to Hermes, the probe for this system can be evacuated to $\sim 1 \cdot 10^{-3}$ mbar and features a coaxial line with an antenna for microwave frequency transmission to the sample. A schematic drawing of Kronos is shown in Fig. 4.4.

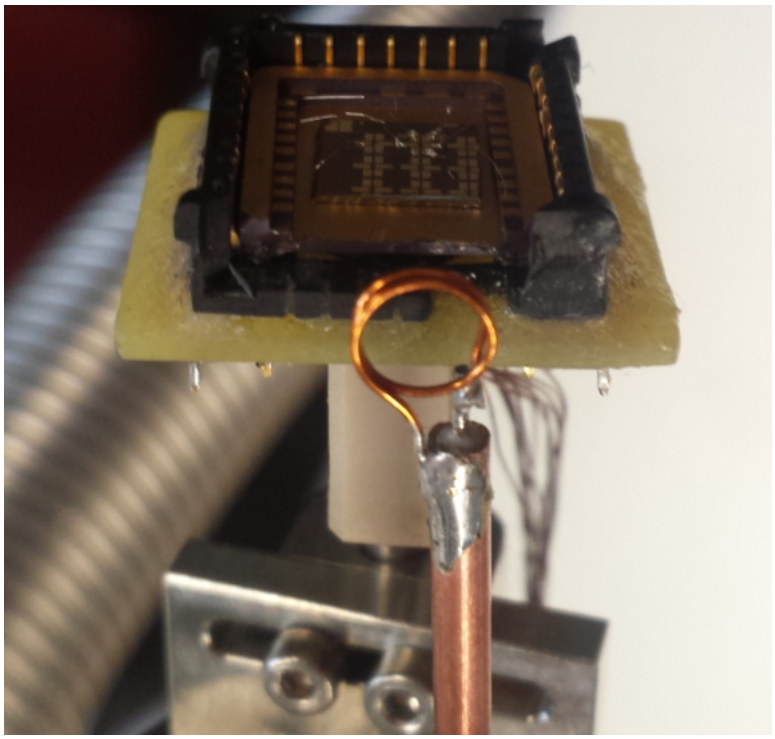

Fig. 4.1. Picture of the probe with the loop antenna next to a sample.

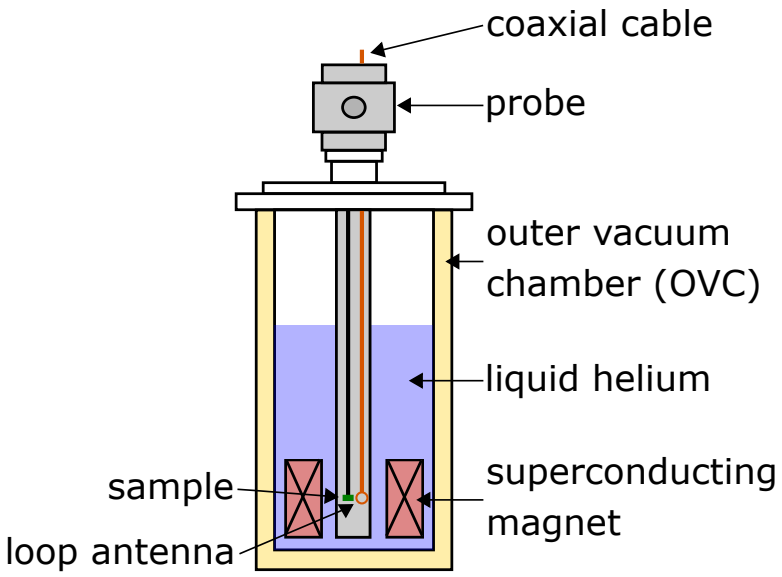

Fig. 4.2. Schematic drawing of the Hermes cryostat with the probe inside.

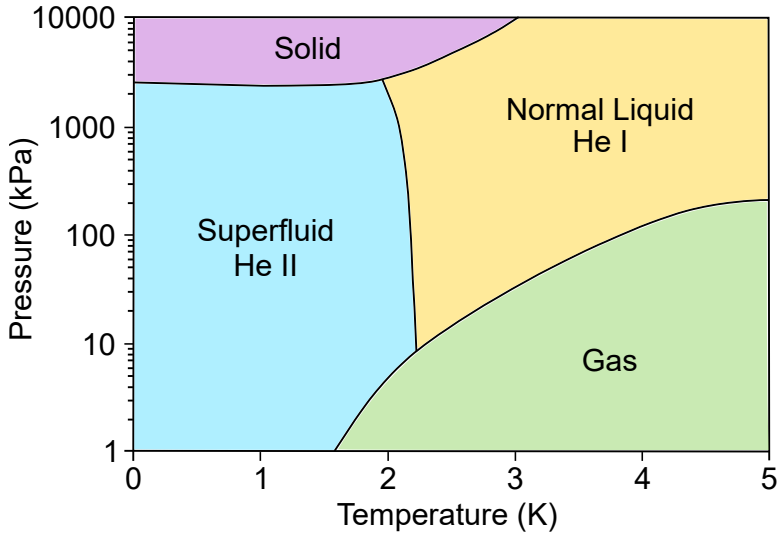

Fig. 4.3. Phase diagram for ^{4}He [103]. At pressures of around 10 mbar (1 kPa), the He vapor reaches temperatures of $\sim$ 1.4 K.

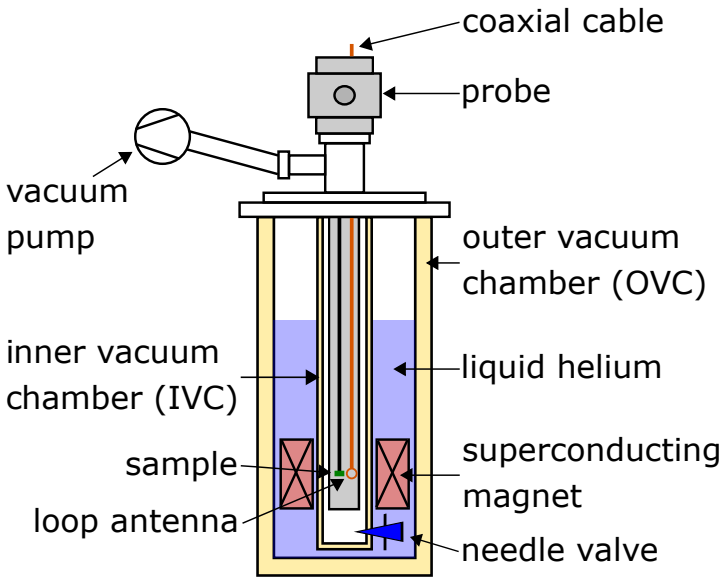

Fig. 4.4. Schematic drawing of the Kronos cryostat with the probe inside.

4.3 Prometheus: Cryostat with Variable Temperature Insert and Vector Magnet

Prometheus is a cryostat with a VTI, but in contrast to Kronos, a heating coil is wrapped around the needle valve. Since all the He entering the sample

space passes the heater, Prometheus enables access to temperatures ranging from 1.4 K to room temperature. Additionally, the system is equipped with a vector magnet with x-, y-, and z-components (the magnetic field orientation with respect to the sample will be described in a following chapter). Thus, through superposition, a sphere with a radius of up to $|B| = 1\,\mathrm{T}$ can be swept. A measurement with only a z-component can be performed to a maximum field of $|B| = 7\,\mathrm{T}$.

The probe for Prometheus has a microwave antenna, but no vacuum shield, resulting in a slightly different second annealing step: The sample has to be annealed in a separate vacuum tube and afterwards always kept under a N_2 atmosphere using a glove bag, then mounted into the probe and inserted into the VTI. A schematic drawing of Prometheus is shown in Fig. 4.5.

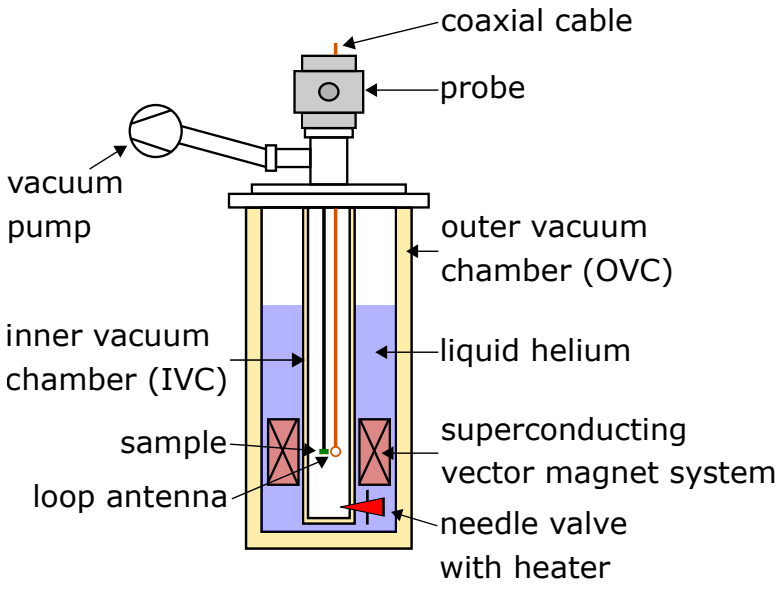

Fig. 4.5. Schematic drawing of the Prometheus cryostat with the probe inside.

4.4 Frequency Generators and Antennas

In the experimental setups where the probe features an antenna for microwave signal transmission, i.e., Hermes, Kronos and Prometheus, there are frequency generators of the type "Agilent Technologies E8257D PSG Microwave Analog Signal Generator". They have specified frequency ranges from 250 kHz to either 40 GHz or 67 GHz, depending on the purchased option, and the resolution is 0.01 Hz.

The signal output is a 1.85 mm connector, and via an adapter to SMA, the signal is transferred to the 50 Ω coaxial cable in the respective probes. Experiments have shown that a noticeable signal is only transmitted to the graphene samples for frequencies of up to $\sim$ 40 GHz, most likely due to the frequency limitations of the coaxial cables and SMA connectors, where the component with the lowest rating is the SMA connector at 18 GHz. Since the absorption spectra for the three systems are qualitatively similar, a

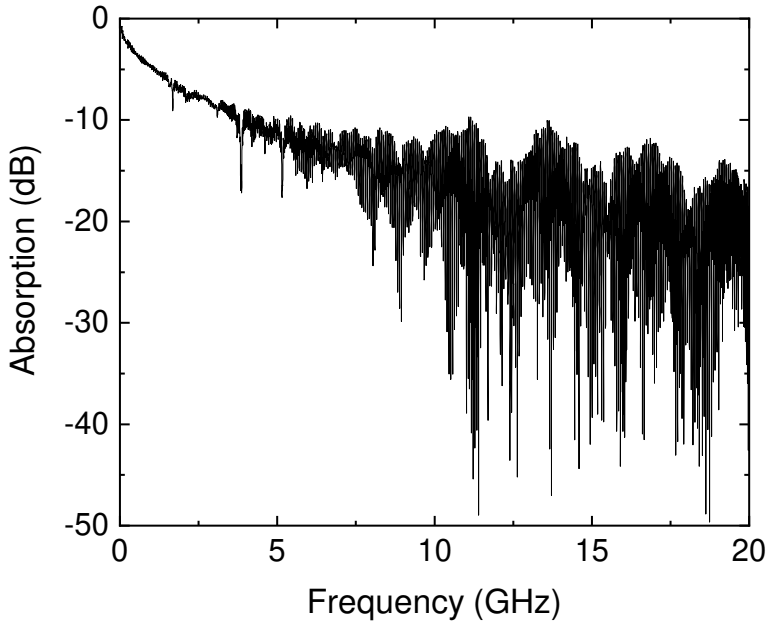

Fig. 4.6. Absorption spectrum for Kronos with the probe at 1.4 K. The damping of the signal for frequencies $\nu > 10$ GHz is of the order of ~ -20 dB. Since the output power of the signal generator is around 20 dB m over a wide spectrum, a signal with a power of circa 0 dB m $= 1$ mW is emitted from the antenna. Signals of up to 40 GHz have been observed to produce an ESR response, although the recording of the absorption spectrum is limited to 20 GHz due to the available equipment.

representative example is shown in Fig. 4.6. An estimate of the magnetic field reaching the sample can be calculated as [46]

$$B_{sample} = \sqrt{\frac{\mu_0 P}{2\pi c_0 d^2}}, \tag{4.1}$$

where μ_0 is the vacuum permeability, $P \approx 1$ mW the output power of the antenna, c_0 the speed of light, and $d \approx 5$ mm the distance between the antenna and the sample. The result is a local magnetic field of $B_{sample} = 163$ nT, and

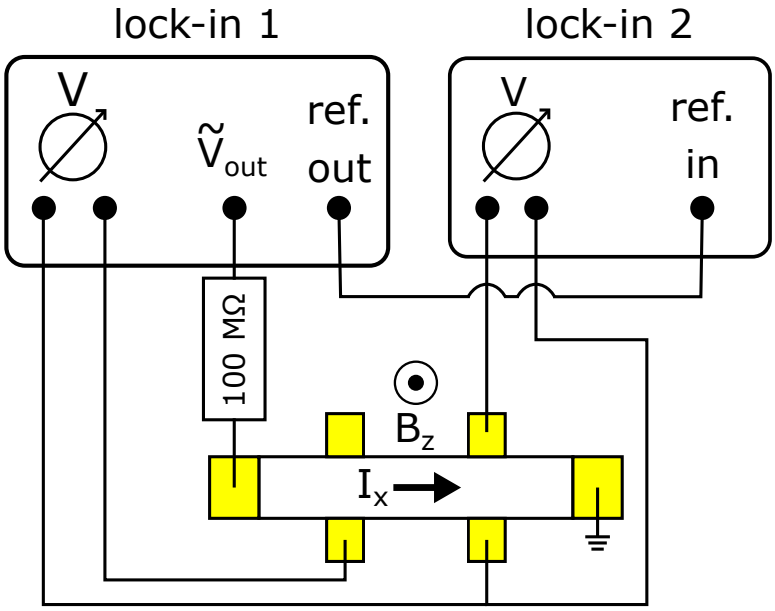

Fig. 4.7. Dual lock-in configuration. Lock-in 1 provides the AC voltage and transmits its frequency to lock-in 2 as a reference. Both lock-ins measure the voltage between the indicated contacts simultaneously.

hence it only plays a perturbative role compared to the fields that are produced by the superconducting magnets.

4.5 Magentoresistance and Lock-In Amplifiers

Each setup is equipped with two lock-in amplifiers of the type "Stanford Research Systems SR830 DSP Lock-In Amplifier". The working principle is detailed in the provided manual [104]. In essence, very small alternating current signals in the nV range can be detected despite potentially low signal-to-noise ratios.

Magnetoresistance is measured in a dual lock-in configuration, as depicted in Fig. 4.7. The resistance of the presented graphene samples is of the order of several 10 kΩ. Thus, when placed in series with a 100 MΩ resistor, the alternating current (AC) output voltage of $V_{RMS} = 0.1$ V and $f = 37$ Hz applied by lock-in 1 results in a nearly constant current of $I_x = 1$ nA through the sample. A reference signal is transmitted to lock-in 2, so that longitudinal and transverse resistances of the Hall bar can be measured simultaneously.

4.6 Source Measure Units

Each setup is equipped with a "Keithley 2400 Source Measure Unit" which serves multiple purposes. One is the measurement of the contact resistances of a sample before and after cool-down. It is found to be of the order of 1 kΩ µm [46], which is reasonable considering the sample fabrication where no emphasis was put into optimizing contact resistance [105].

The other purpose of the source measure units is the application of a back-gate voltage to a sample (see Section 2.2.4) while preventing it from a potential current flow in case of an undesired gate leakage. In this manner, the charge carrier density in the graphene can be controlled with minimal risk of damaging the sample.

The voltage that can be applied ranges from 100 nV to 200 V, and at the same time, a current between 10 fA and 10 A can be measured.

5 The ISOC Gap in Graphene

ESR measurements have been performed on samples 1 and 2 which mainly differ in terms of substrate geometry and the dimensions of the Graphene Hall bar. The results are analyzed and a model is presented which allows for the determination of the size of the ISOC gap in graphene. As a further implication of this analysis, graphene is found to undergo a phase transition from a spin-Hall insulator to a Dirac semi-metal at a critical magnetic field value.

Furthermore, the influence of an electric field on the SOC gap is studied. Not only does an electric field control the charge carrier type and density, but it introduces Rashba SOC to the system, which could potentially influence the size of the gap depending on its coupling strength (see Section 2.1.5).

5.1 Experimental Results

As described in Section 2.4, in a standard RD-ESR measurement, a constant current is applied to the sample and the antenna frequency is set to a fixed value, while the magnetic field is swept and the longitudinal voltage of the sample is recorded. This measurement can be repeated at various charge carrier densities by applying an appropriate voltage to a back-gate. The experimental setup for both samples, with the orientation of the antenna, the current flow, and the magnetic field, is depicted in Fig. 5.1. Due to the large attenuation of the coaxial wire and the antenna for frequencies exceeding 40 GHz and due to the expected g-factor of around 2 [18, 20], measurements are limited to range of $|B| \leq 2\,\mathrm{T}$ (see Eq. 2.41). The response of the longitudinal resistivity under resonance is generally very weak and not discernible from heating effects. In order to resolve the resonance signal, a background measurement is performed with the microwave signal switched off, which is subsequently subtracted from the individual ESR measurements.

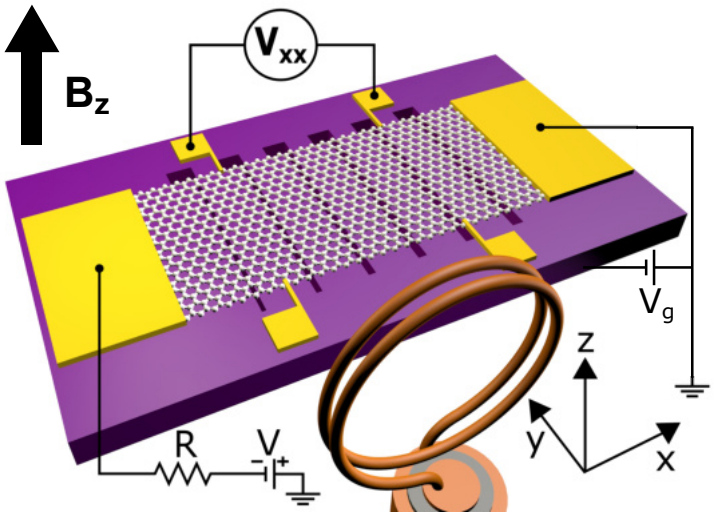

Fig. 5.1. Experimental setup of the ESR measurements. The external magnetic field is oriented in z-direction, i.e., perpendicular to the sample plane, while the AC antenna field points along the y-axis. A constant current is applied in x-direction and the longitudinal voltage V_{xx} is measured. The charge carrier density can be controlled via the back-gate voltage V_g. The trenches in the substrate are a schematic and correspond to sample 1.

5.1.1 Sample 1

Sample 1 is a $200 \times 22\,\mu m^2$ graphene sheet in a Hall bar configuration which is placed on a corrugated Si/SiO_2 substrate with a modulation period and amplitude of 200 nm and 20 nm, respectively (see Section 3.4). This substrate geometry results in a one-dimensional potential along the x-direction of the sample. It is measured in the Hermes setup at a temperature of 4.2 K. A current of $I_x = 0.8\,nA$ is applied and the back-gate voltage V_g is swept from -10 to 10 V in increments of 10 mV, while recording the longitudinal resistivity ρ_{xx}. The CNP is found to be at $V_{CNP} \approx -1.5\,V$, as indicated in Fig. 5.2.

The back-gate is then set to $V_g = 0$, or $\Delta V_{CNP} = V_g - V_{CNP} = 1.5\,V$, and the background measurement without microwave irradiation is performed by sweeping the magnetic field from -2 to 2 T in increments of 10 mT and recording ρ_{xx}.

From this background measurement and the previous gate sweep, it is possible to extract the charge carrier density $n(V_g = 0) \approx 2.6 \cdot 10^{11}\,cm^{-2}$ and the mobility $\mu \approx 1160\,cmV^{-1}s^{-1}$ of the sample, using Eq. 2.21 and Eq. 2.28. Note that these values are only estimates, since close to the CNP, $n(V_g)$ does

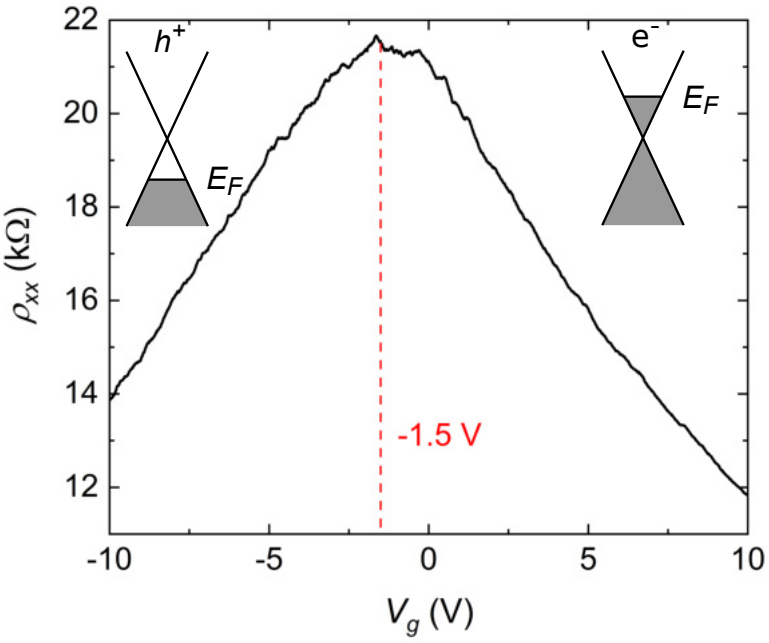

Fig. 5.2. Longitudinal resistivity versus back-gate voltage at $B = 0$ and $T = 4.2\,\mathrm{K}$, with the CNP at $V_{CNP} \approx -1.5\,\mathrm{V}$ indicated by the red line. The cartoons illustrate the regions dominated by hole (h^+) and electron (e^-) transport, respectively.

not behave linearly as it is assumed for Eq. 2.21. A correction would result in a lower charge carrier density and higher mobility, which would be more consistent with the results of T. Lyon *et al.* (2017) [20], i.e., $n \approx 1.5 \cdot 10^{11}\,\mathrm{cm}^{-2}$ and $\mu \approx 3700\,\mathrm{cmV}^{-1}\mathrm{s}^{-1}$, where the same batch of graphene and fabrication methods were used.

For the frequency-dependent measurements, the radiation power and frequency of the microwave signal are set to 17 dBm and 0.5 GHz, respectively, and magnetoresistance is measured. After each magnetic field sweep, the frequency is raised by 0.5 GHz up to the maximum value of 40 GHz. The radiation power of 17 dBm has been determined as the maximal output power over this frequency range. Despite the ambient temperature of 4.2 K, the antenna radiation heats the sample locally. It is estimated to reach an effective temperature of the order of several tens of Kelvin. This value is obtained by employing a simplified "radiation heat transfer" model given by

$$P = A\epsilon\sigma T^4/S, \tag{5.1}$$

where P is the radiation power, $A = 4\pi r^2$ is the surface area of the radiant

heat source, with r being its radius, ϵ is the emissivity coefficient, T is the temperature, and S is the irradiated surface area. In this simplified model, the radiation source is assumed to originate from the point at the center of the antenna in a spherical and homogeneous manner. The intensity at a certain distance r is then $P/A(r)$. P is assumed to be of the order of 1 mW, $r \approx 5\,\mathrm{mm}$ is the distance between the antenna and the sample (see Section 4.4), and the emissivity for Cu is around 0.05. Additionally, the effective surface area of the graphene sheet has to be considered, which is its area perpendicular to the radiation source. Here, the assumption of the point emitter has to be repealed. When assuming an antenna diameter of 4 mm the average angle between the top half of the antenna and the graphene sheet is approximately 10°, and one obtains $S = 200\,\mu\mathrm{m} \cdot 22\,\mu\mathrm{m} \cdot \tan(10°) \approx 800\,\mu\mathrm{m}^2$. When solving for the temperature, the result is $T \approx 20\,\mathrm{K}$. This seems to be an acceptable estimate when comparing it to the experimental results by Mani *et al.* (2012) [18], who determined a value of 13 K for the same power via temperature dependent measurements.

The data for the background and an ESR measurement at 17 GHz are shown in Fig. 5.3. In both measurements, the parabolic behavior in the range of $0.4\,\mathrm{T} \lesssim |B| \lesssim 0.8\,\mathrm{T}$ is an indicator for two-carrier transport [61]. For magnetic fields exceeding the upper limit, standard linear behavior of magnetoresistance without quantization is observed. The peak at zero field is evidence of weak localization, as described in Section 2.3.3.

The frequency data exhibit a lower resistivity over the whole magnetic field range than the background measurement due to the antenna radiation effectively heating the sample and hence, additional charge carriers being thermally activated for transport. This behavior has been observed in previous studies, and in general, a higher radiation power results in a lower sample resistivity [18, 20].

A noticeable feature is observed near $B = 0.5\,\mathrm{T}$, where the magnetoresistance under microwave irradiation shows a very weak peak which is not present in the background measurement. In order to investigate this feature, the difference between both measurements

$$\Delta\rho_{xx,\nu}(B) = \rho_{xx,\mathrm{background}}(B) - \rho_{xx,\nu}(B) \tag{5.2}$$

is calculated. $\Delta\rho_{xx,\nu}(B)$ is presented in Fig. 5.4 for various frequencies ν. The data for each individual measurement are normalized in order to compensate

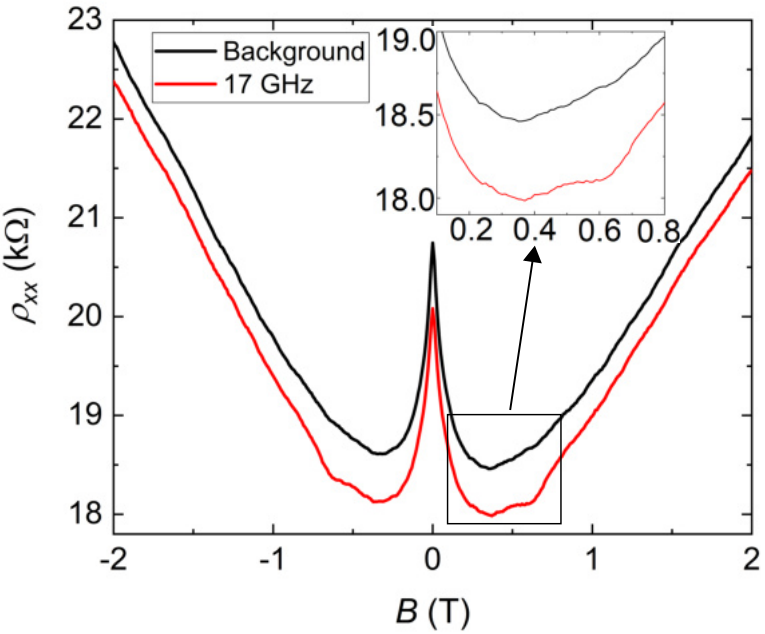

Fig. 5.3. Raw magnetoresistance data of the background (black) and an ESR measurement at 17 GHz (red), with the zoomed-in region highlighting the feature near 0.5 T. The measurements are taken at $T = 4.2\,\mathrm{K}$ and $V_g = 0$, with a microwave radiation power of 17 dBm for the 17 GHz line.

for the power absorption of the coaxial line and antenna, which is dependent on the frequency (see Section 4.4). The center peak is caused by the aforementioned WL in the sample, and since it is sensitive to temperature, it remains in the subtracted data. The remaining peaks are caused by ESR and are symmetric in B, due to $+B$ and $-B$ resulting in the same energy splitting ΔE_Z.

The derivative $\mathrm{d}[\Delta\rho_{xx,\nu}(B)]/\mathrm{d}B$ is calculated to resolve the resonance peaks more clearly, and the result for the entire frequency range is shown in Fig. 5.5. It is apparent that below a cut-off frequency of $\nu \approx 11\,\mathrm{GHz}$, the ESR signal vanishes, while it can be observed for the whole range above the cut-off.

In order to determine the exact resonance positions under the magnetic field, a Lorentzian fit (the line shape is caused by exchange interactions between localized and conduction electrons [68]) is performed on the ESR peaks for each individual measurement, and subsequently, the frequency is plotted against the peak position. As the shift for both peaks is clearly linear, a linear regression is performed and the result is shown in Fig. 5.6.

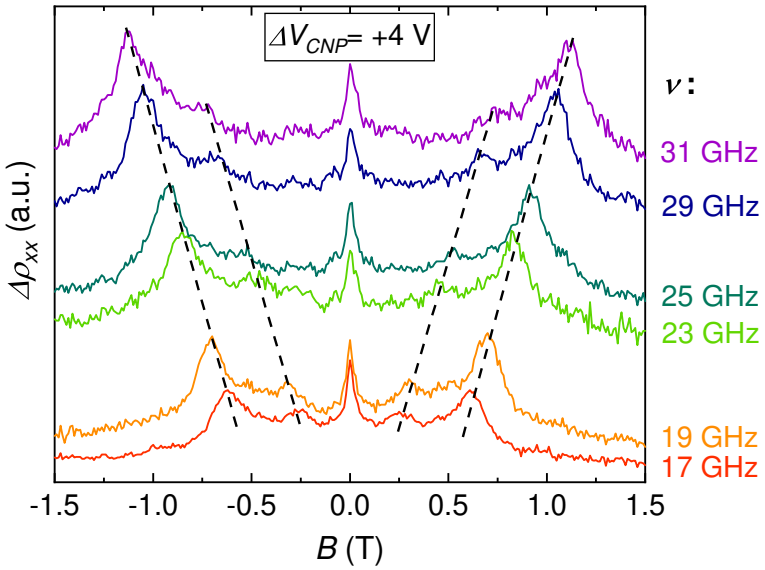

Fig. 5.4. $\Delta\rho_{xx,\nu}(B)$ for various frequencies. Two ESR peaks, which are symmetric in B, shift linearly with the applied microwave frequency (indicated by the dashed lines), while the peak at zero field stems from the the weak localization in the sample. The measurements are normalized and offset for clarity. The data are recorded at $T = 4.2\,\mathrm{K}$ and $V_g = 0$, with a microwave radiation power of 17 dBm.

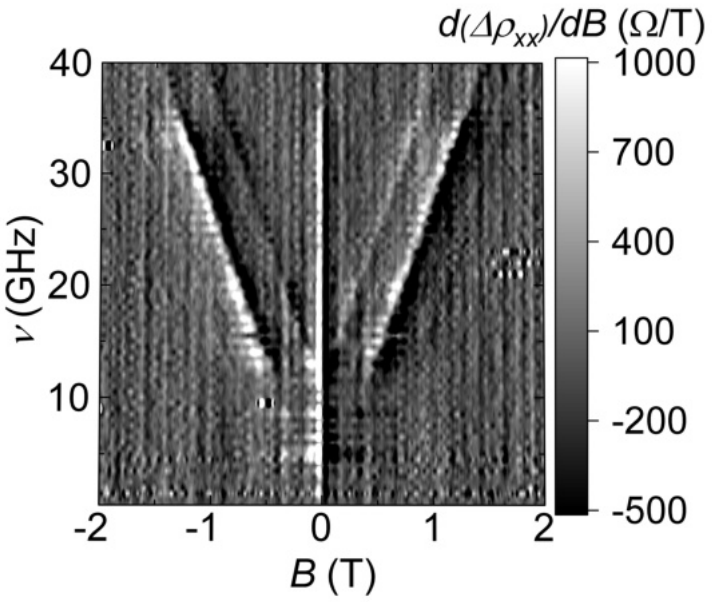

Fig. 5.5. Derivative of the ESR measurements recorded for $0.5\,\mathrm{GHz} \leq \nu \leq 40\,\mathrm{GHz}$. The resonance signals vanish abruptly for frequencies $\nu \lesssim 11\,\mathrm{GHz}$. The data are recorded at $T = 4.2\,\mathrm{K}$ and $V_g = 0$, with a microwave radiation power of 17 dBm.

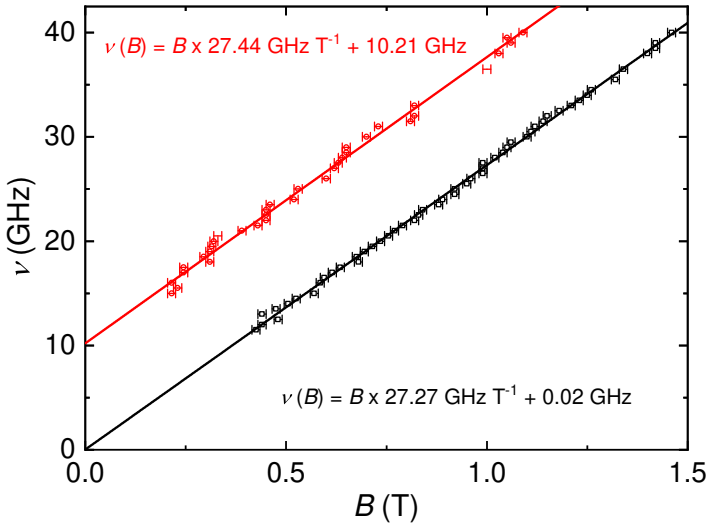

Fig. 5.6. Antenna frequency versus ESR peak position in magnetic field for the data from Fig. 5.5. The red circles correspond to the peak positions of the upper "V" feature of Fig. 5.5, while the black squares stem from the lower "V". A linear regression yields an intercept of the red line with the frequency axis of 10.21 GHz, which corresponds to an energy of 42.2 µeV. The extrapolation of the black data points passes through the origin, with only a small offset, as expected from traditional Zeeman splitting. The slopes of both graphs yield similar g-factors of $g \approx 1.95$.

The errors of the peak positions are estimated to be around $\pm 10\,\mathrm{mT}$, originating from the inaccuracy of the magnet power supply (3 mT), the error of the resonance peak fit (3 mT) and a potential tilt angle of the sample of up to 5° with respect to the magnetic field (4 mT).

The slopes of the two graphs are $[\mathrm{d}\nu/\mathrm{d}B]_{\mathrm{upper}} = (27.44 \pm 0.39)\,\mathrm{GHzT}^{-1}$ and $[\mathrm{d}\nu/\mathrm{d}B]_{\mathrm{lower}} = (27.27 \pm 0.16)\,\mathrm{GHzT}^{-1}$ for the upper and lower peak, respectively. These values correspond to g-factors of $g_{\mathrm{upper}} = 1.96 \pm 0.03$ and $g_{\mathrm{lower}} = 1.95 \pm 0.01$ (see Eq. 2.44), which are in good agreement with previous studies [18, 20, 21, 46].

From the slope and the ESR peak width ΔB, the spin lifetime of the charge carriers can be calculated (see Eq. 2.49). The average width for all frequencies is $\Delta B \approx 40\,\mathrm{mT}$, which corresponds to a lifetime of $\tau_s \approx 73\,\mathrm{ps}$. Note that the peak width (and position), and therefore the spin lifetime, is constant over the accessible range of radiation power, i.e., temperatures of $10\,\mathrm{K} \lesssim T \lesssim 40\,\mathrm{K}$ according to Eq. 5.1 in combination with the data of Lyon *et al.* (2017) [20, 46].

The lower line intercepts the frequency axis at $\nu_0 = (0.02 \pm 0.16)\,\mathrm{GHz}$, i.e., nearly at the origin of the graph, as it would be expected from traditional Zeeman splitting. However, the upper line extrapolates to $\nu_1 = (10.21 \pm 0.24)\,\mathrm{GHz}$,

which corresponds to an energy of $E_1 = h\nu_1 = (42.2 \pm 1.0)\,\mu\text{eV}$.

The appearance of the additional ESR peak is unexpected and the finite intercept of this second peak with the frequency axis suggests that an energy gap exists in the band structure of graphene. It is the central topic of this chapter to investigate the nature of this gap.

In order to rule out the one-dimensional potential as the cause, which is present in sample 1 due to the corrugated substrate, the ESR measurements have also been performed on sample 2. Here, the Hall bar is much larger than in sample 2, and the substrate is flat SiO_2 on Si (see Section 3.4).

5.1.2 Sample 2

Sample 2 is a $1920 \times 66\,\mu\text{m}^2$ graphene sheet in a Hall bar configuration which is situated on a flat Si/SiO_2 substrate. It is measured in the Prometheus system with the temperature set to $\sim 1.4\,\text{K}$. Note that there are always minor temperature fluctuations over long times in such a system ($\sim 0.1\,\text{K}$), which however, do not seem to influence the results of the measurements. This is most likely due to the negligible size of the fluctuations when compared to the radiation heating of approximately 20 K.

The back-gate voltage is swept from $-10\,\text{V}$ to $10\,\text{V}$ in increments of $10\,\text{mV}$. From the obtained data, which are presented in Fig. 5.7, it is not possible to extract the position of the CNP. The positive slope of the curve indicates that the Fermi energy lies below the Dirac point in the measured voltage range. The voltage is limited to $|V_g| = 10\,\text{V}$ to protect the graphene from a potentially harmful gate leakage current.

The magnetic field range is limited to $-1\,\text{T} \leq B \leq 1\,\text{T}$ and the step size is 5 mT. Additionally, the frequency range is $1\,\text{GHz} \leq \nu \leq 30\,\text{GHz}$, with increments of 1 GHz. The power is set to 21 dBm, which has been determined as the maximal output power over this frequency range. The magnetoresistance data for the background and an ESR measurement at $\nu = 18\,\text{GHz}$ are presented in Fig. 5.8.

Identically to Section 5.1.1, $\Delta\rho_{xx,\nu}(B)$ is calculated and the results for four individual frequencies are shown in Fig. 5.9. The normalized curves for the entire frequency range are displayed in Fig. 5.10.

Although the signal-to-noise ratio is significantly worse compared to sample 1, two resonance peaks appear which are symmetric in B and shift linearly with frequency.

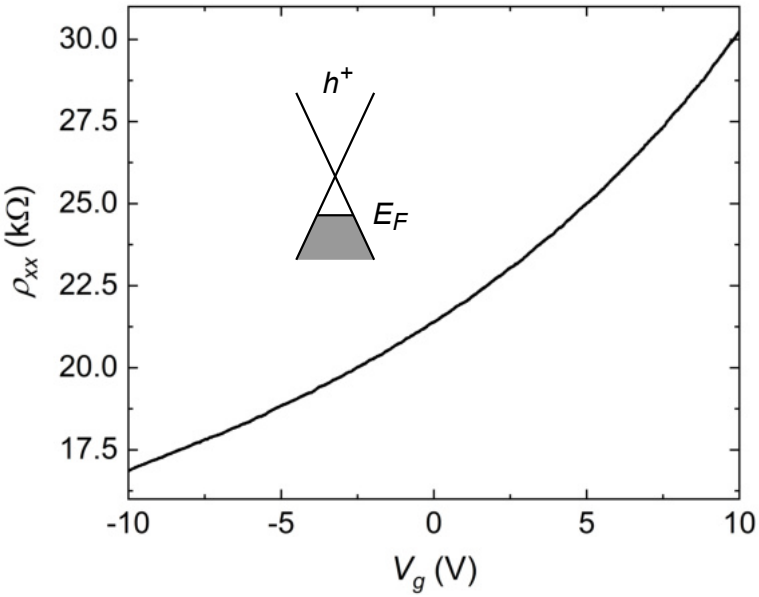

Fig. 5.7. Longitudinal resistivity versus back-gate voltage at $B = 0$ and $T = 1.4\,\mathrm{K}$, with $V_{CNP} > 10\,\mathrm{V}$. The cartoon indicates the Fermi level in this regime.

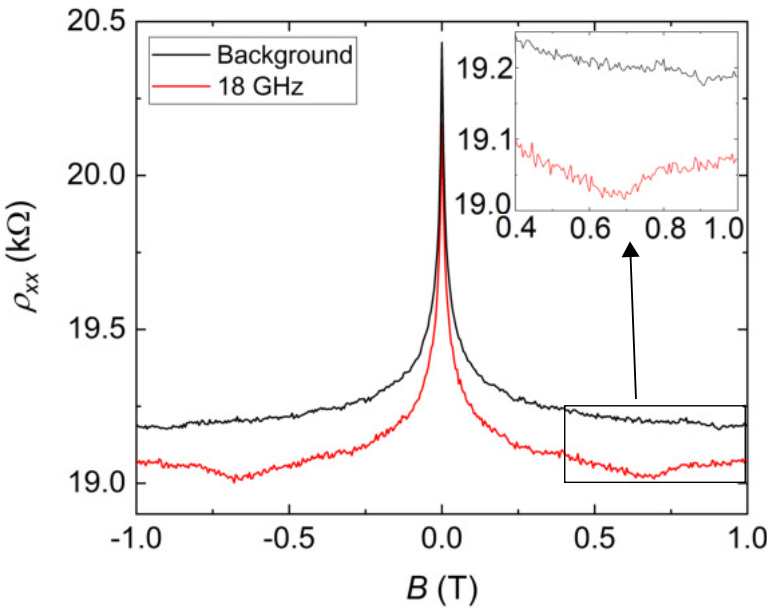

Fig. 5.8. Raw magnetoresistance data of the background (black) and an ESR measurement at 18 GHz (red), with the zoomed-in region highlighting the additional features of the red curve. The data are recorded at $T = 1.4\,\mathrm{K}$, $V_g = 0$, with a microwave radiation power of 21 dBm for the 18 GHz line.

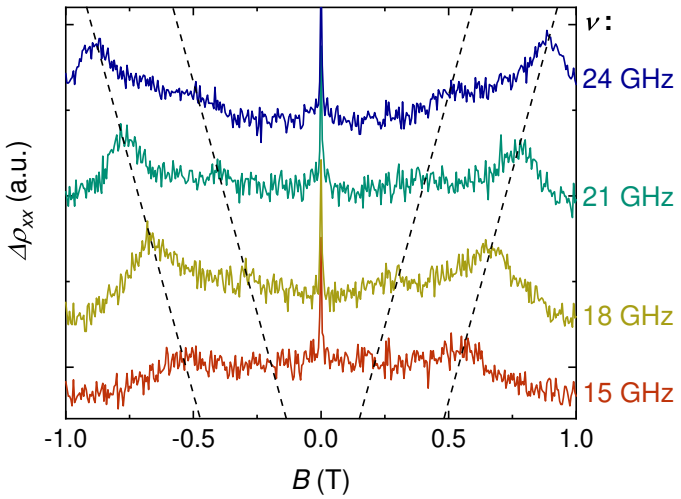

Fig. 5.9. $\Delta\rho_{xx,\nu}(B)$ for various frequencies. Two ESR peaks, which are symmetric in B, shift linearly with the applied microwave frequency (indicated by the dashed lines), while the peak at zero field stems from the the weak localization in the sample. The inner resonance signal is hardly visible in this presentation of the data (improved visibility in the normalized contour plot in Fig. 5.10) and therefore, the corresponding dashed lines serve as a guide to the eye. The measurements are normalized and offset for clarity. The data are recorded at $T = 1.4\,\mathrm{K}$, $V_g = 0$, with a microwave radiation power of 21 dBm.

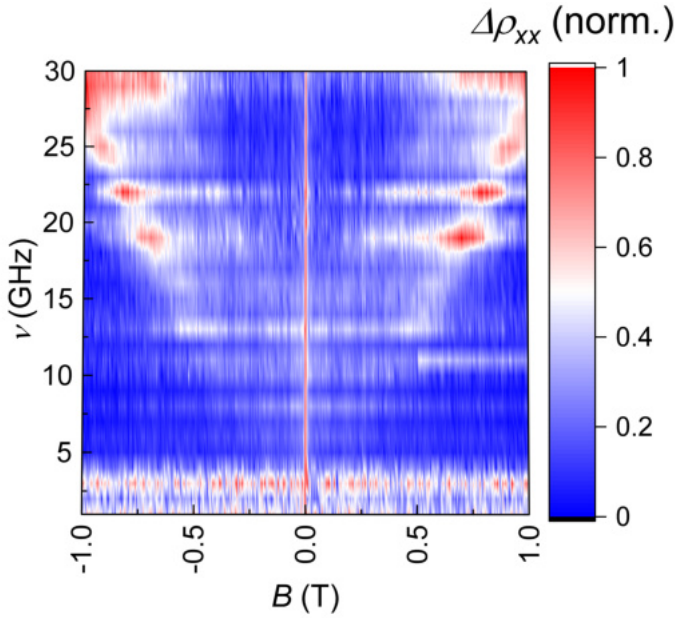

Fig. 5.10. Normalized ESR measurements recorded for $1\,\mathrm{GHz} \leq \nu \leq 30\,\mathrm{GHz}$. The resonance signal is present over a wider range of frequencies. The data are taken at $T = 1.4\,\mathrm{K}$, $V_g = 0$, with a microwave radiation power of 21 dBm.

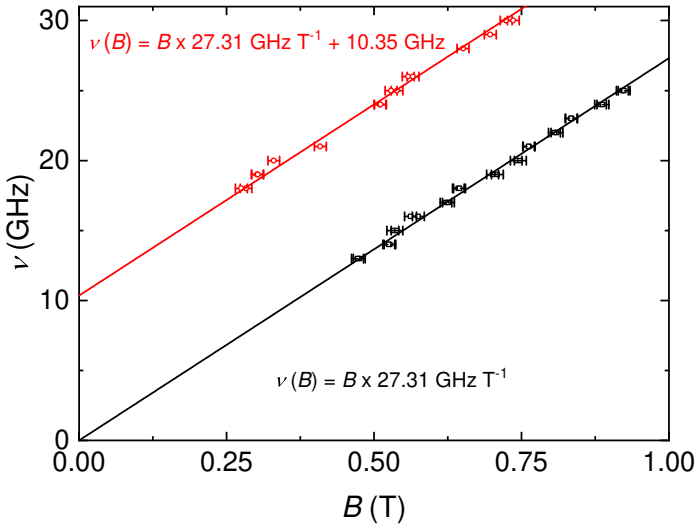

Fig. 5.11. Antenna frequency versus ESR peak position in magnetic field. The red circles correspond to the peak positions of the upper "V" feature of Fig. 5.10, while the black squares stem from the lower "V". A linear fit to the black squares, which is guided through the origin, yields a g-factor of $g_{\mathrm{corr}} = 1.95 \pm 0.01$. When the g-factor for both resonances is assumed to be equal, the intercept of the red graph with the frequency axis corresponds to an energy gap of $E_{\mathrm{corr}} = 42.6\,\mu\mathrm{eV}$. The values for the free fits are stated in the main text.

Strong unintentional surface doping (see Fig. 5.7) and local defects are the most likely causes for the poor signal-to-noise found in sample 2. It is also possible that temperature fluctuations couple differently to the sample due to the He gas flow of the VTI system which may vary under microwave irradiation.

Lorentz fits are performed and the frequency is plotted against peak position in Fig. 5.11.

Here, the error bars of $\pm 10\,\mathrm{mT}$ include once more the inaccuracy of the magnet power supply, the error from the resonance peak fit and the potential tilt angle of the sample of up to 5° with respect to magnetic field. The average resonance peak width of $\Delta B \approx 40\,\mathrm{mT}$ is comparable with sample 1, returning a spin relaxation time of $\tau_s \approx 73\,\mathrm{ps}$.

When performing the linear regression for the black squares in Fig. 5.11, i.e. the lower "V" feature in Fig. 5.10, without boundary conditions, the intercept with the frequency axis is found at $\nu_0 = (0.46 \pm 0.28)\,\mathrm{GHz}$. The y-axis intercept of the upper "V" feature (red circles) is at $\nu_1 = (10.89 \pm 0.26)\,\mathrm{GHz}$. This corresponds to an energy difference of $\Delta E = h(\nu_1 - \nu_0) = (43.0 \pm 2.2)\,\mu\mathrm{eV}$, which is consistent with the result for sample 1. The slope of the upper reso-

nance is $[\mathrm{d}\nu/\mathrm{d}B]_{\mathrm{upper}} = (26.22 \pm 0.50)\,\mathrm{GHzT}^{-1}$ and for the lower resonance feature $[\mathrm{d}\nu/\mathrm{d}B]_{\mathrm{lower}} = (26.68 \pm 0.40)\,\mathrm{GHzT}^{-1}$. These results yield g-factors of $g_{\mathrm{upper}} = 1.87 \pm 0.04$ and $g_{\mathrm{lower}} = 1.91 \pm 0.03$, respectively. They differ significantly from those calculated for sample 1, and also from the ones found in literature [18, 20, 21, 46].

With the boundary condition that the Zeeman splitting should be zero at B = 0 T, the fit for the black squares in Fig. 5.11 runs through the origin, and the slope becomes $[\mathrm{d}\nu/\mathrm{d}B]_{\mathrm{new}} = (27.31 \pm 0.08)\,\mathrm{GHzT}^{-1}$, which corresponds to a corrected g-factor of $g_{\mathrm{corr}} = 1.95 \pm 0.01$. Additionally, by setting the slope of the regression for the red circles to the new value, the y-axis intercept is then $\nu_{\mathrm{corr}} = (10.35 \pm 0.09)\,\mathrm{GHz}$ and the resulting energy gap is now $E_{\mathrm{corr}} = h\nu_{\mathrm{new}} = (42.6 \pm 0.1)\,\mu\mathrm{eV}$. Hence, although the g-factor is corrected, the energy gap stays nearly constant, and all results are in good agreement with previous studies as well as those of sample 1.

5.1.3 Back-Gate Dependence

After receiving similar results for samples 1 and 2 with the back-gate voltage set to zero, ESR is probed in dependence of the back-gate voltage to test the strength of the Rashba spin-orbit interaction, which would be reflected in the size of the energy gap (see Section 2.1.5). In addition to introducing Rashba SOC to the system, the gate voltage also controls the position of the Fermi energy and the charge carrier density in graphene. The results of sample 1 and 2, which, up until now, were measured in the electron- and hole-like regime of the band structure, respectively, are in good agreement with the data by Lyon *et al.* (2017) [20], who showed that the g-factor in graphene is independent of the charge carrier density.

Since Rashba SOC should only depend on the applied gate voltage relative to zero, it is desirable to measure both positive and negative voltages. The available data for sample 1 are presented, before a more systematic approach is taken with sample 2, where the back-gate voltage range is extended and the step size reduced.

For sample 1, ESR measurements are performed in Hermes at $T = 4.2\,\mathrm{K}$, $\nu = 19\,\mathrm{GHz}$, and a power of 17 dBm (see Section 5.1.1) for five different gate voltages $-10\,\mathrm{V} \lesssim \Delta V_g \lesssim 10\,\mathrm{V}$, or, relative to the CNP, $-8.5\,\mathrm{V} \lesssim \Delta V_{CNP} \lesssim 11.5\,\mathrm{V}$. The corresponding charge carrier densities are in the range of $-7.6 \cdot 10^{11}\,\mathrm{cm}^{-2} \lesssim n \lesssim 9.7 \cdot 10^{11}\,\mathrm{cm}^{-2}$. $\Delta\rho_{xx,19GHz}(B)$ is displayed in Fig. 5.12, with the nominal

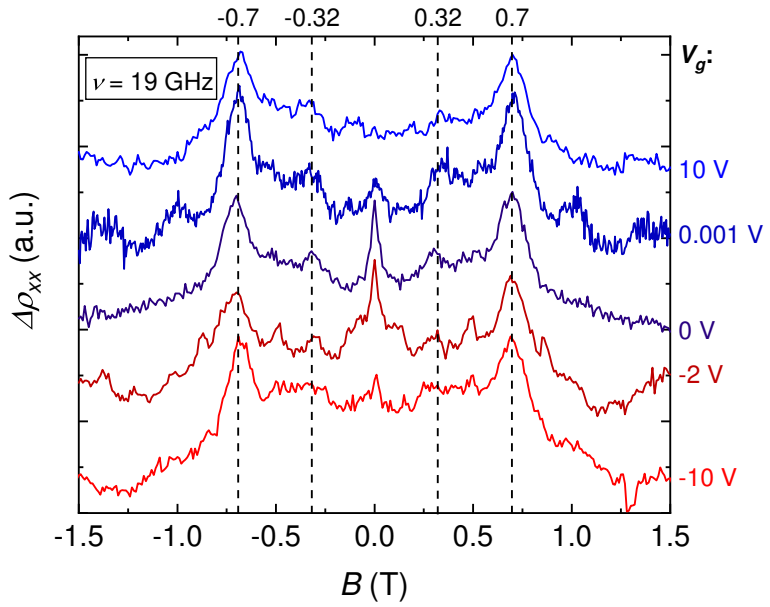

Fig. 5.12. ESR measurements in sample 1 for five different back-gate voltages. The dashed lines indicate the ESR peak positions calculated for $g = 1.95$ and an energy gap of 42 µeV. Red (blue) color represents the Fermi energy being in the hole-(electron-)like regime. Both resonance positions are insensitive to the applied voltage. The CNP is at $V_{CNP} = -1.5\,\mathrm{V}$. The individual curves are normalized and offset for clarity. The data are recorded at $T = 4.2\,\mathrm{K}$, with a microwave radiation power of 17 dBm.

values of the resonance peaks indicated by the dashed lines, assuming $g = 1.95$. The invariance of the peak at $|B_0| = 0.7\,\mathrm{T}$ supports the g-factor independence claimed by Lyon *et al.* (2017) [20], while the constant position of the resonance at $|B_1| = 0.32\,\mathrm{T}$ indicates a fixed energy gap.

More data are available for sample 2, measured by T. Anlauf. For these measurements, the sample was transferred to the Kronos system, where the back-gate voltage can be set to values of up to $|V_g| = 100\,\mathrm{V}$. The temperature is held constant at 1.4 K, with minor fluctuations over time as mentioned in the previous section. A gate sweep determines the CNP to be at $V_{CNP} = 47.0\,\mathrm{V}$ and the result is shown in Fig. 5.13. Note that the position of the CNP here is not necessarily comparable to the measurement performed in the Prometheus system as the CNP can vary over multiple cool-downs of the sample due to unintentional and varying surface doping.

Due to the appearance of the CNP at high gate voltage, only positive voltages can be applied in order to probe the influence of Rashba SOC on the energy gap.

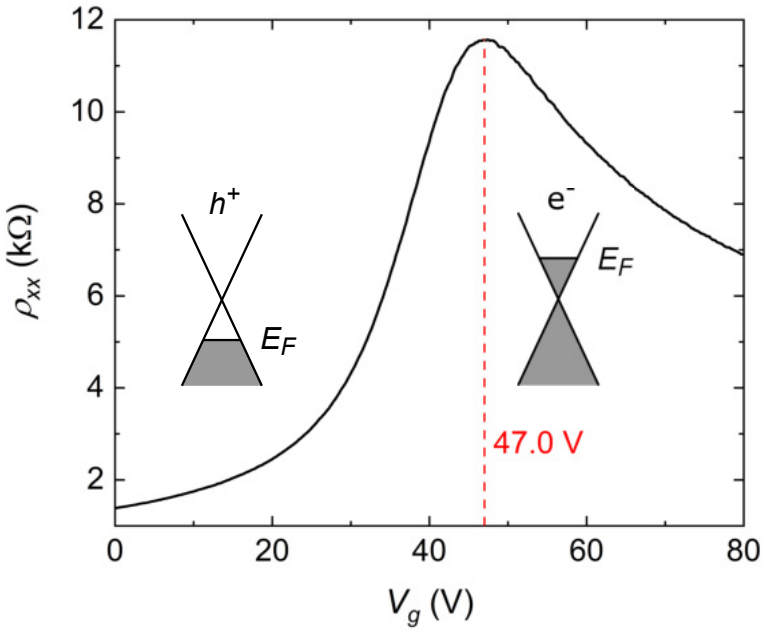

Fig. 5.13. Longitudinal resistivity ρ_{xx} versus back-gate voltage at $B = 0$ and $T = 1.4\,\mathrm{K}$, with $V_{CNP} = 47.0\,\mathrm{V}$. The cartoons indicate the regions dominated by hole (h^+) and electron (e^-) transport, respectively.

ESR measurements are performed at a constant frequency of 22 GHz and a power of 21 dBm, while the back-gate voltage is systematically tuned in the range of $7\,\mathrm{V} \leq \Delta V_g \leq 91\,\mathrm{V}$ in steps of 1 V. The magnetic field is swept from 0 to 1 T in steps of 10 mT. The results for selected gate voltages are displayed in Fig. 5.14.

For $21\,\mathrm{V} \lesssim V_g \lesssim 85\,\mathrm{V}$, or, relative to the CNP, $-26\,\mathrm{V} \leq \Delta V_{CNP} \leq 38\,\mathrm{V}$ both peaks are visible and their positions are insensitive to changes of the gate voltage. The corresponding charge carrier densities are $-2.01 \cdot 10^{12}\,\mathrm{cm}^{-2} \leq n \leq 2.87 \cdot 10^{12}\,\mathrm{cm}^{-2}$. Beyond this range, the resonance at 0.83 T stays at a constant position, while the peak at 0.43 T vanishes in the background. Despite not being able to verify the invariance of the gap for negative gate voltages in sample 2, the results of both samples combined suggest that the energy gap in graphene does not depend on the back-gate voltage, and therefore Rashba SOC effects are negligible in the studied range.

In a subsequent analysis, the resonance peak height $\Delta\rho_{peak}$ is plotted with respect to the applied gate voltage (see Fig. 5.15). The height of the resonance peaks increases when the Fermi energy moves towards the CNP.

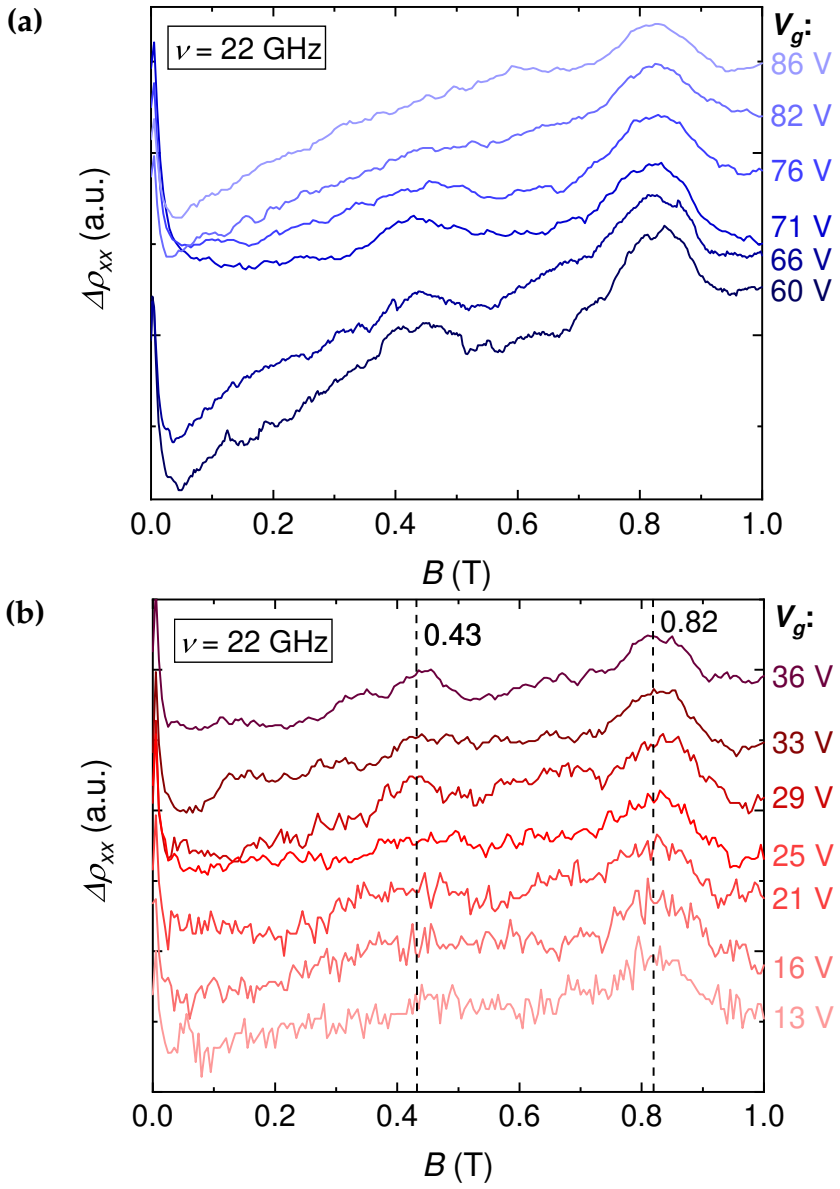

Fig. 5.14. ESR measurements for various gate voltages. The color indicates the position of the Fermi energy with respect to the Dirac point, with blue (red) indicating $E_F > 0$ ($E_F < 0$). **(a)** The resonance peak positions are insensitive to gate voltage. However, the height of both peaks diminishes with increasing distance from the CNP (represented by lighter shades of blue), until the resonance at 0.43 T vanishes at around 85 V. **(b)** Similar behavior is observed as in (a), with the vanishing lower-field resonance at approximately 21 V. The data are recorded at $T = 1.4$ K, with a microwave radiation power of 21 dBm.

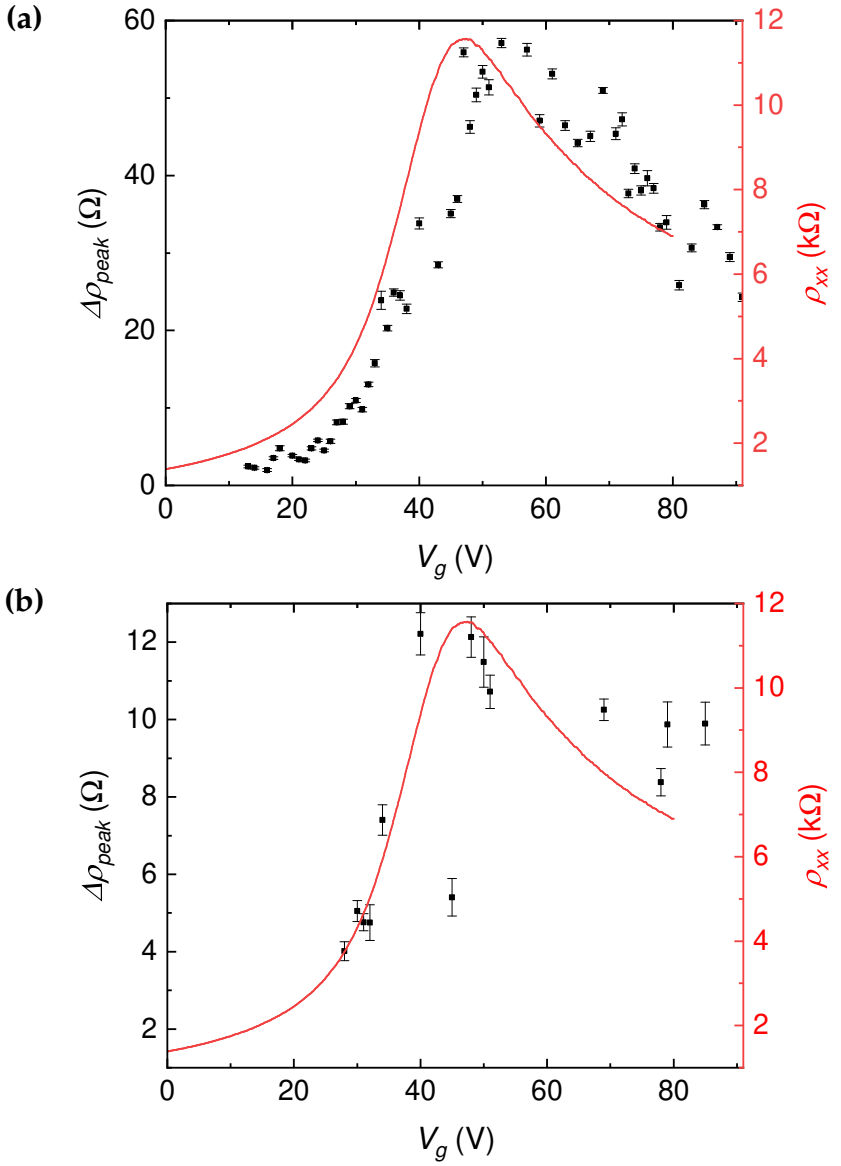

Fig. 5.15. Peak height versus back-gate voltage in comparison with the longitudinal resistivity $\rho_{xx}(0,V_g)$. **(a)** Analysis of the resonance at 0.83 T. The peak height (black data points) follows the behavior of the longitudinal sample resistivity (red solid line), however, there seems to be a slight horizontal mismatch between the two datasets. **(b)** Analysis of the resonance at 0.43 T. Two outliers have been eliminated. Compared to (a), the number of data points is reduced, since the peak fit does not converge for the missing voltages. The peak height follows the sample resistivity. The corresponding data have been recorded at $T = 1.4\,\mathrm{K}$ and $\nu = 22\,\mathrm{GHz}$, with a radiation power of 21 dBm.

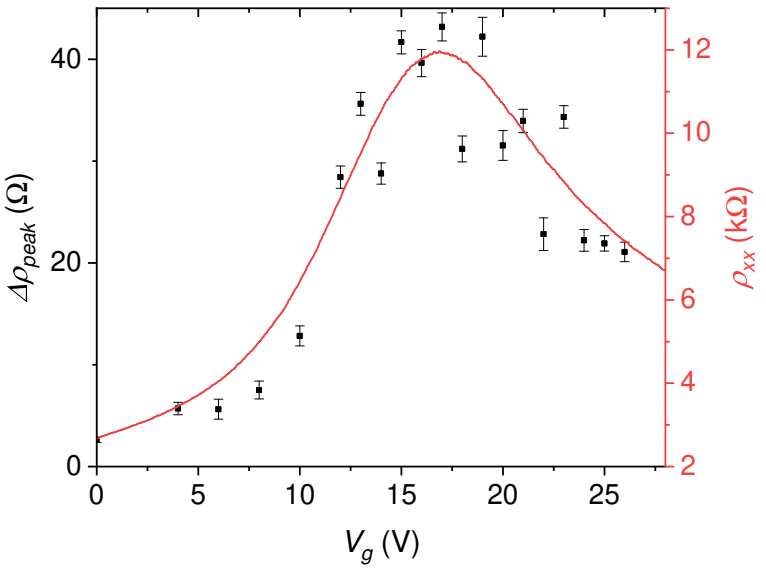

Fig. 5.16. Peak height and sample resistivity in dependence of back-gate voltage. The data are recorded from a different sample cool-down than Fig. 5.15, with the CNP at $V_{CNP} = 16.5\,\mathrm{V}$. The corresponding data have been recorded at $T = 1.4\,\mathrm{K}$ and $\nu = 22\,\mathrm{GHz}$, with a radiation power of 21 dBm.

Thus, it reproduces the trend of the sample resistivity versus back-gate voltage from Fig. 5.13. The number of data points is low for the 0.43 T resonance since an analytical identification of the peak is not possible for all values of V_g.

In Fig. 5.15a, there is a horizontal offset between the two datasets. This is unexpected, since in a simple picture, $\Delta\rho_{peak} \propto (n_\uparrow - n_\downarrow)^{-1}$ and $\rho_{xx}(V_g) \propto (n_\uparrow + n_\downarrow)^{-1}$, with $n_\uparrow$ ($n_\downarrow$) representing carrier densities of the spin up (down) state. The result is then $\Delta\rho_{peak}(V_g)/\rho_{xx}(V_g) \approx$ constant.

Indeed, in a second set of data, which has been previously recorded during another cool-down cycle of the sample, the horizontal mismatch is not observed (see Fig. 5.16). A major difference here is the position of the CNP which is found at $V_{CNP} = 16.5\,\mathrm{V}$. Therefore, one can speculate that the reason for the mismatch at a higher CNP might be charged impurities on the graphene, influencing the availability of charge carriers that contribute to the resonance signal. However, further studies need to be carried out to determine the origin of this shift with certainty.

5.2 Theoretical Interpretation

As shown in section Section 5.1.3, the electron spin properties of graphene seem to be invariant within the accessible parameters of temperature, sample size, carrier type and density (through the application of a gate voltage) or the topology of the SiO_2 substrate. The large scale (hundreds of µm) CVD graphene used in this work contains hundreds of individual domains with various orientations, which limits the mobility and enhances (intervalley) scattering [106]. Yet, the observed energy gap and g-factor are comparable to those determined by Mani et al. (2012) [18], measured by ESR on epitaxially grown graphene (several μm^2 in size) on a SiC substrate, where graphene quality and substrate interaction should be very different.

All these experimental facts demonstrate that the observed properties are particularly robust against external influences and imply that they are most likely intrinsic to graphene. In the following paragraphs, a model, which was developed by M. Prada, is presented to complement these observations.

The theory that is discussed in Section 2.1 serves as a starting point, and Fig. 5.17 is displayed as a reminder. Intrinsic SOC leads to the existence of an energy gap Δ_I in the bulk, which is denoted in black. The flat edge bands, shown in green and magenta, possess a fixed chirality and high DOS that cross the gap at the Γ point at zero magnetic field. Here, the occupation of the edge bands is maximal (indicated by color brightness), and spreads over the bandwidth $h\Delta\nu \sim \Delta_I$. Fig. 5.17a shows the band structure for edge E1 (An equivalent consideration can be made for edge E2, where the magenta (green) band corresponds to spin up (down)). Fig. 5.17b is a cartoon depicting the resulting SHI state. Rashba SOC is neglected for the moment.

When a moderate magnetic field ($g\mu_B B < \Delta_I$, or $B < 0.38\,\mathrm{T}$) is applied, the bands of opposite spin move in opposite directions along the energy axis. This causes the band crossing of E1 to be shifted to negative values of $\mathbf{k}$, while still keeping the edge character intact. The observation of an ESR signal in the edge bands is prevented due to the aforementioned bandwidth $h\Delta\nu$, and excitations occur over a range of $\mathbf{k}$-vectors as indicated by the red arrows in Fig. 5.18a. In contrast, a bulk signal that fulfills the condition $h\nu = g\mu_B B + \Delta_I$ is always observable, as it is indeed the case (upper "V" feature, Fig. 5.5). In this regime, graphene is in the SHI state.

When the magnetic field is increased, the band crossing occurs in the bulk and the edges are energetically separated allowing for an observable resonance

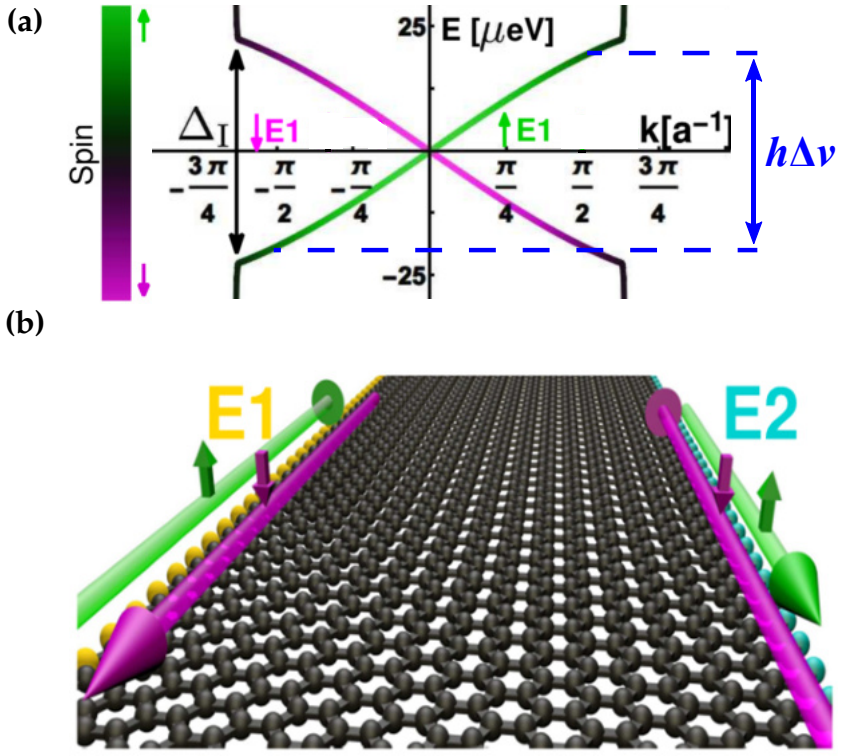

Fig. 5.17. (a) Band structure for the bulk and edge E1. Green and magenta denote spin up and down, respectively, while black indicates eigenstates with bulk character. The bulk band gap Δ_I is assumed to be caused by ISOC. The edge band broadening $\Delta\nu$ is indicated in blue. Figure adopted from Sichau *et al.* (2019) [21]. **(b)** Schematic illustration of the edge modes. Charge carrier transport is spin-dependent, thus depicting graphene in the SHI phase.

signal of $h\nu = g\mu_B B$ in addition to the bulk resonance (see Fig. 5.18b). This edge signal, however, is broadened due to the bandwidth $h\Delta\nu$. A cartoon illustrating the energy levels and the corresponding ESR transitions in a simplified manner is shown in Fig. 5.19. Due to the band crossings occurring in the bulk (at **K**, and **K**′ when including E2) at these higher magnetic fields, graphene is in the semi-metallic state.

Fig. 2.6, which shows the bulk bands at one of the **K** points, suggests that the size of the gap varies with the Rashba field, which seems to contradict the results of the back-gate dependent measurements with a constant gap shown in Section 5.1. However, since a photon carries spin but no sublattice spin, the selection rule dictates that only transitions between bands of the same color can be induced.

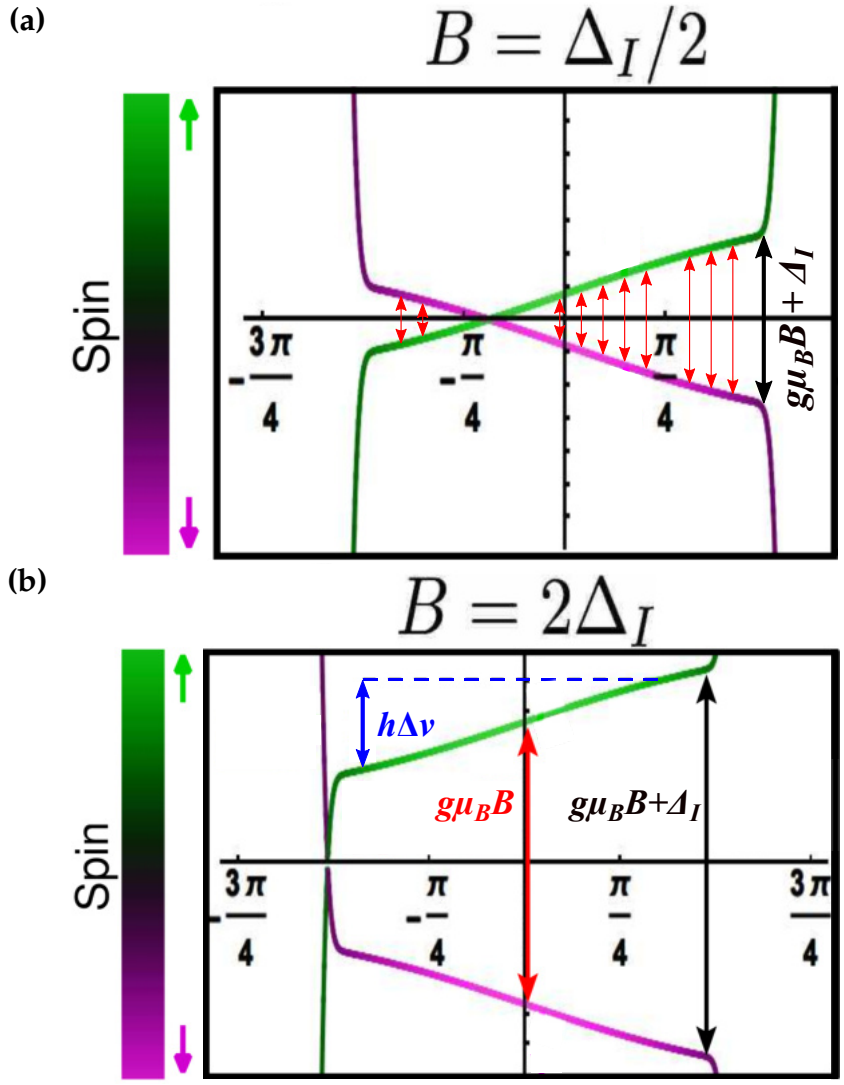

Fig. 5.18. **(a)** Band structure for a moderate magnetic field. Transitions between the edge bands are possible in the entire indicated range (red double-headed arrows), resulting in an undetectable resonance signal. The bulk resonance is always observed and follows the condition $h\nu = g\mu_B B + \Delta_I$. Graphene is in the SHI state. **(b)** Band structure for a magnetic field which surpasses the size of the energy gap Δ_I. The edge signal is now visible and it is broadened by $h\Delta\nu = \Delta_I$. Graphene is in the semi-metallic state. Figure adopted from Sichau *et al.* (2019) [21].

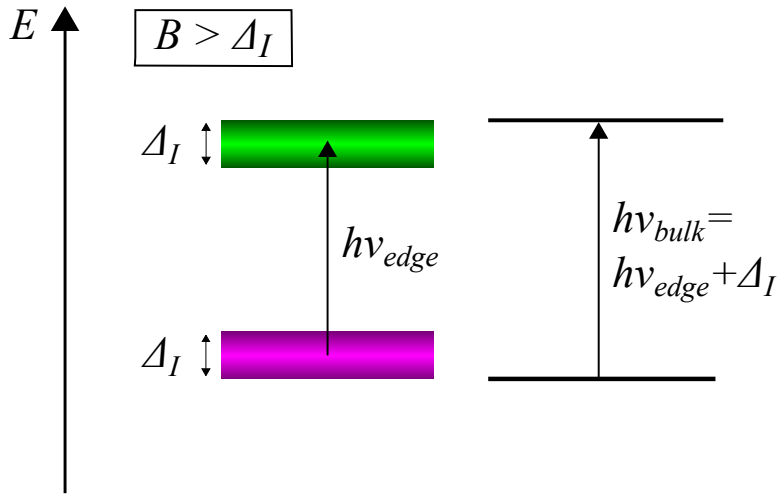

Fig. 5.19. Cartoon indicating the ESR transitions for large magnetic fields: The edge signal has a resonant condition given by the Zeeman splitting, $h\nu_{edge} = g\mu_B B$, with a spread given by the energetic dispersion, $\Delta_I = h\Delta\nu$, whereas the bulk fulfills $h\nu_{bulk} = h\nu_{edge} + \Delta_I$. The color gradient indicates the LDOS, with bright (dark) colors representing a high (low) occupation.

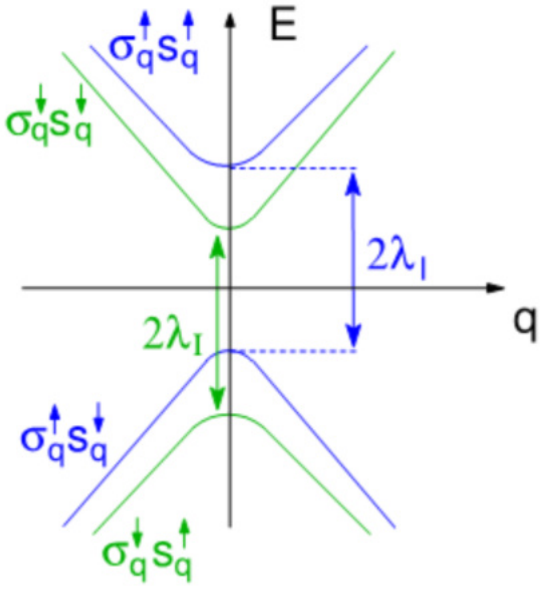

Fig. 5.20. Schematic representation of the band structure in the vicinity of the **K** point, with ISOC and Rashba SOC dictating the position of the bands. As long as $\lambda_I > \lambda_r$, the gap between bands with identical sublattice spin is always $\Delta_I = 2\lambda_I$. The vector **q** represents the momentum with respect to **K**. Figure adopted from Sichau *et al.* (2019) [21], Supplemental Material.

The Rashba Hamiltonian (see Eq. 2.18), carries opposite sign for valence and conduction bands, which results in a constant gap between bands with the same sublattice spin. Hence, ESR does not allow to probe the gap $2\lambda_I - 2\lambda_r$, but only the pure intrinsic SOC; this is illustrated in Fig. 5.20.

As long as the contribution from the ISOC, λ_I, is larger than the Rashba SOC, λ_r, ($\lambda_I > \lambda_r$) the model is consistent with the experimental results, since the edge bands cross diagonally (as described above), making the SHI observable at low magnetic fields [11]. For the case of $\lambda_I < \lambda_r$, graphene is transformed into a trivial insulator with the edge bands connecting the bulk bands horizontally and the graphene becomes gapped. The consequence of the latter is an observable ESR signal in the entire frequency range, including $\nu < 11\,\mathrm{GHz}$, as there is no SHI state anymore. This seems to be the case in sample 2 (Fig. 5.9), most likely owed to the charged impurities on the surface, which is reflected in the large distance to the CNP. Note that the strength of the Rashba coupling λ_r is different for every sample and cool-down cycle.

Finally, addressing the involved energy scales is crucial to the model. The ISOC gap of 42.2 µeV is smaller than the thermal energy of $k_B T \approx 360\,\mu\mathrm{eV}$ by an order of magnitude. However, this is no hindrance to resolving the gap, since the spin imbalance dictated by the Maxwell-Boltzmann distribution is still significant (see Section 2.4). In contrast, the thermal energy is pivotal, as it provides access to the gap even when the Fermi level is far away from the Dirac points.

6 Angle-Dependent RD-ESR

In this chapter, it will be shown that the g-factor measured in Chapter 5 is merely an effective g-factor for a specific external magnetic field orientation, in this case perpendicular to the sample plane. However, through the ISOC and Rashba mechanisms, additional effective magnetic fields are introduced to the graphene, altering the perceived g-factor for varying external magnetic field angles. In the following sections, the effective g-factor is determined for various directions of the external **B**-field in order to establish a model which allows for the description of the behavior of the g-factor as well as the extraction of characteristic atomic quantities of graphene.

ESR measurements have been performed on sample 2 in Prometheus, with the experimental setup and the variable magnetic field being shown in Fig. 6.1.

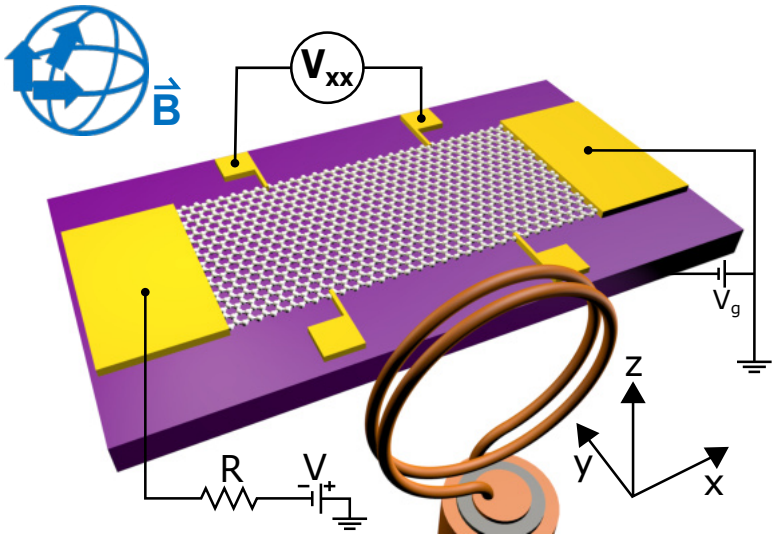

Fig. 6.1. Schematic setup of the ESR measurements for sample 2. The external magnetic field can be freely oriented in space with an absolute strength of $|B| \leq 1\,\mathrm{T}$, while the AC antenna field is pointing along the y-axis. A constant current is applied in x-direction and the longitudinal voltage V_{xx} is measured. The charge carrier density can be controlled via the back-gate voltage V_g.

6.1 Axial Magnetic Field Sweeps

In addition to the measurement of **B** along the z-direction presented in Chapter 5, the magnetic field is oriented along the x- and y-axes, respectively. Also, the three diagonals of the x-y, x-z, and y-z-planes are probed by ESR. For each direction i, the magnetic field is swept in the range of $-1\,\mathrm{T} \leq B_i \leq 1\,\mathrm{T}$ in increments of 5 mT, and the frequency is tuned between 1 and 30 GHz in steps of 1 GHz. A current of $I_x = 1\,\mathrm{nA}$ is applied and the back-gate is grounded. The base temperature of the system of $T \approx 1.4\,\mathrm{K}$ showed fluctuations of the order of 0.5 K and had a reduced cooling power due to problems with the Helium needle valve. Signatures of these variations can be observed as a field-dependent background in the magnetoresistance data, but do not influence the value of the g-factor.

6.1.1 Magnetic Field in x-Direction

The data analysis for ESR in x-direction is identical to that of the previous experiments along the z-axis. The differential resistivity $\Delta\rho_{xx,\nu}$ is calculated from the recorded magnetoresistance data, a Lorentzian fit is performed for each resonance peak, and the applied microwave frequency is plotted versus the resonance peak position. Finally, the g-factor is determined from the slope of these data points. Fig. 6.2 shows $\Delta\rho_{xx,\nu}$ for the entire frequency range, with each frequency curve normalized in order to emphasize the resonance feature. Only a single ESR peak line is visible in this measurement, although a faint difference in contrast indicates the existence of a second line. An analytical approach, however, could not reliably distinguish this second peak from the noise. The overall gradient in resistivity from left to right is an artifact arising from heating when the magnetic fields is swept to its starting position at $-1\,\mathrm{T}$ and a low cooling power due to the aforementioned issues with the needle valve of the cryostat.

When the fit is set through the origin (see Fig. 6.3), the main resonance has a slope of $(25.36 \pm 0.07)\,\mathrm{GHzT}^{-1}$ and the corresponding g-factor is $g_x = 1.81 \pm 0.01$. The errors originate from the same sources that have been discussed for the z-direction in Chapter 5.

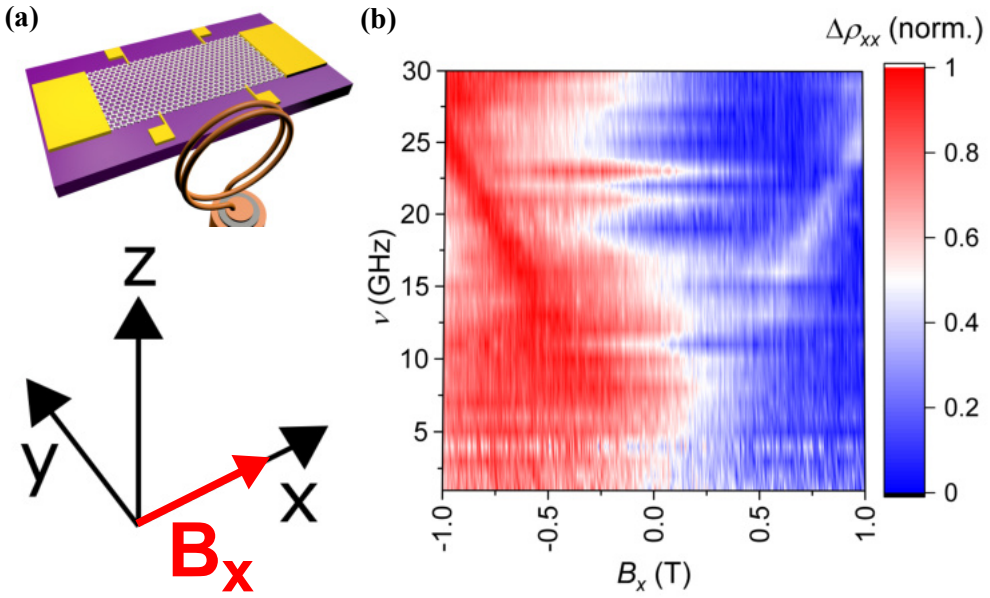

Fig. 6.2. **(a)** Schematic depiction of the magnetic field orientation in the sample. **(b)** Normalized ESR measurements with the magnetic field $\mathbf{B} = B_x\hat{e}_x$. The resonance in shape of a "V", which originates at $B_x = 0$, is present over a wide range of frequencies. The gradient in resistivity from left to right is a temperature-related artifact. The data are recorded at $T = 1.4\,\mathrm{K}$ and $V_g = 0$, with a radiation power of 21 dBm.

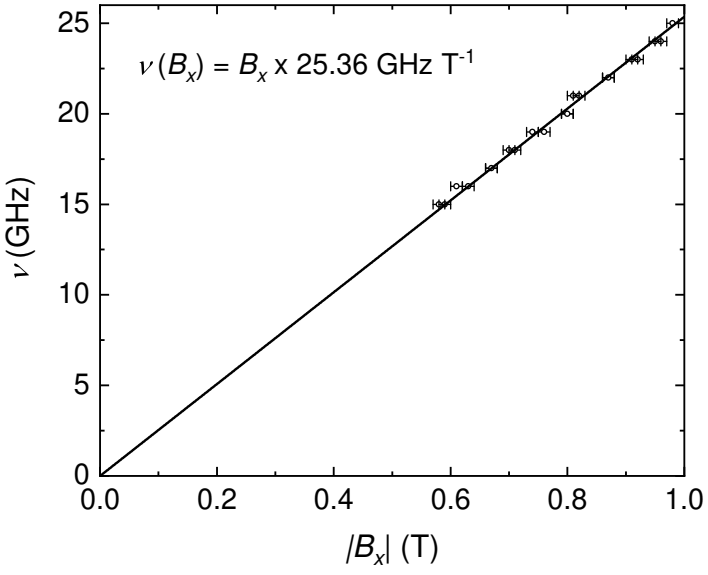

Fig. 6.3. Microwave frequency in dependence of the ESR peak position. The slope of the linear fit yields a g-factor of $g_x = 1.81 \pm 0.01$.

6.1.2 Magnetic Field in y-Direction

The normalized data from the ESR measurements with the magnetic field oriented along the y-direction is shown in Fig. 6.4. The fit in Fig. 6.5 yields a slope of $(28.46 \pm 0.10)\,\mathrm{GHzT}^{-1}$, which corresponds to a g-factor of $g_y = 2.03 \pm 0.01$ This is very close to the free electron g-factor of $g = 2.0023$. The large region of high resistivity at magnetic fields between $-0.5\,\mathrm{T}$ and 0 is a temperature-related artifact.

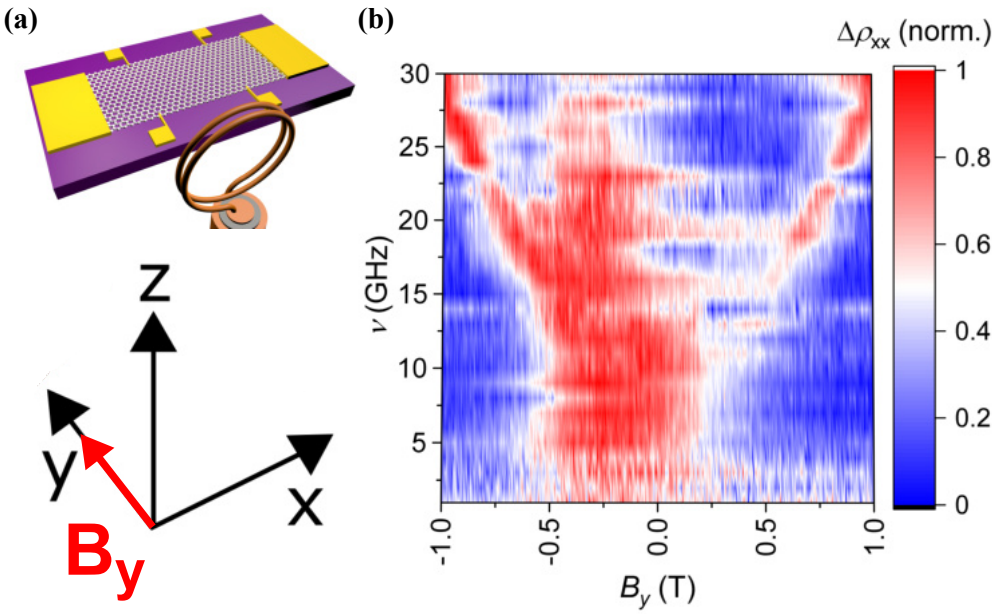

Fig. 6.4. **(a)** Schematic depiction of the magnetic field orientation in the sample. **(b)** Normalized ESR measurements with the magnetic field $\mathbf{B} = B_y\hat{e}_y$. The resonance in shape of a "V", which originates at $B_y = 0$, is present over a wide range of frequencies. The high resistivity in the range between $\sim -0.5\,\mathrm{T}$ and $\sim 0\,\mathrm{T}$ is a temperature-related artifact. The data are recorded at $T = 1.4\,\mathrm{K}$ and $V_g = 0$, with a radiation power of 21 dBm.

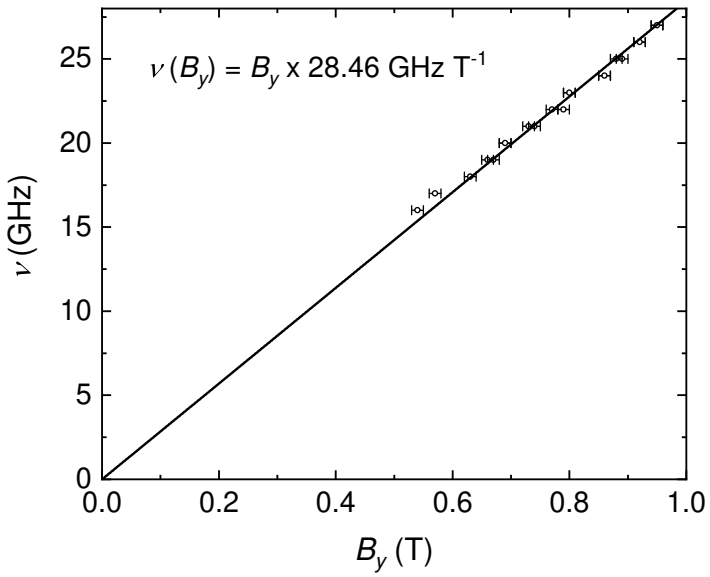

Fig. 6.5. Microwave frequency in dependence of the ESR peak position. The slope of the linear fit yields a g-factor of $g_y = 2.03 \pm 0.01$.

6.1.3 Magnetic Field in x-y-Direction

In order to achieve a more coherent understanding of the angular dependence of the g-factor for more than just the main axes of the coordinate system, the magnetic field directions at various angles are studied, starting with the diagonal of the x-y-plane, i.e., $\mathbf{B} = \mathbf{B_{x-y}} = B_x\hat{e}_x + B_y\hat{e}_y \equiv B_{x-y} \cdot (\hat{e}_x + \hat{e}_y)/\sqrt{2}$, with $\hat{e}_i$ being the unit vectors in i-direction, and with equal values of the magnetic fields, $B_x = B_y$.

The normalized data are plotted in Fig. 6.6 and the resonance peak positions are analyzed in Fig. 6.7. The correction of the linear fit is performed as before and the resulting slope is $(26.79 \pm 0.12)\,\mathrm{GHzT}^{-1}$, which corresponds to a g-factor of $g_{x-y} = 1.91 \pm 0.01$. This value lies in between $g_x = 1.81$ and $g_y = 2.03$. Various temperature artifacts are visible for negative magnetic fields as well as for the measurement at 15 GHz.

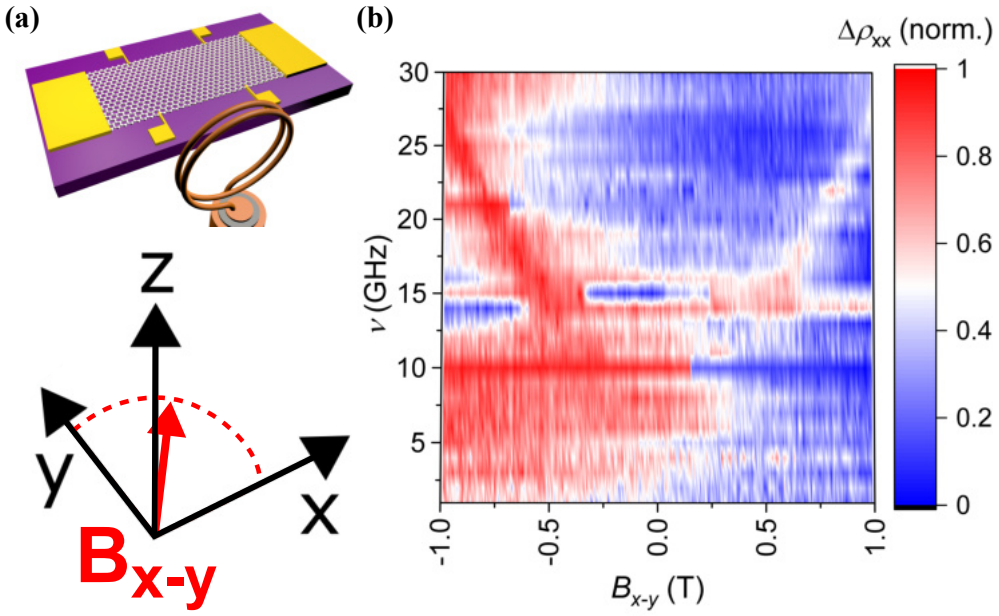

Fig. 6.6. **(a)** Schematic depiction of the magnetic field orientation in the sample. **(b)** Normalized ESR measurements with the magnetic field $\mathbf{B} = \mathbf{B_{x-y}}$. The resonance in shape of a "V", which originates at $B_{x-y} = 0$, is present over a wide range of frequencies. The gradient in resistivity from negative to positive fields is a temperature-related artifact. The data are recorded at $T = 1.4\,\mathrm{K}$ and $V_g = 0$, with a radiation power of 21 dBm.

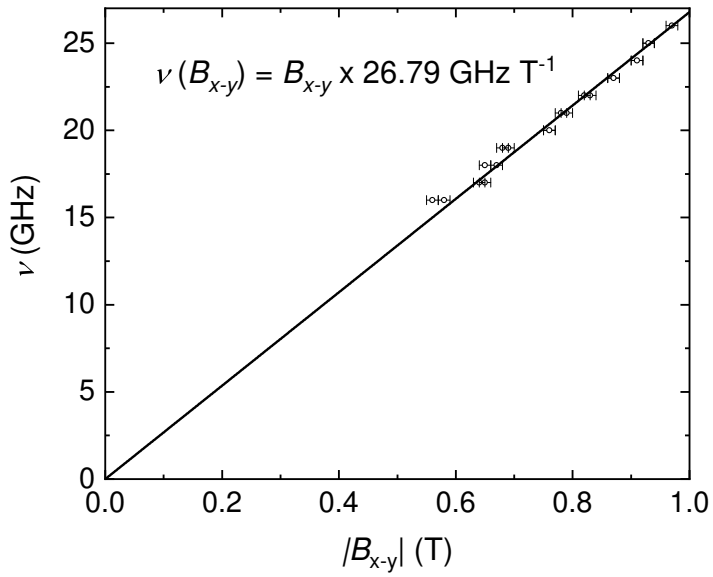

Fig. 6.7. Microwave frequency in dependence of the ESR peak position. The slope of the linear fit yields a g-factor of $g_{x-y} = 1.91 \pm 0.01$.

6.1.4 Magnetic Field in x-z-Direction

When ESR is measured with the external magnetic field along the direction of $\mathbf{B} = \mathbf{B_{x-z}} = B_{x-z} \cdot (\hat{e}_x + \hat{e}_z)/\sqrt{2}$, a different g-factor is obtained yet again. The experimental results are displayed in Fig. 6.8 and the analysis is presented in Fig. 6.9, yielding $g_{x-z} = 1.87 \pm 0.01$. This result supports the previous speculation of the g-factor value shifting with the applied magnetic field angle. The measurement at 20 GHz shows a step-like artifact from temperature fluctuations.

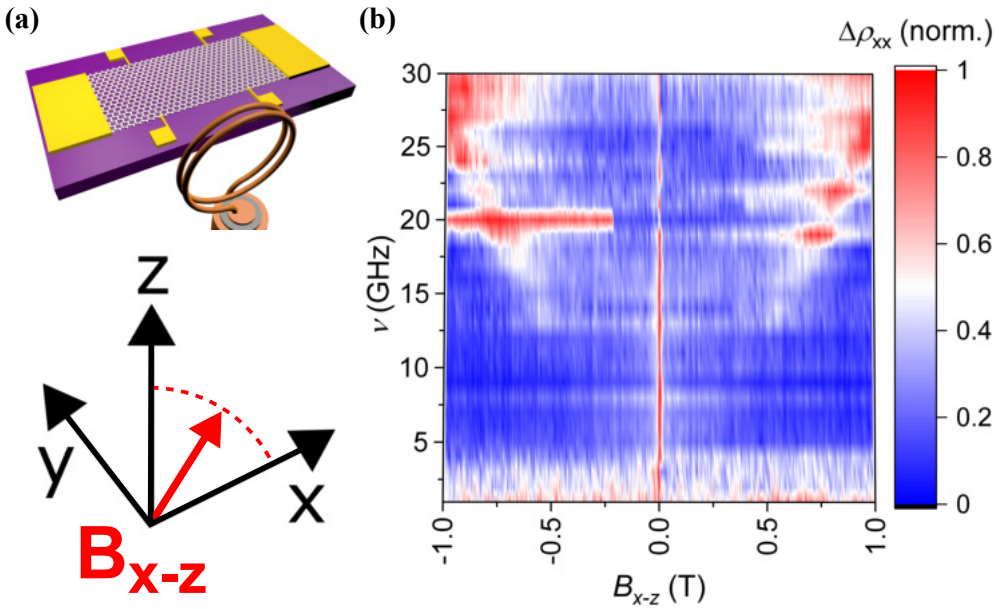

Fig. 6.8. **(a)** Schematic depiction of the magnetic field orientation in the sample. **(b)** Normalized ESR measurements with the magnetic field $\mathbf{B} = \mathbf{B_{x-z}}$. The resonance in shape of a "V", which originates at $B_{x-z} = 0$, is present over a wide range of frequencies. The data are recorded at $T = 1.4$ K and $V_g = 0$, with a radiation power of 21 dBm. The measurement at 20 GHz shows artifacts due to varying temperature.

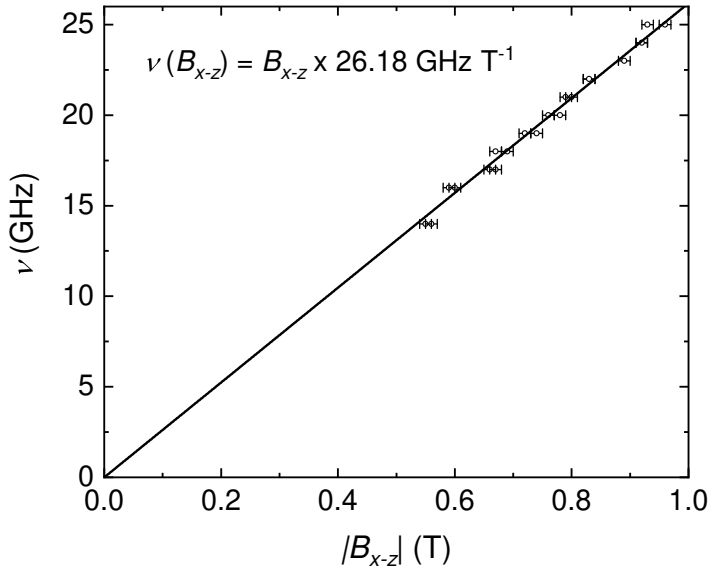

Fig. 6.9. Microwave frequency in dependence of the ESR peak position. The slope of the linear fit yields a g-factor of $g_{x-z} = 1.87 \pm 0.01$.

6.1.5 Magnetic Field in y-z-direction

The data in Fig. 6.10 show the results of the ESR experiments when the magnetic field is swept along $\mathbf{B} = \mathbf{B_{y-z}} = B_{y-z} \cdot (\hat{e}_y + \hat{e}_z)/\sqrt{2}$. The temperature is stable over the entire measurement apart from a small step-like artifact at 25 GHz. The analysis of the resonance peak position in Fig. 6.11 results in $g_{y-z} = 1.99 \pm 0.01$, with $g_z < g_{y-z} < g_y$.

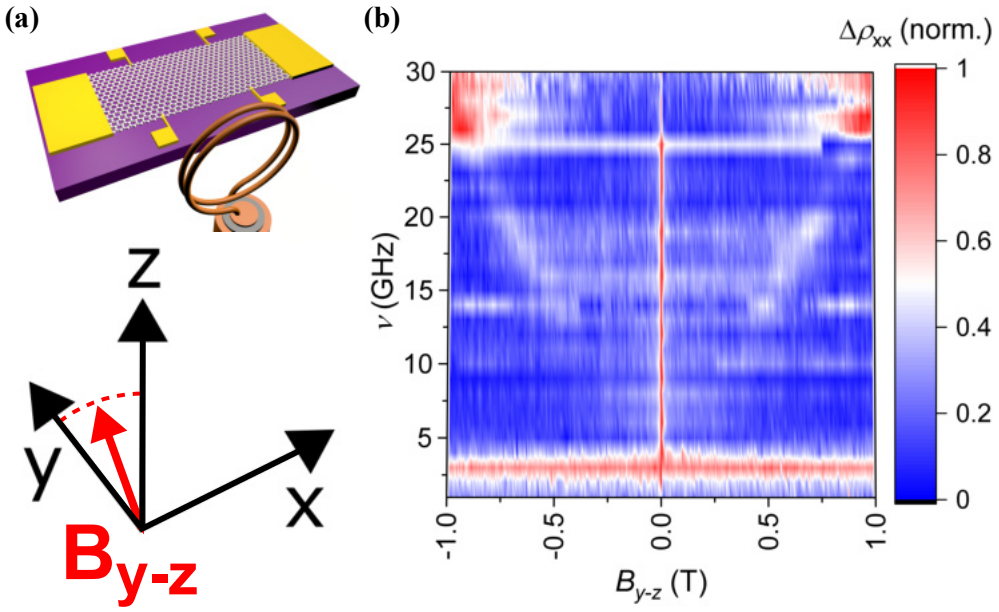

Fig. 6.10. **(a)** Schematic depiction of the magnetic field orientation in the sample. **(b)** Normalized ESR measurements with the magnetic field $\mathbf{B} = \mathbf{B_{y-z}}$. The resonance in shape of a "V", which originates at $B_{y-z} = 0$, is present over a wide range of frequencies. The data are recorded at $T = 1.4\,\mathrm{K}$ and $V_g = 0$, with a radiation power of 21 dBm

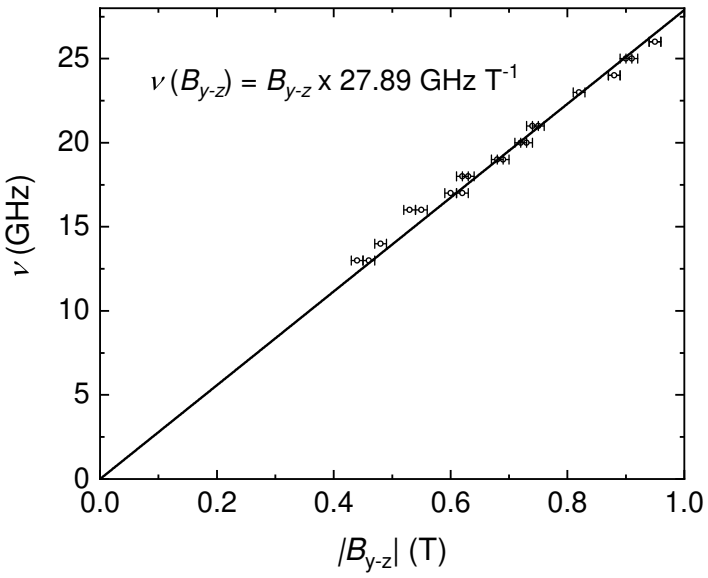

Fig. 6.11. Microwave frequency in dependence of the ESR peak position. The slope of the linear fit yields a g-factor of $g_{y-z} = 1.99 \pm 0.01$.

6.2 Radial Magnetic Field Sweeps

An overview of the determined g-factors for six directions of the magnetic field is given in Tab. 6.1. With the present approach, the g-factor can be measured with an error of less than 5 % for the main axes of the magnetic field. For arbitrary (diagonal) directions, however, this approach is very time-consuming, since the two magnetic field components have to be swept separately for each data point.

To reduce the measurement time, the g-factor can be deduced from the resonance of a constant microwave frequency under various angles of the magnetic field direction $\mathbf{B}$. This approach, however, is limited to a narrow window around $|\mathbf{B}|$ and works at the expense of accuracy of the determined g-factor. It is possible to measure the behavior of the g-factor over an entire coordinate plane with an angular resolution of 3° in a reasonable amount of time. A microwave frequency of $\nu_{res} = 19\,\mathrm{GHz}$ with a power of 21 dBm produces a clear resonance for all directions that have been probed. Corresponding to the g-factors listed in Tab. 6.1, a resonance can then be expected in the range of $0.66\,\mathrm{T} \lesssim |\mathbf{B}| \lesssim 0.75\,\mathrm{T}$. The magnetic field is therefore swept in a slightly bigger range of $0.6\,\mathrm{T} \leq |\mathbf{B}| \leq 0.8\,\mathrm{T}$, always in radial direction, with a step size of 5 mT. The temperature is $T = 1.4\,\mathrm{K}$ and the back-gate voltage is set to 0.

Tab. 6.1. g-factors for various directions of the external magnetic field $\mathbf{B}$. These values have been obtained for $T = 1.4\,\mathrm{K}$ and $V_g = 0$.

g_x	g_{x-y}	g_y	g_{y-z}	g_z	g_{x-z}	**Error**
1.81	1.91	2.03	1.99	1.95	1.87	0.01

6.2.1 Magnetic Field in the x-y-Plane

The ESR data in Fig. 6.12 show the normalized differential resistivity for the radial magnetic field sweeps in the x-y-plane, with the experimental parameters from Section 6.2. The magnetic field vector can be written as

$$\mathbf{B_{x-y}} = B_{x-y} \cdot \cos(\theta_{x-y}) \cdot (\hat{e}_x + \hat{e}_y)/\sqrt{2}, \tag{6.1}$$

where θ_{x-y} is the angle between $\mathbf{B_{x-y}}$ and the y-axis in the x-y-plane. Resonances, which have a large differential resistivity, appear in red whereas the off-resonance conditions are shown in blue.

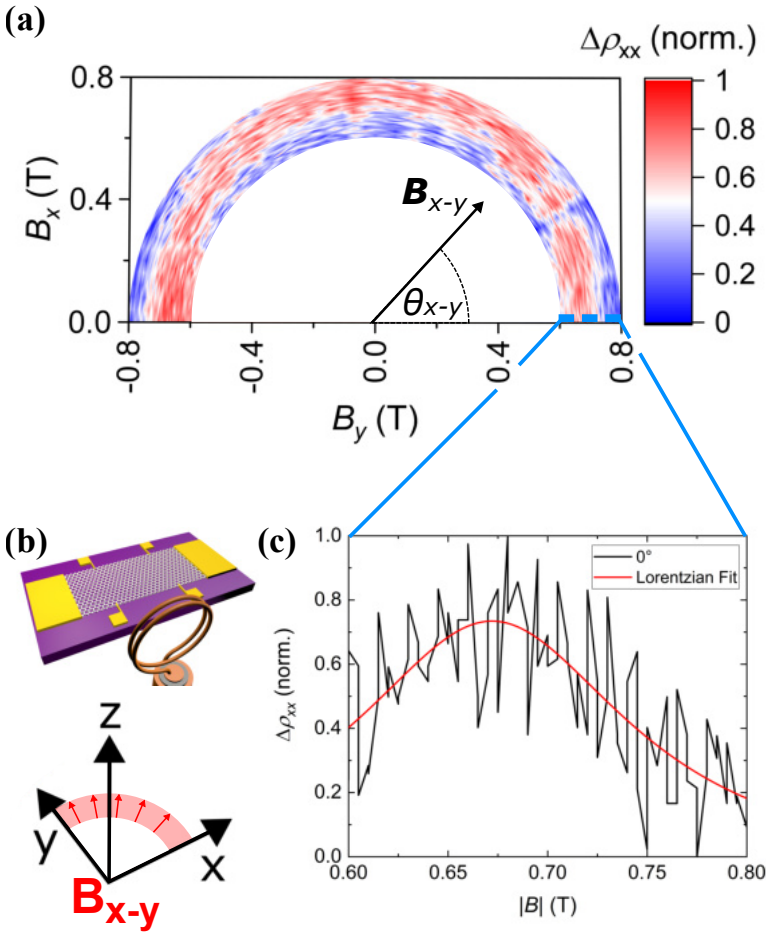

Fig. 6.12. (a) ESR data of the normalized differential resistivity for the radial magnetic field sweeps in the x-y-plane. The resonance peaks are relatively wide compared to the measured magnetic field range, which results in a low color contrast. However, the resonance feature is visibly shifted to lower absolute fields near angles of 0° and 180° (indicated in dark red). The data are recorded at $T = 1.4\,\mathrm{K}$ and $V_g = 0$, with a microwave frequency of $\nu = 19\,\mathrm{GHz}$ and a power of 21 dBm. **(b)** Schematic depiction of the magnetic field orientation in the sample. **(c)** Cross-section of the experimental data of (a) at $\theta_{x-y} = 0°$ (black) and a Lorentzian peak fit (red) with its center at $(0.67 \pm 0.01)\,\mathrm{T}$. The theoretical position is calculated to be 0.68 T.

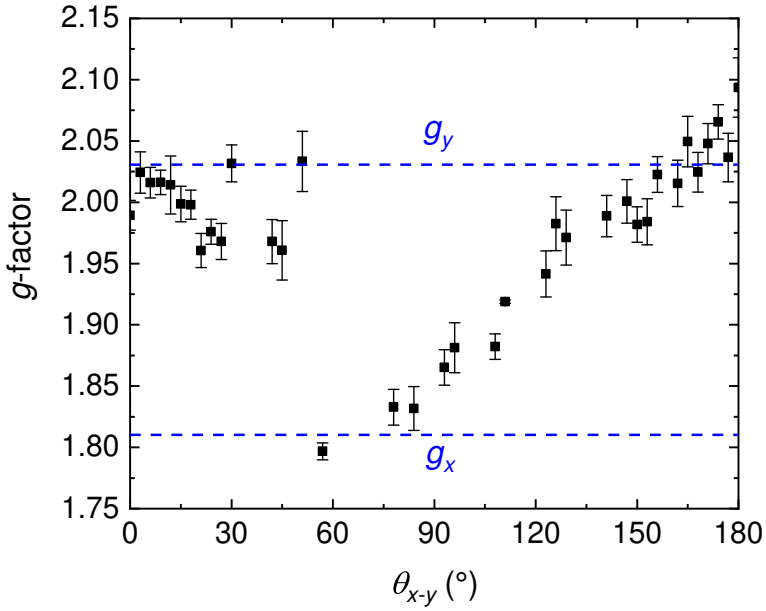

Fig. 6.13. Dependence of the g-factor on the magnetic field angle θ_{x-y}. The data have been extracted from the measurement in Fig. 6.12 by performing a Lorentzian peak fit [68] for each angle and converting the peak position to the corresponding g-factor. The g-factors of the main directions of the coordinate system are indicated by the blue dashed lines. Note that for certain angles, the resonance peak fit did not converge, resulting in missing data points.

The resonance peaks are relatively broad compared to the measured field range, resulting in large regions of red color. Near $\theta_{x-y} = 0°$ and 180°, the resonance is clearly shifted to lower values of $|B_{x-y}|$ and blue off-resonance regions dominate the higher field range, while the opposite is true for $\theta_{x-y} = 90°$. Over the measured range, the resonance position, and thus the g-factor, shifts smoothly with the magnetic field angle.

After a Lorentzian fit [68] to the resonance peak is performed for each angle, the obtained resonance positions can be translated to their respective g-factors: Each resonance can be interpolated to the origin in the parameter space of frequency versus resonance position (similar to, e.g., Fig. 6.7), and thus Eq. 2.44 can be used to calculate g. The g-factor is then plotted with respect to the magnetic field angle θ_{x-y} and the result is shown in Fig. 6.13.

A thorough physical explanation of the data will be given after the results for the two remaining planes of the coordinate system are presented. For this purpose, a theoretical model will be introduced in Section 6.3 which includes the Rashba and ISOC mechanisms.

6.2.2 Magnetic Field in the x-z-Plane

The angle-dependent ESR measurements with the external magnetic field in the x-z-plane are performed with the parameters outlined in Section 6.2. In Fig. 6.14, the normalized differential resistivity versus the angle-dependent magnetic field is shown, which, analogous to the x-y-plane, can be written as

$$\mathbf{B_{x-z}} = B_{x-z} \cdot \cos(\theta_{x-z}) \cdot (\hat{e}_x + \hat{e}_z)/\sqrt{2}, \tag{6.2}$$

where θ_{x-z} is the angle between $\mathbf{B_{x-z}}$ and the x-axis in the x-z-plane. Although the signal-to noise ratio is lower than in the measurement of the x-y-plane, the resonance positions for various angles can be extracted. The regions around $\theta_{x-z} = 0°$ and 180° exhibit resonances (red) at higher absolute values of the magnetic field than at around 90°.

Identically to Section 6.2.1, Lorentzian peak fits [68] are performed for each radial magnetic field sweep, and the g-factor corresponding to the determined resonance position is plotted against the angle, as shown in Fig. 6.15. The large errors for the individually determined values of g reflect the large resonance peak width and a low signal-to-noise ratio. At $\theta_{x-z} = 0°$ and 90°, values close to g_x and g_z should be found, respectively. However, there is a significant deviation from this expectation, which indicates that the accuracy of the experimental method of determining g from only one frequency might be unreliable in some cases. The deviation could also be caused by a slight misalignment of the sample with respect to the specified coordinate system, although the extremal values for g are found near 0°, 90°, and 180° as expected. A detailed theoretical model will be presented in Section 6.3.

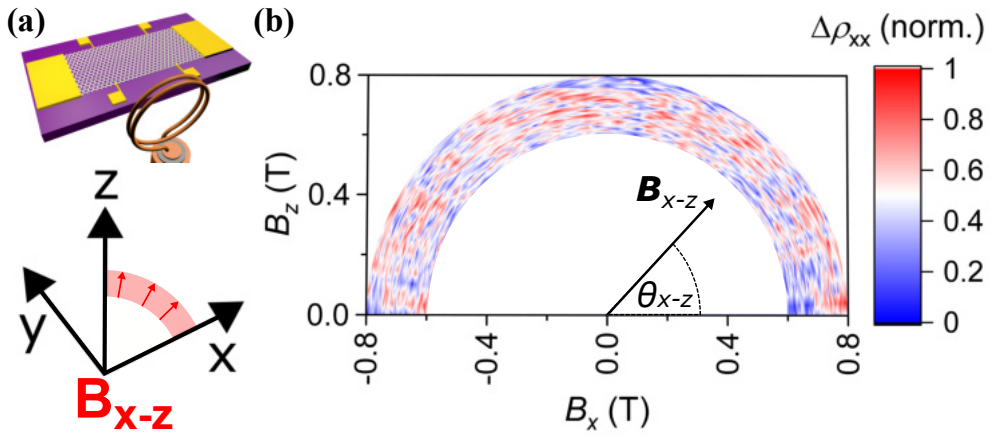

Fig. 6.14. **(a)** Schematic depiction of the magnetic field orientation in the sample. **(b)** ESR data of the normalized differential resistivity for the radial magnetic field sweeps in the x-z-plane. The signal-to-noise ratio is rather low, which makes the resonance positions difficult to determine. However, for some angles, the resonance feature is visible, and it is shifted to higher absolute fields near angles of 0° and 180° (indicated in red) compared to angles near 90°. The data are recorded at $T = 1.4\,\mathrm{K}$ and $V_g = 0$, with a microwave frequency of $\nu = 19\,\mathrm{GHz}$ and a power of 21 dBm.

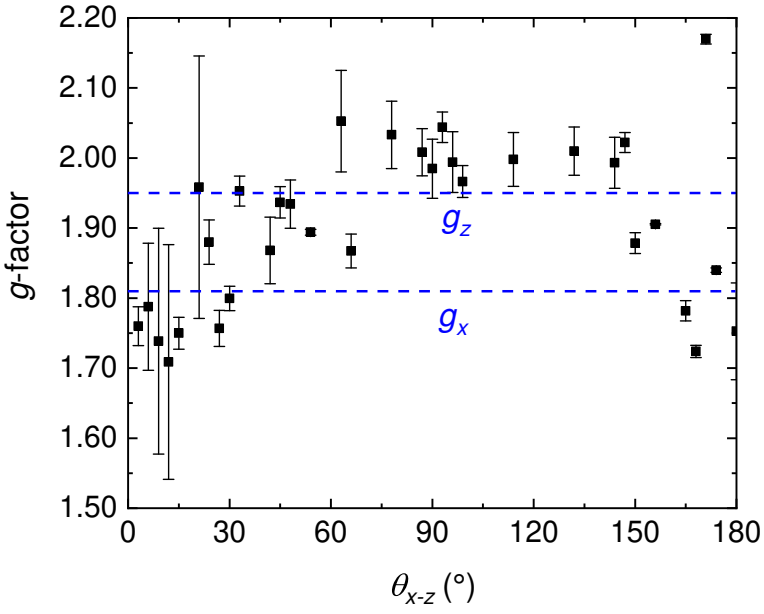

Fig. 6.15. Dependence of the g-factor on the magnetic field angle θ_{x-z}. The data have been extracted from the measurement in Fig. 6.12 by performing a Lorentzian peak fit [68] for each angle and converting the peak position to the corresponding g-factor. The g-factors of the main directions of the coordinate system are indicated by the blue dashed lines. Note that for certain angles, the resonance peak fit did not converge, resulting in missing data points.

6.2.3 Magnetic Field in the y-z-Plane

The angle-dependent ESR measurements with the external magnetic field in the y-z-plane are performed with the parameters outlined in Section 6.2. In Fig. 6.16, the normalized differential resistivity is plotted against the angle-dependent magnetic field, which, analogous to the x-y-plane, can be written as

$$\mathbf{B_{y-z}} = B_{y-z} \cdot \cos(\theta_{y-z}) \cdot (\hat{e}_y + \hat{e}_z)/\sqrt{2}, \tag{6.3}$$

where θ_{y-z} is the angle between $\mathbf{B_{y-z}}$ and the y-axis in the y-z-plane. The single radial measurements exhibit a high signal-to-noise ratio as well as narrow resonances and therefore provide good accuracy for the determination of the angle-dependent g-factor. When the magnetic field angle θ_{y-z} makes a 360° turn, the resonance (red) in Fig. 6.16 follows an oval. For $\theta_{y-z} = 0°$ and 180°, the resonance appears at lower absolute values of the magnetic field than at 90° or 270°.

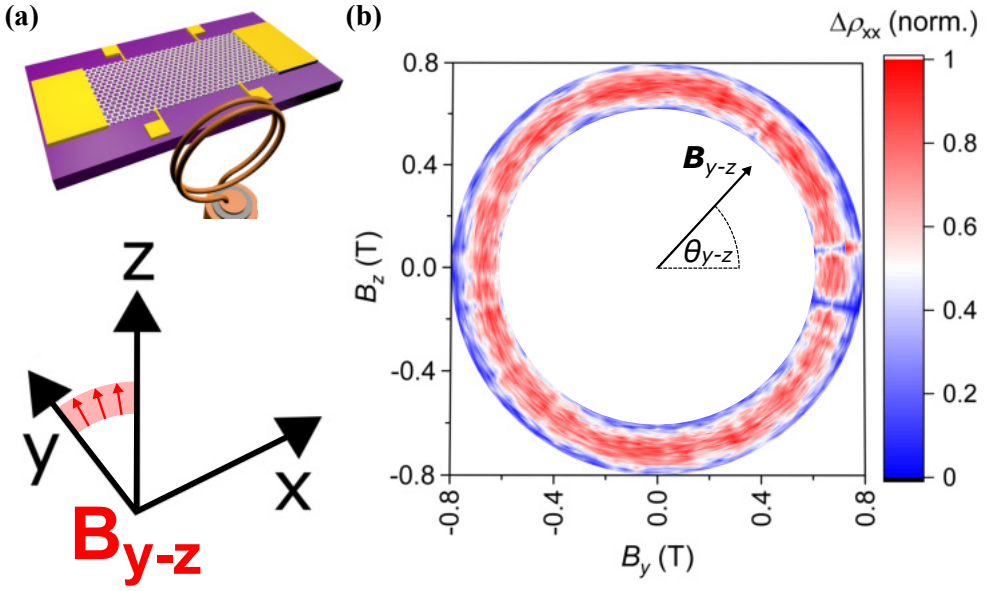

Fig. 6.16. (a) Schematic depiction of the magnetic field orientation in the sample. **(b)** ESR data of the normalized differential resistivity for the radial magnetic field sweeps in the y-z-plane. The resonance peaks are shown in red and they are visibly shifted to lower absolute fields near angles of 0° and 180° as compared to angles of 90° and 270°. Overall, the resonance position varies smoothly with the magnetic field angle θ_{y-z}. The data are recorded at $T = 1.4\,\mathrm{K}$ and $V_g = 0$, with a microwave frequency of $\nu = 19\,\mathrm{GHz}$ and a power of 21 dBm.

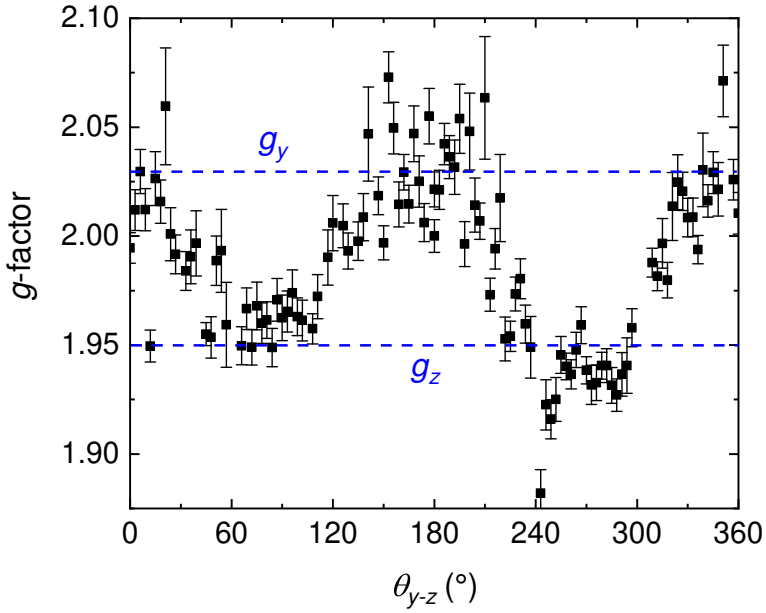

Fig. 6.17. Dependence of the g-factor on the magnetic field angle θ_{y-z}. The data have been extracted from the measurement in Fig. 6.16 by performing a Lorentzian peak fit [68] for each angle and converting the peak position to the corresponding g-factor (black squares). The resulting behavior seems to follow a sine function (red solid line). The g-factors of the main directions of the coordinate system are indicated by the blue dashed lines. Note that for certain angles, the resonance peak fit did not converge, resulting in missing data points.

After the resonance position for each radial magnetic field sweep is determined and converted to the corresponding g-factor (see Section 6.2.1), g is plotted in dependence of the magnetic field angle θ_{y-z}, as shown in Fig. 6.17. Most g-factors exhibit an acceptable error of around 10 % and stay within the expected boundaries, which are set by g_y and g_z. The angular dependence seems to be of sinusoidal nature, spanning two periods over the 360° range and exhibiting extrema near 0°, 90°, 180°, 270°, and 360°.

Extensive tests have been performed to exclude external sources as the origin of the g-factor fluctuations, such as the calibration of the magnet power supplies, the frequency generators, and the lock-ins. The sample and magnetic field orientation have been checked as well as the wiring. It can be concluded that the g-factor varies with respect to the magnetic field angle due to the properties of the graphene, which is the subject of the following section.

6.3 Theoretical Model

In this section, a theoretical model is presented to interpret the angle-dependent data. For this purpose, a microscopic theory for the effective g-factor was developed by M. Prada, which does not only describe the observations, but also grants access to the scale of the involved quantities, i.e., the mixing of the p- and d-orbitals, the energy of the d-orbitals, and the atomic SOC. In general, the Zeeman Hamiltonian describing an electron in a magnetic field which has an angular momentum $\mathbf{L}$ and a spin angular momentum $\mathbf{S}$ is given by

$$\hat{H}_{\text{Zeeman}} = \mu_B \mathbf{B}(\mathbf{L} + g_0 \mathbf{S}), \tag{6.4}$$

with g_0 being the g-factor of the free electron. In contrast, one can describe the same electron via an effective spin model, where the effect of the angular momentum alters the strength of the external magnetic field seen by the electron. Hence, in the effective spin model, the g-factor has to be adjusted, and the effective Hamiltonian can be written as

$$\hat{H}_{\text{eff}} = \mu_B \mathbf{B} \tilde{g} \mathbf{S}, \tag{6.5}$$

where $\tilde{g}$ is a tensor which describes the effective g-factor in three dimensions according to the theory presented in Section 2.4.2, i.e.,

$$\tilde{g} = \begin{pmatrix} g_x & 0 & 0 \\ 0 & g_y & 0 \\ 0 & 0 & g_z \end{pmatrix}, \tag{6.6}$$

and the effective g-factor

$$g_{\text{eff}} = \sqrt{g_x^2 \sin^2\theta \cos^2\gamma + g_y^2 \sin^2\theta \sin^2\gamma + g_z^2 \cos^2\theta}, \tag{6.7}$$

with the angles θ and γ being shown in Fig. 6.18. The model according to Eq. 6.7 is plotted together with the angle-dependent experimental data for the three magnetic field planes in order to verify the viability of the theory. The only input are the experimentally determined values for g_x, g_y, and g_z. The results are shown in Fig. 6.19-6.21. A slight horizontal offset between the model and the data might originate from a slight misalignment of the sample with respect to the magnetic field axes. However, Eq. 6.7 generally describes the experiment with high accuracy. A corresponding visualization of the g-factor

of graphene in three dimensions is displayed in Fig. 6.22.

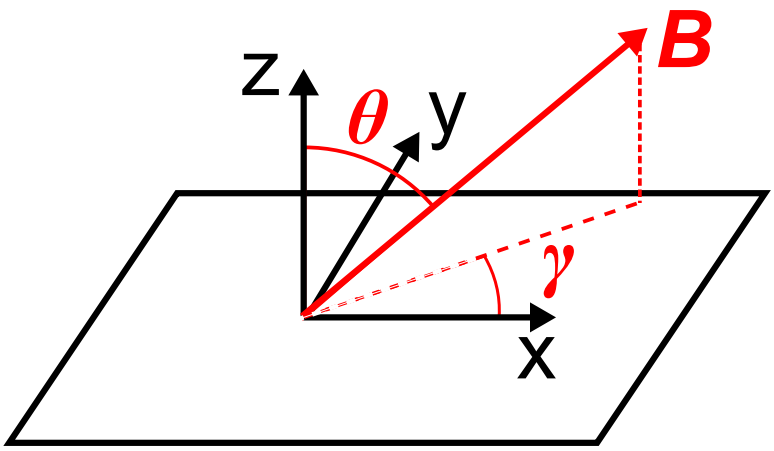

Fig. 6.18. Orientation of the magnetic field (red) with respect to the coordinate system (black), with the orientation of **B** being defined by the angles θ and γ.

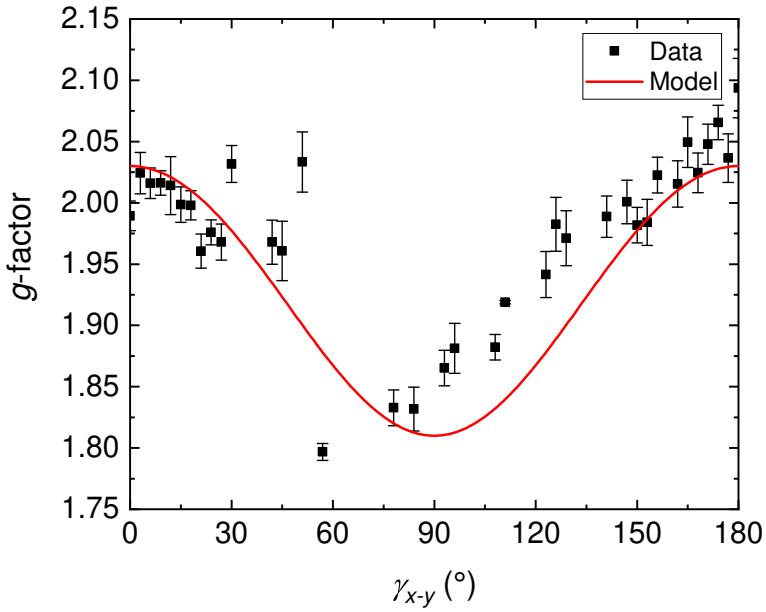

Fig. 6.19. Dependence of the g-factor on the angle γ_{x-y} in the x-y-plane. The theoretical model (red solid line, Eq. 6.7) is in good agreement with the experimental data (black squares). The slight horizontal offset between the model and the experiment could be caused by a slight misalignment of the sample with respect to the main axes of the magnetic field.

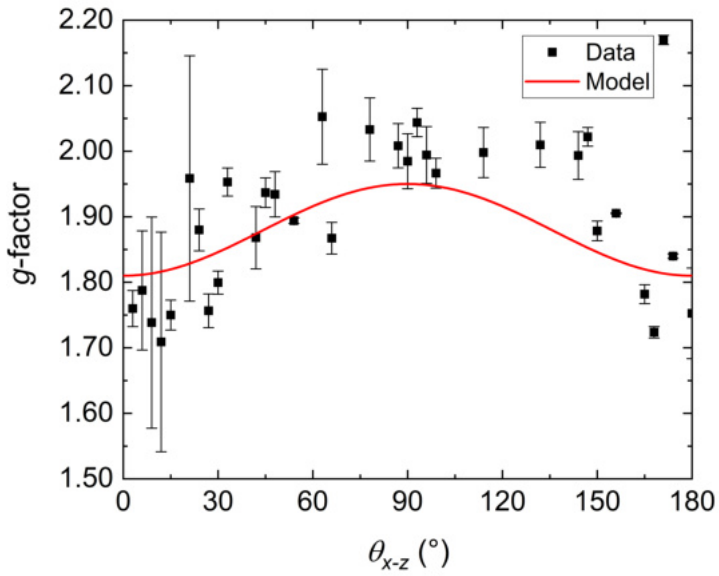

Fig. 6.20. Dependence of the g-factor on the angle θ_{x-z} in the x-z-plane. The theoretical model (red solid line, Eq. 6.7) is in good agreement with the experimental data (black squares).

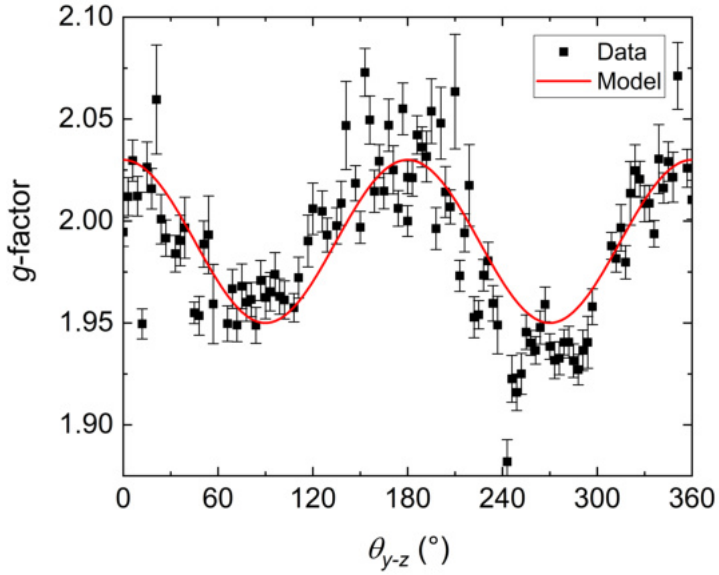

Fig. 6.21. Dependence of the g-factor on the angle θ_{y-z} in the y-z-plane. The theoretical model (red solid line, Eq. 6.7) is in good agreement with the experimental data (black squares). The slight horizontal offset between the model and the experiment could be caused by a slight misalignment of the sample with respect to the main axes of the magnetic field.

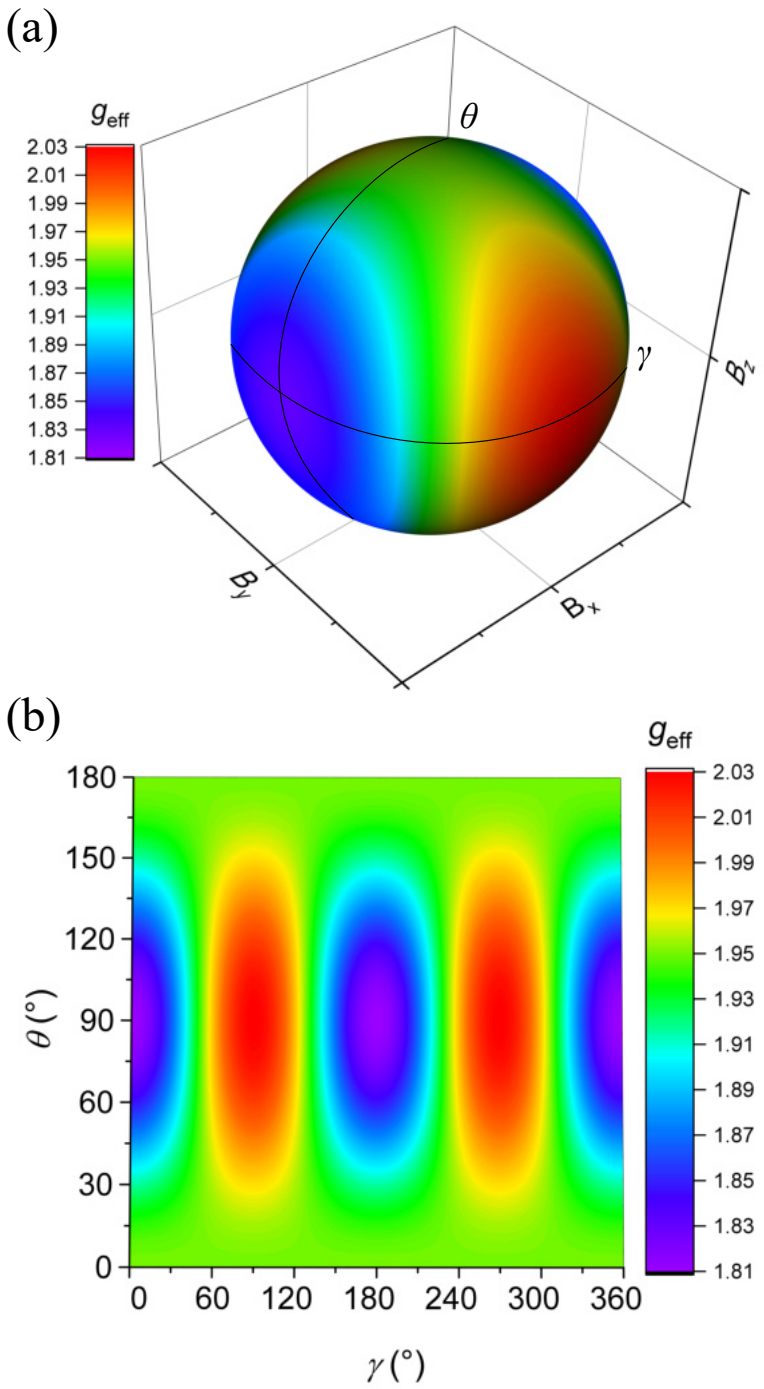

Fig. 6.22. The g-factor of graphene in three dimensions. **(a)** Spherical magnetic field representation with the origin at the center of the sphere. The color gradient on the surface indicates the g-factor for the respective field orientation. The sphere is characterized by the polar angle γ and the azimuthal angle θ, which are used to define a planar projection of the surface in **(b)**. A periodicity in both γ and θ of 180° can be observed.

The tensor $\tilde{g}$ in Eq. 6.5 is constructed in such a way that the resulting energies of $\hat{H}_{\text{Zeeman}}$ and $\hat{H}_{\text{eff}}$ are always equal. For an electron with ground state $|\phi\rangle$, it is required that

$$\langle\phi|\hat{H}_{\text{Zeeman}}|\phi\rangle = \langle\phi|\hat{H}_{\text{eff}}|\phi\rangle, \qquad \langle\phi|\mathbf{B}(\mathbf{L}+g_0\mathbf{S})|\phi\rangle = \langle\phi|\mathbf{B}\tilde{g}\mathbf{S}|\phi\rangle. \tag{6.8}$$

6.3.1 z-Direction

For the z-direction of the magnetic field, the Hamiltonians $\hat{H}_{\text{Zeeman}}$ and $\hat{H}_{\text{eff}}$ in the microscopic crystal field model become fairly simple, yielding

$$\langle(g_z\hat{S}_z)\rangle = \langle(\hat{L}_z + g_0\hat{S}_z)\rangle. \tag{6.9}$$

In order to derive the equation for the effective g-factor for this direction, the ground states $|\phi\rangle$ have to be calculated. The leading corrections of the g-factor can be attributed to the d-orbital mixing in graphene [15, 17]. Thus, by employing perturbation theory and the Slater-Koster matrix elements [107], the corrections can be expressed as

$$\begin{aligned}|\phi\rangle \simeq c_A|p_z^A\rangle + c_B|p_z^B\rangle - \frac{c_A}{\varepsilon_d}(\langle d_{xz}^B|\hat{V}|p_z^A\rangle|d_{xz}^B\rangle + \langle d_{yz}^B|\hat{V}|p_z^A\rangle|d_{yz}^B\rangle)\\ - \frac{c_B}{\varepsilon_d}(\langle d_{xz}^A|\hat{V}|p_z^B\rangle|d_{xz}^A\rangle + \langle d_{yz}^A|\hat{V}|p_z^B\rangle|d_{yz}^A\rangle),\end{aligned} \tag{6.10}$$

where the indices A and B indicate the respective sublattices of graphene. Furthermore, $c_A = \pm c_B \exp(i\phi\tau)$, with + (-) representing the conduction (valence) band, and $\tau = \pm 1$, with $+1$ (-1) relating to the **K** (**K'**) point. Additionally, $|c_A|^2 + |c_B|^2 \simeq 1$, and ε_d is the energy of the d-orbitals. The matrix elements $\langle d_i^\alpha|\hat{V}|p_z^\beta\rangle$ describe the coupling between the p- and d-orbitals and are given by

$$\sum_i \langle\phi_{p_z}^A|\hat{V}|\phi_{d_{yz}}^B\rangle \exp(i\mathbf{k}\cdot\boldsymbol{\delta_i}) \simeq i\frac{3}{2}\tau V_{pd\pi}(1 - \frac{a}{2}(\tau q_x - iq_y)), \tag{6.11}$$

and

$$\sum_i \langle\phi_{p_z}^B|\hat{V}|\phi_{d_{xz}}^A\rangle \exp(i\mathbf{k}\cdot\boldsymbol{\delta_i}) \simeq \frac{3}{2}V_{pd\pi}(1 + \frac{a}{2}(\tau q_x + iq_y)), \tag{6.12}$$

with the relations

$$\langle \phi^A_{p_z} | \hat{V} | \phi^B_{d_{yz}} \rangle = -\langle \phi^B_{p_z} | \hat{V} | \phi^A_{d_{yz}} \rangle^* = \langle \phi^A_{d_{yz}} | \hat{V} | \phi^B_{p_z} \rangle, \tag{6.13}$$

and

$$\langle \phi^A_{p_z} | \hat{V} | \phi^B_{d_{xz}} \rangle = -\langle \phi^B_{p_z} | \hat{V} | \phi^A_{d_{xz}} \rangle^* = \langle \phi^A_{d_{xz}} | \hat{V} | \phi^B_{p_z} \rangle, \tag{6.14}$$

respectively. It is assumed that one is close to the **K** point, i.e., $\mathbf{k} = \mathbf{K} + \mathbf{q}$ and $\mathbf{q} \ll \mathbf{K}$, a is the distance between two neighboring carbon atoms in graphene, and $V_{pd\pi}$ is the mixing potential of the p- and d-orbitals forming π bonds. Eq. 6.13 and 6.14 represent a swap of the sublattices A and B, resulting in a minus sign, which is exactly what the chirality operator $\hat{h}_q = \hat{\sigma} \cdot \mathbf{q}/|\mathbf{q}|$ does to the Hamiltonian [108]. Without the property of chirality, the matrix elements would be zero. Additionally, they are spin-diagonal, i.e., they do not contain spin up-spin down mixing terms to leading order. Hence, only the expectation value $\langle \hat{L}_z \rangle$ needs to be calculated in order to access the g-factor, and by using $\langle d^\alpha_i | \hat{L}_z | p_z \rangle = 0$ and $\langle d^\alpha_{xz} | \hat{L}_z | d^\beta_{yz} \rangle = i\delta_{\alpha\beta}$, one obtains

$$\begin{aligned}
\langle \phi | \hat{L}_z | \phi \rangle \simeq & \frac{c_A c_A^*}{\varepsilon_d^2} (\langle p_z^B | \hat{V} | d_{xz}^A \rangle \langle d_{xz}^A | \hat{L}_z | d_{yz}^A \rangle \langle d_{yz}^A | \hat{V} | p_z^B \rangle \\
& + \langle p_z^B | \hat{V} | d_{yz}^A \rangle \langle d_{yz}^A | \hat{L}_z | d_{xz}^A \rangle \langle d_{xz}^A | \hat{V} | p_z^B \rangle) \\
& + \frac{c_B c_B^*}{\varepsilon_d^2} (\langle p_z^A | \hat{V} | d_{xz}^B \rangle \langle d_{xz}^B | \hat{L}_z | d_{yz}^B \rangle \langle d_{yz}^B | \hat{V} | p_z^A \rangle \\
& + \langle p_z^A | \hat{V} | d_{yz}^B \rangle \langle d_{yz}^B | \hat{L}_z | d_{xz}^B \rangle \langle d_{xz}^B | \hat{V} | p_z^A \rangle) \\
= & -2i^2 \tau \frac{\alpha^2}{\varepsilon_d^2} (|c_A|^2 - |c_B|^2) = 2\tau\sigma_z \frac{\alpha^2}{\varepsilon_d^2},
\end{aligned} \tag{6.15}$$

where $\alpha = \frac{3}{2} V_{pd\pi}$ is a factor that is linearly proportional to the orbital coupling potential. The result for the g-factor in z-direction can then be written as

$$g_z = g_0 + 2\tau \frac{\alpha^2}{\varepsilon_d^2} \sigma_z = g_0 + \Delta g_z. \tag{6.16}$$

With this equation and comparing g_0 to the experimental data (summarized in Tab. 6.1), it is apparent that $\Delta g_z \approx -0.05$, i.e., $\sigma_z \tau < 0$, which corresponds to the molecular ground state of graphene ($\langle \sigma_z \tau \rangle$ is obtained through third order

corrections). Interestingly, the quantity $\alpha/\varepsilon_d \simeq 0.0871$ has already been determined via density functional theory by Konschuh *et al.* (2010) [16], resulting in an upper limit of

$$\Delta g_z = 2\frac{\alpha^2}{\varepsilon_d^2}\langle\tau\sigma_z\rangle = -2\frac{\alpha^2}{\varepsilon_d^2} \simeq -0.015. \tag{6.17}$$

which deviates from the experimentally determined value of -0.05. However, the theoretical value has lead to underestimating the intrinsic band gap Δ_I of graphene as 24 µeV [16] instead of 42 µeV. One could therefore argue to use the experimental value of g_z in order to improve the theoretical parameters:

$$|\Delta g_z| = 0.05 = 2\frac{\alpha^2}{\varepsilon_d^2} \rightarrow \frac{\alpha}{\varepsilon_d} = 0.1581, \tag{6.18}$$

which is roughly a factor of two larger than the theoretical value, and could explain the originally underestimated gap. Additionally, α/ε_d determines the mixing of the *p*- and the *d*-orbitals, and the experimentally determined value results in a contribution of the *d*-orbitals which is around 6 % larger than expected. Moreover, this mixing parameter allows to calculate the atomic SOC χ_d, which is dominated by the contribution of the *d*-orbitals:

$$\Delta_I = 42\,\mu\text{eV} = 4\frac{\alpha^2}{\varepsilon_d^2}\chi_d \rightarrow \chi_d \simeq 0.42\,\text{meV}, \tag{6.19}$$

while the value estimated via density functional theory is 0.8 meV [16].

6.3.2 x-Direction

In contrast to the z-direction, an effective spin model is employed for the x-direction, which is oriented in plane and parallel to the current through the graphene. This minimal model is defined in a spin and pseudospin (bi-spinor) basis of $\boldsymbol{s} \otimes \boldsymbol{\sigma} = \{A\uparrow, B\uparrow, A\downarrow, B\downarrow\}$, and the Hamiltonian is given by

$$\begin{aligned}\hat{H} = {} & g_0\mu_0 B(\hat{s}_x \otimes \mathbb{I}) + \alpha_k(\mathbb{I} \otimes \hat{\sigma}_x) + \lambda_R(\hat{s}_x \otimes \hat{\sigma}_y - \hat{s}_y \otimes \hat{\sigma}_x) \\ & + \lambda_I(\hat{s}_z \otimes \hat{\sigma}_z),\end{aligned} \tag{6.20}$$

where $\mathbb{I}$ is the 2D identity matrix, $\alpha_k = \hbar v_F k_x$, and $\hat{s}_\alpha$ and $\hat{\sigma}_\beta$ are the Pauli matrices acting on spin and pseudospin, respectively. The four terms are, in

order, the Zeeman term, the Dirac term, the Rashba SOC term, and the intrinsic SOC term. The Zeeman term dictates that the spin of the eigenstates points along x, while the Dirac term quantizes the pseudospin along the same direction, since transport is along x. This is also the reason why a Dirac term including $\hat{\sigma}_y$ can be neglected here. Both SOC terms mix spin-up and spin-down states. Note that this Hamiltonian includes additional relevant components compared to the z-direction as the Dirac and the Rashba terms did not play a role before (they are oriented in plane).

For convenience, the order of spin and pseudospin degrees of freedom is swapped, resulting in an altered bi-spinor basis $\{+_x\uparrow_x, +_x\downarrow_x, -_x\uparrow_x, -_x\downarrow_x\}$, where the sublattice spin A and B has been replaced by + and -, respectively, and the index x represents the collinear alignment with the x-direction.

For the g-factor calculation, perturbation theory is employed in the absence of a magnetic field (no Zeeman term), with the Dirac term being the unperturbed term, while the two SOC terms represent the perturbation mixing spin-up and spin-down states. In other words, one starts with a symmetry-broken eigenstate and calculates the correction that arises from SOC. One receives for the zeroth order of perturbation

$$\hat{H}^0 = \alpha_k(\mathbb{I}\otimes\hat{\sigma}_x) = \alpha_k \begin{pmatrix} 1 & 0 & 0 & 0 \\ 0 & 1 & 0 & 0 \\ 0 & 0 & -1 & 0 \\ 0 & 0 & 0 & -1 \end{pmatrix}, \tag{6.21}$$

and for the first order

$$\hat{H}^1 = -\lambda_R(\hat{s}_y\otimes\hat{\sigma}_x) \begin{pmatrix} 0 & 1 & 0 & 0 \\ 1 & 0 & 0 & 0 \\ 0 & 0 & 0 & -1 \\ 0 & 0 & -1 & 0 \end{pmatrix} + \lambda_I \begin{pmatrix} 0 & 0 & 0 & 1 \\ 0 & 0 & 1 & 0 \\ 0 & -1 & 0 & 0 \\ -1 & 0 & 0 & 0 \end{pmatrix}. \tag{6.22}$$

In the zeroth order, the ground state is given by $|\phi^0_{GS}\rangle = |-_x\rangle$, a degenerate state with negative sublattice spin and arbitrary real spin, and the eigenenergy $E^0_0 = -\alpha_k$. The first term (Rashba) in Eq. 6.22 does not yield any net contributions as it does not mix the two degrees of freedom. However, the second term (ISOC) mixes spin and pseudospin, breaking the degeneracy.

When applying degenerate perturbation theory to the first order on one of the ground states, in this case $|\phi^0_{GS}\rangle = |-_x \downarrow_x\rangle$, one receives

$$\begin{aligned} |\phi_{GS}\rangle_\downarrow &\simeq \frac{1}{c_n}\left(|\phi^0_{GS}\rangle_\downarrow + \sum_j \frac{1}{E^0_0 - E^0_j}\langle j|\hat{H}^1|\phi^0_{GS}\rangle|j\rangle\right) \\ &= \frac{1}{c_n}(|-_x \downarrow_x\rangle + \beta|+_x \uparrow_x\rangle), \end{aligned} \tag{6.23}$$

with

$$\beta = \frac{\lambda_I}{2\alpha_k}, \qquad c_n^2 = 1 + \beta^2. \tag{6.24}$$

Note that the Rashba term plays no role in the degenerate perturbation theory, since it does not lift any degeneracies (ones in the off-diagonal elements). Now that the ground state $|\phi_{GS}\rangle_\downarrow$ is known, the expectation values of the effective Hamiltonian $\hat{H}_{\text{eff}}$ and the Zeeman Hamiltonian $\hat{H}_{\text{Zeeman}}$ need to be matched in order to access the g-factor (similar to the z-direction). They are given by

$$\langle \hat{H}_{\text{eff}}\rangle_\downarrow = g_x \mu_B B_x \langle \hat{s}_x\rangle_\downarrow = -\frac{1}{2} g_x \mu_B B_x, \tag{6.25}$$

and

$$\begin{aligned} \langle \hat{H}_{\text{Zeeman}}\rangle_\downarrow &= \langle \phi_{GS}|\hat{H}_{\text{Zeeman}}|\phi_{GS}\rangle_\downarrow \simeq g_0 \mu_B B_x \langle \phi_{GS}|\hat{s}_x|\phi_{GS}\rangle_\downarrow \\ &\simeq -\frac{1}{2} g_0 \mu_B B_x \left(\frac{1-\beta^2}{c_n^2}\right). \end{aligned} \tag{6.26}$$

The comparison between those results yields the g-factor in x-direction

$$g_x \simeq g_0 \frac{1-\beta^2}{c_n^2} = g_0 \frac{1-\beta^2}{1+\beta^2} \simeq g_0(1-2\beta^2), \tag{6.27}$$

and the correction to the free electron g-factor

$$\Delta g_x = \frac{\lambda_I^2}{2\hbar^2 v_F^2 k_x^2}. \tag{6.28}$$

With the experimental results $g_x = 1.81$, $\Delta g_x = 0.19$, and $\lambda_I = \Delta_I/2 \simeq 21\,\mu\text{eV}$, one receives $\hbar v_F k_x \simeq 34\,\mu\text{eV}$, or $v_F k_x \simeq 5.17 \cdot 10^{10}\,\text{s}^{-1}$. Inserting the Fermi velocity of ideal graphene yields $k_x \simeq 10^4\,\text{m}^{-1}$.

6.3.3 y-Direction

At the time of writing this thesis, the theory for the y-direction is a work in progress. The Hamiltonian would be similar to the one presented for the x-direction, with the difference of the magnetic field resulting in a different quantization direction of the electron spin. The overall correction to the g-factor calculated from perturbation theory should be close to zero as the experiment suggests ($g_y = 2.03 \simeq g_0$). Preliminary results show that the factor λ_I^2 from Eq. 6.28 would become $(\lambda_I + \lambda_R)^2$, resulting in the condition $\lambda_I \approx -\lambda_R$, which, in principle, would be possible.

7 Enhancement of ESR by Magnetic Nanoparticles

In this chapter, the influence of magnetic nanoparticles on the ESR signal is studied. When graphene is placed directly on such particles, the resonance peak height is found to increase drastically. When external in-plane fields are applied, the magnetization of the nanomagnets appears to rotate following the field direction and strength. When additional in-plane AC fields are applied, the magnetization seems to instantaneously switch. Both effects are observed in the resistivity of the graphene layer. Preliminary experimental results as well as theoretical speculations about the origin of these effects will be presented in the following sections.

7.1 Magnetoresistance and ESR in Out-of-Plane Direction

The ESR studies are performed on sample 3, a 200 µm × 22 µm graphene Hall bar, which is placed on Pt/Co/Pt magnetic nanoparticles. These nanodots exhibit a perpendicular magnetic anisotropy as well as a hexagonal short-range order with a mean spacing of around 70 nm. The Si/SiO_2 substrate allows to apply a back-gate voltage. A detailed description of the sample can be found in Section 3.4.3.

Preliminary ESR measurements for a magnetic field B_z along the z-direction (for a schematic of the setup, see Fig. 7.1) have been performed in Kronos at a temperature of 1.4 K, while ongoing measurements probe all magnetic field directions in the Prometheus system, also at 1.4 K.

Initially, a sweep of the back-gate voltage V_g at $B_z = 0$ is performed in Kronos by applying a constant current of 2 nA to the sample, while increasing the gate voltage from 0 to 100 V in steps of 10 mV and recording the longitudinal voltage. As shown in Fig. 7.2, the CNP lies beyond the maximal gate voltage of $V_g = 100$ V, indicating hole-transport in the experimentally accessible regime. The resistivity change of around 200 Ω over the entire voltage range is low compared to the measurements of the graphene samples in Chapter 5, where

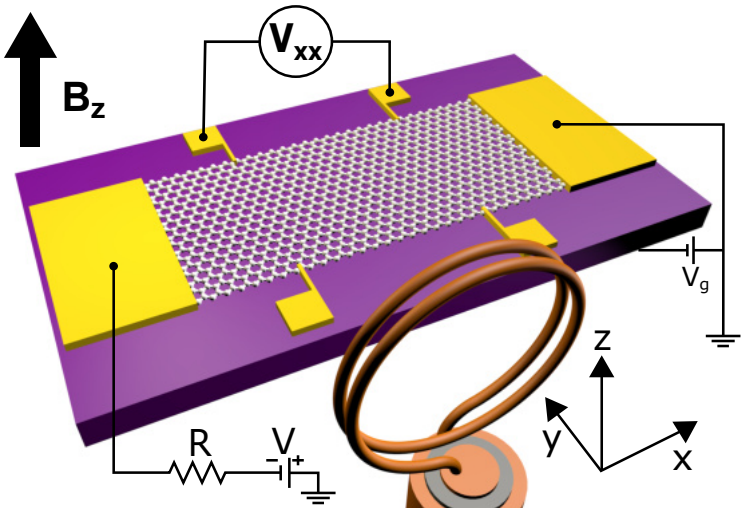

Fig. 7.1. Experimental setup for the magnetoresistance and ESR measurements of sample 3. The external magnetic field is oriented in z-direction, i.e., perpendicular to the sample plane, while the AC antenna field points along the y-axis. A constant current is applied in x-direction and the longitudinal voltage V_{xx} is measured. The charge carrier density can be controlled via the back-gate voltage V_g.

the change is up to two orders of magnitude higher. This indicates that the metallic nanodots might be shielding the graphene from the electric field which is applied through the back-gate.

For further sample characterization, the magnetoresistance at $V_g = 0$ is probed by applying a current of 2 nA to the sample, while sweeping the magnetic field from -10 T to 10 T in steps of 20 mT. The measured total Hall resistivity ρ_{tot} exhibits a longitudinal component due to a non-ideal contact symmetry, i.e., a slight misalignment of the probing contacts with respect to the current direction. By assuming zero Hall resistivity at zero magnetic field, the Hall data can be symmetrized as follows [22]: The measured Hall resistivity can be expressed as $\rho_{tot} = \rho_{long} + \rho_{xy}$, where the longitudinal component obeys $\rho_{long}(-B) = \rho_{long}(B)$, while the transverse component follows $\rho_{xy}(-B) = -\rho_{xy}(B)$. One can then extract the transverse (Hall) resistivity as $\rho_{xy}(B) = \rho_{tot}(B) - \rho_{long}(B) = \rho_{tot}(B) - 1/2(\rho_{tot}(B) + \rho_{tot}(-B))$. The longitudinal measurement of ρ_{xx} does not exhibit an asymmetry and is displayed as raw data in Fig. 7.3. The results yield a charge carrier density of $n = 1.86 \cdot 10^{13}\,\mathrm{cm}^{-2}$ and a charge carrier mobility of $\mu = 70.9\,\mathrm{cm}^{-2}\mathrm{V}^{-1}\mathrm{s}^{-1}$. The density is rather high compared to the graphene samples 1 and 2, while the mobility is very low, which is most likely caused by the metallic nanodots, which are in contact

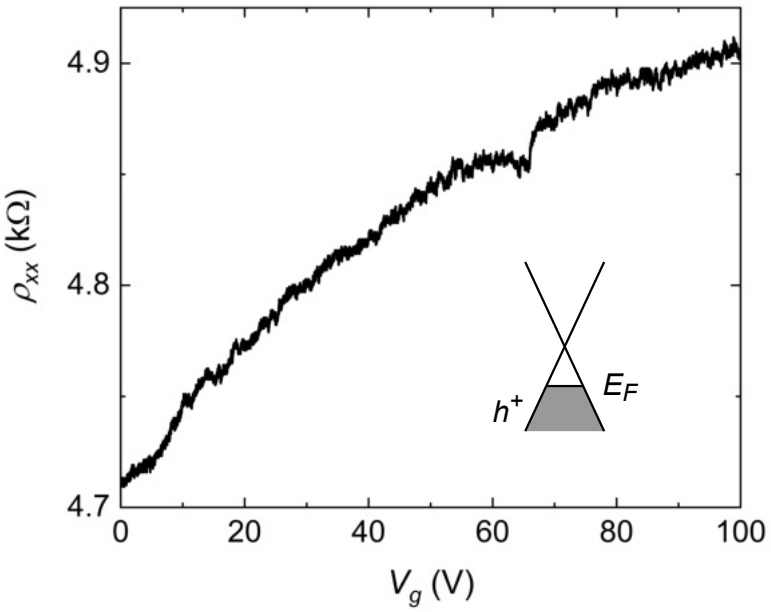

Fig. 7.2. Longitudinal resistivity in dependence of the back-gate voltage at $T = 1.4\,\mathrm{K}$ and $B = 0$. The CNP lies beyond the maximal value of $V_g = 100\,\mathrm{V}$, i.e, only the hole-transport regime is accessible in the experiment, as indicated by the schematic drawing in the inset.

with the graphene and act as impurities. The negative slope of the transverse resistivity confirms the hole-like nature of the transport. Additionally, the magnetoresistance data shows no hysteresis in a reverse magnetic field sweep.

During the subsequent ESR measurements, the current is set to 2 nA and the back-gate voltage is kept constant at $V_g = 0$. The frequency ν is set to values between 15 GHz and 30 GHz in increments of 1 GHz with a radiation power of 19 dBm, and for each frequency, the magnetic field is swept between $-1.5\,\mathrm{T}$ and 1.5 T in steps of 5 mT. A background measurement without radiation is performed for each back-gate voltage.

The background measurement and and an exemplary measurement at $\nu = 30\,\mathrm{GHz}$ are shown in Fig. 7.4. The resonance peak, which is $\sim 30\,\Omega$ in height, can be resolved without calculating $\Delta\rho_{xx}$. This is surprising, since in Section 5.1.3, and especially in Fig. 5.15, the measurements show that the peak height decreases (and eventually vanishes) with increasing distance from the CNP. The high charge carrier density in sample 3 suggests that the distance to the CNP is even greater than in the measurements from Fig. 5.15. A peak height of $30\,\Omega$ this far away from the CNP is therefore an improvement of at least a factor of 5 compared to the samples without magnetic nanoparticles

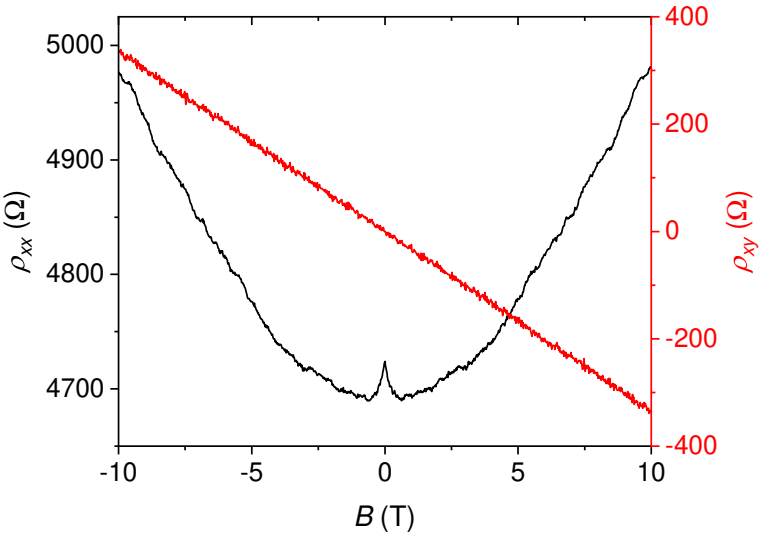

Fig. 7.3. Longitudinal (black) and Hall resistivity (red) in dependence of the external magnetic field at $T = 1.4\,\mathrm{K}$ and $V_g = 0$. The measurements yield values for the charge carrier density and mobility of $n = 1.86 \cdot 10^{13}\,\mathrm{cm}^{-2}$ and $\mu = 70.9\,\mathrm{cm}^{-2}\mathrm{V}^{-1}\mathrm{s}^{-1}$, respectively. The negative slope of the transverse resistivity is an indication for hole-like transport.

($\Delta\rho_{Peak} < 5\,\Omega$). A feasible explanation could be based on the local electron spin polarization in the vicinity of the nanomagnets which is enhanced compared to the prediction of the Maxwell-Boltzmann distribution (see Section 2.4). The increased change in resistance can then be explained in terms of a larger number of spin-flips that can be induced by the microwave radiation. This concept is illustrated in Fig. 7.5

The second (lower-field) ESR peak (see Chapter 5) is not sufficiently resolved using the Kronos setup. This might be due to the noise in the data whenever a frequency is applied, which does not appear in measurements performed on the same sample in the Prometheus setup. These issues are probably related to insufficient thermal contact with the 1.4 K bath.

The results for various frequencies are presented in Fig. 7.6 where the raw frequency data are shown, i.e., no background signal is subtracted to enhance the visibility of the resonances. Additionally, the ESR features do not appear as a peak for all frequencies. The type of feature seems to be frequency-dependent as low frequencies tend to rather produce resonance dips and higher frequencies resonance peaks. This behavior has not been studied extensively, however, one could speculate that the effective sample temperature plays an important role, since it is frequency-dependent due to the power absorption of the signal line

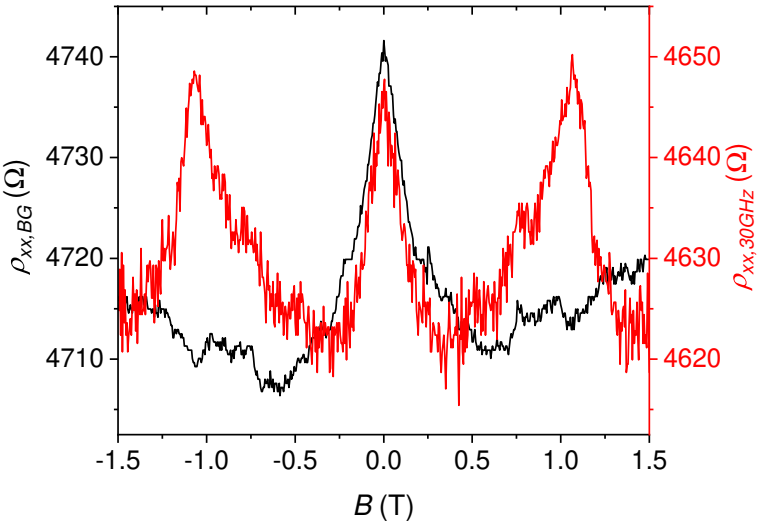

Fig. 7.4. Longitudinal magnetoresistance without radiation (black) and with $\nu = 30\,\mathrm{GHz}$ and a power of 19 dBm (red). Large resonance peaks with a height of $\sim 30\,\Omega$ are visible around $|B| = 1\,\mathrm{T}$. The data have been recorded at $T = 1.4\,\mathrm{K}$ and $V_g = 0$.

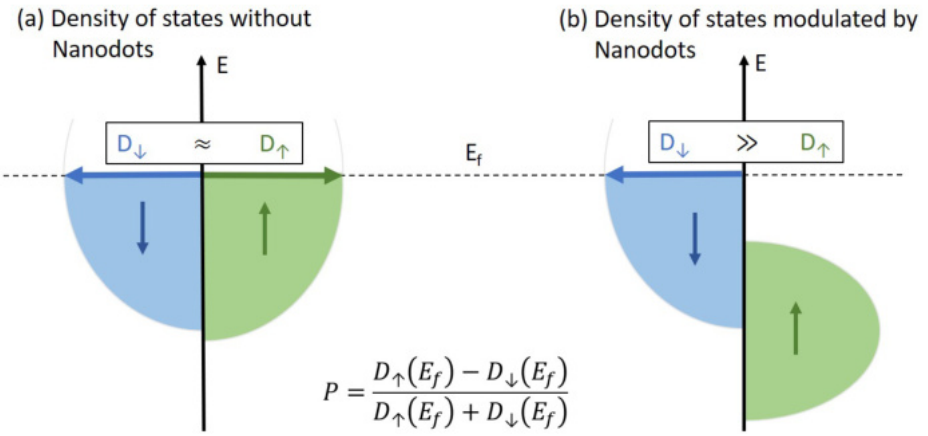

Fig. 7.5. Density of spin states for graphene **(a)** without and **(b)** with magnetic nanoparticles. Without the nanodots, the spin polarization is given by the Maxwell-Boltzmann distribution, and it is low compared to the (locally) enhanced polarization when the dots are present. Image courtesy of T. Anlauf.

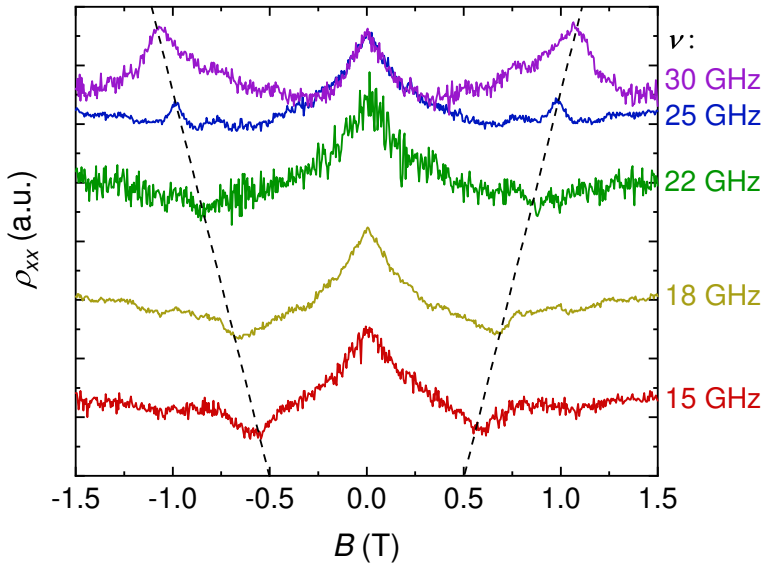

Fig. 7.6. $\rho_{xx,\nu}(B)$ for various frequencies between 15 GHz and 30 GHz. The ESR peaks, which are symmetric in B, shift linearly with the applied microwave frequency (indicated by the dashed lines), while the peak at zero field stems from the the weak localization in the sample. The measurements are offset for clarity. The data are recorded at $T = 1.4\,\mathrm{K}$ and $V_g = 0$, with a microwave radiation power of 19 dBm.

(see Section 4.4). In a simplified picture, the sample temperature is influenced by the resonant absorption and radiative heating leading to the excitation of a significant number of charge carriers to higher energetic (spin) states, causing a scenario comparable to a population inversion. The result would then be visible in the resistivity as an "inversion" of the resonance feature. This topic has to be studied more thoroughly, e.g., by performing a peak analysis for varying signal power at a constant frequency.

The g-factor for this direction of the magnetic field, deduced from the slope in Fig. 7.7 as $g_z = 1.94 \pm 0.02$, does not seem to be influenced significantly by the magnetic nanoparticles. A more extensive set of data would be necessary in order to determine whether the nanoparticles contribute a significant magnetic field to the ESR measurements. In this case, a positive x-intercept of the linear fit would be expected without affecting the slope, indicating a remnant field when the external field is set to zero. However, the particles cover only $\sim 10\,\%$ of the sample area, and the stray field at the nanoparticle/graphene interface is $< 50\,\mathrm{mT}$ [109]. Thus, one would expect a rather small x-intercept, which cannot be resolved with the limited amount of frequencies available in this preliminary data set.

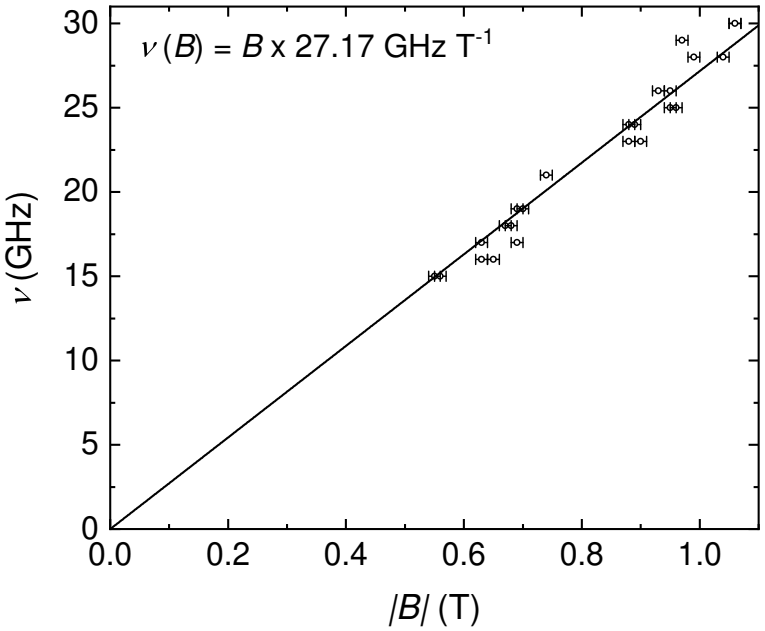

Fig. 7.7. Antenna frequency versus ESR peak position in magnetic field corresponding to the data from Fig. 7.6. The slope of the linear fit is calculated as $(27.17 \pm 0.25)\,\mathrm{GHzT}^{-1}$, which corresponds to a g-factor of $g_z = 1.94 \pm 0.02$, and does not seem to be influenced significantly by the magnetic nanoparticles. An outlier at 20 GHz has been removed.

Therefore, similar to the data analysis in Chapter 5 and Chapter 6, the fit in Fig. 7.7 is set through the origin. The errors of the peak positions are estimated to be around $\pm 10\,\mathrm{mT}$, originating from the inaccuracy of the magnet power supply (3 mT), the error of the resonance peak fit (3 mT), and a potential tilt angle of the sample of up to 5° with respect to the magnetic field (4 mT).

7.2 Magnetoresistance and ESR in the In-Plane Directions

In this section, the most important preliminary results for the in-plane magnetic field directions are presented. These and ongoing measurements are performed by T. Anlauf, and a more in-depth analysis is available in his thesis [110].

Magnetoresistance for the in-plane directions of the magnetic field B_x and B_y has been probed in the Prometheus system at a temperature of $T = 1.4\,\mathrm{K}$ and a back-gate voltage of $V_g = 0$. A schematic overview of the orientation of sample 3 is shown in Fig. 7.8. A constant current of 2 nA is applied to the sample, while

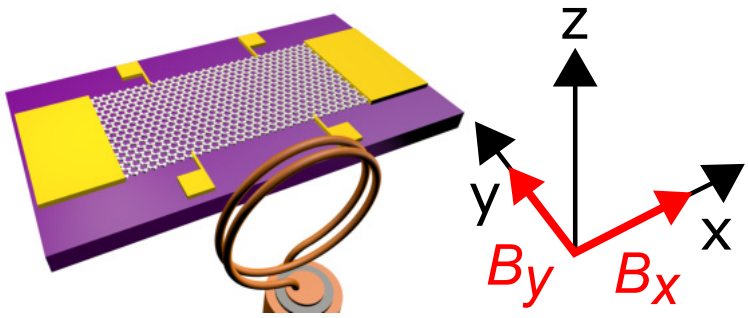

Fig. 7.8. Experimental setup for the magnetoresistance and ESR measurements of sample 3. The external magnetic field is oriented in either x- or y-direction, while the AC antenna field always points along the y-axis.

the magnetic field is swept between $-1\,\mathrm{T}$ and $1\,\mathrm{T}$ (and in reverse) in steps of $5\,\mathrm{mT}$ for each of the two directions x and y. The resulting data is displayed in Fig. 7.9. A slight hysteresis is observed in both cases, indicating a response of the magnetic nanoparticles to the external field. By applying an in-plane field, they are forced to rotate their magnetic orientation from the intrinsic out-of-plane direction to the energetically less favorable in-plane direction x or y, respectively.

The sample was irradiated with microwaves of various frequencies between $10\,\mathrm{GHz} \leq \nu \leq 30\,\mathrm{GHz}$ with a power of 19 dBm to the sample while sweeping the magnetic field. In x-direction, the hysteresis is enhanced once the microwaves are turned on, as illustrated in Fig. 7.10a. Additionally, the obtained data resembles a two-level system regarding the sample resistivity, with the critical "switching" field varying with the sweep direction. A feasible model that explains this behavior is based on microwave-assisted switching of the magnetic orientation: When sweeping from a high to a low absolute in-plane field, the nanomagnets are less likely to stay in the energetically unfavorable in-plane orientation with diminishing field. The sum of the magnetic moments of all nanoparticles, which is reflected in the sample resistivity, varies smoothly (approximately linearly) with B_x in the absence of radiation (see Fig. 7.8a).

When the radiation is switched on, the microwaves provide the required energy for the nanomagnets to switch instantaneously to their preferred out-of-plane orientation at a certain threshold field, which seems to be $|B_x| \approx 0.5\,\mathrm{T}$. Subsequently, the nanomagnets stay in this orientation until B_x overcomes this threshold, again at $|B_x| \approx 0.5\,\mathrm{T}$. The resistance of the graphene layer responds strongly to changes in the orientation of the magnetic domains of the nanoparticles. While the electron spin is always collinear with the external field, the

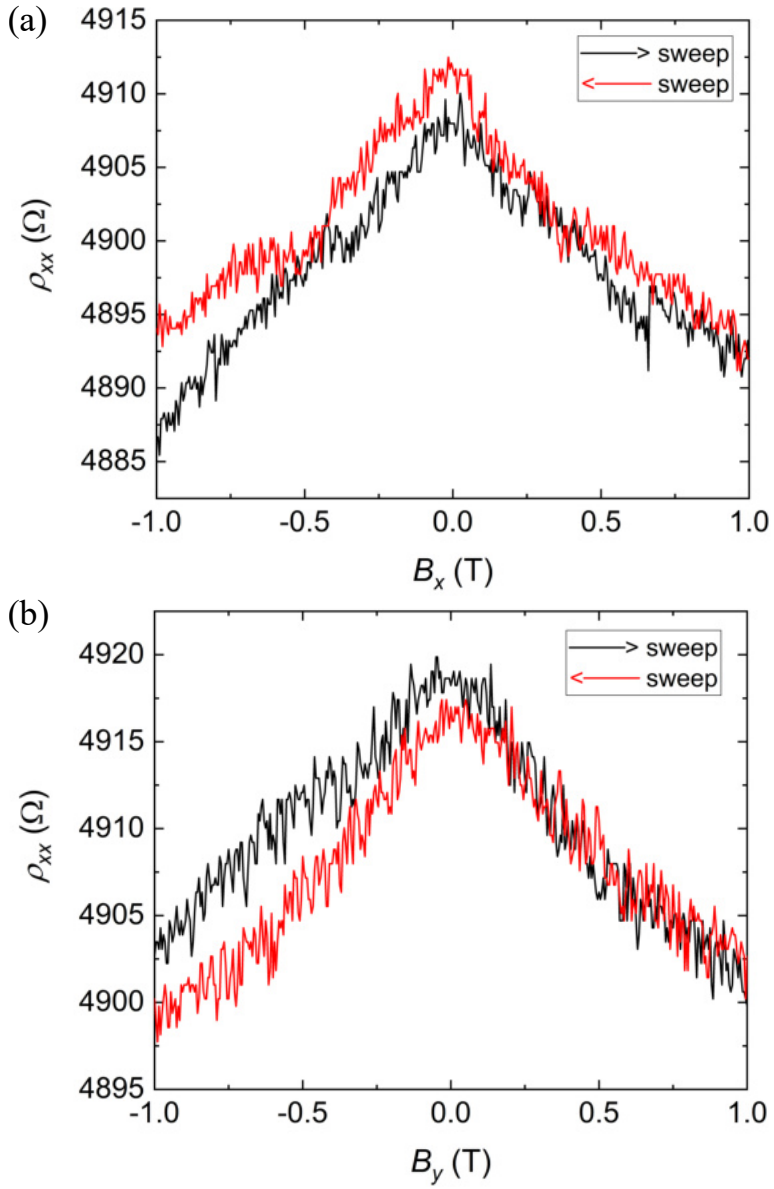

Fig. 7.9. Magnetoresistance for the x-direction **(a)** and the y-direction **(b)** of the external magnetic field. The data are recorded at $T = 1.4\,\mathrm{K}$ and $V_g = 0$. The black line indicates a magnetic field sweep from negative to positive values, and the reverse direction for the red line. A slight hysteresis is observed for both orientations B_x and B_y, respectively.

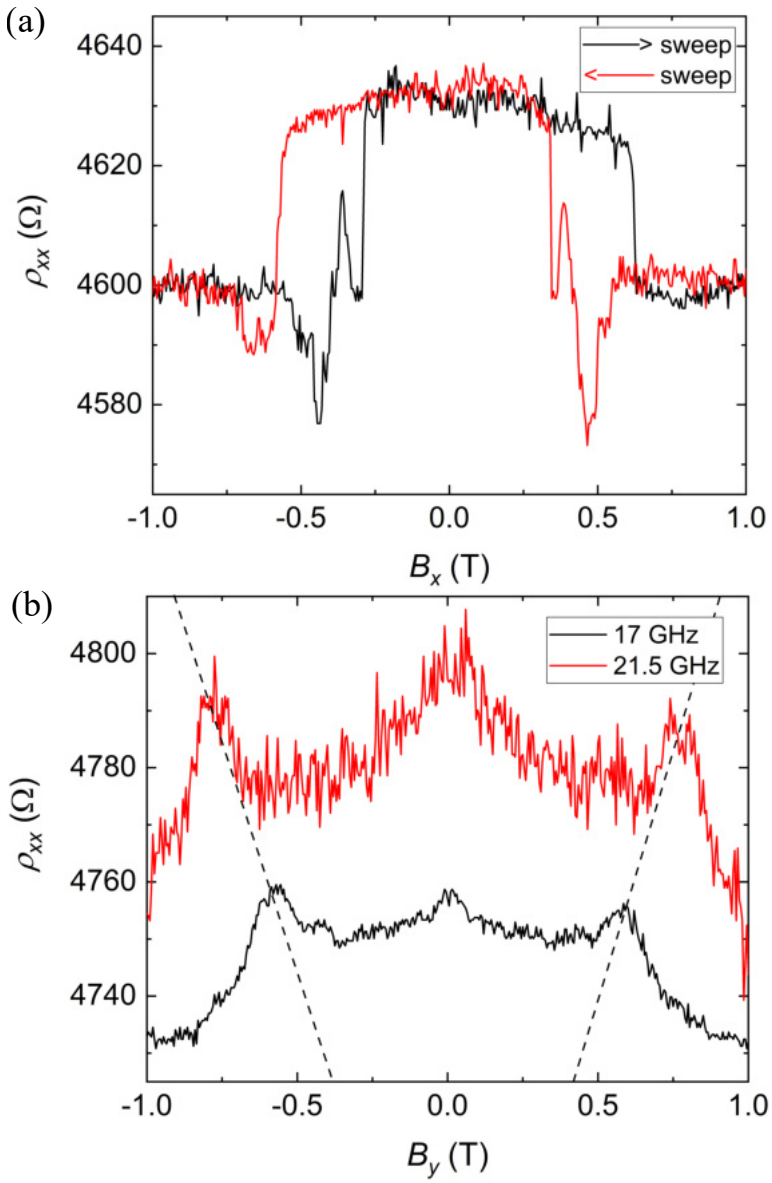

Fig. 7.10. Magnetoresistance under microwave irradiation for the x- and y-directions of the external magnetic field, respectively. The data are recorded at $T = 1.4\,\mathrm{K}$, $V_g = 0$ and a radiation power of 19 dBm. **(a)** The applied microwave frequency is 15 GHz. Two resistivity levels appear as well as a clear hysteresis. The critical field of the resistivity change is independent of frequency [110] and no ESR signal is observed. **(b)** Two different frequencies exhibit ESR features and a WL peak. The peak positions correspond to $g_y \approx 2$, which is consistent with the data of Chapter 6. Speculations about the origin of the observed features in (a) and (b) can be found in the main text.

magnetic moments of the nanoparticles are either aligned perpendicularly to the spin ($|B_x| \lesssim 0.5\,\mathrm{T}$) or parallel ($|B_x| \gtrsim 0.5\,\mathrm{T}$). The perpendicular configuration hinders transport, which can be observed as a rise in resistivity. Note that these speculations are preliminary and demand for a thorough investigation in the future.

In the y-direction, the hysteresis vanishes and instead, a WL peak appears at zero field, as well as the ordinary spin resonance which is symmetric in B_y (see Fig. 7.10b). The presented resonance positions correspond to a g-factor of $g_y \approx 2$, which is consistent with the results of Chapter 6. The absence of the WL feature without radiation (see Fig. 7.9b) indicates that there might be a remnant magnetic field even when $B_y = 0$ due to the nanoparticles. When the microwaves are switched on, the remnant field seems to disappear, or might rather be averaged to zero over time due to the antenna tipping the magnetic moments of the nanoparticles repeatedly, hence the reappearance of the WL peak.

The different behavior for x- and y-directions could be explained in terms of the relative orientations of magnetic field and the microwave field, generated by the antenna. When B_x is applied, the AC field is perpendicular to the magnetic moments and can act as a "tipping" field for the magnetic orientation. In contrast, for sufficiently high B_y the nanoparticles are collinear with the microwave field and stay unaffected. However, similar to the x-direction of the magnetic field, many questions remain unanswered and additional experimental proof is required to establish a consistent theoretical model.

8 Conclusions and Outlook

The magnetoresistance and resistively-detected electron spin resonance measurements presented in this work shed light on various intrinsic properties of graphene. The ESR experiments with the magnetic field perpendicular to the sample plane were employed to measure the band gap in graphene of $\Delta_I = 42.2\,\mu\text{eV}$, which is caused by intrinsic spin-orbit coupling. The size of this gap is in the theoretically predicted range of $1\,\mu\text{eV} - 100\,\mu\text{eV}$ [11, 13–17]. It was shown that graphene undergoes a phase transition from a spin-Hall insulator to the semi-metallic state at a critical magnetic field of $|B| = 0.38\,\text{T}$. The g-factor was extracted as $g_z = 1.95$ and was found to be independent of the applied back-gate voltage. In the presented theory, numerical tight binding calculations were performed by M. Prada, illustrating the band structure of graphene close to the Dirac points and the spin transitions of the charge carriers involved in the experimental observations. These findings have been published recently as a peer-reviewed journal article [21].

The effective g-factor of graphene was determined in dependence of the magnetic field angle, and a significant variation between $g_x = 1.81$ and $g_y = 2.03$ for the x- and y-directions of the **B**-field was found. With these values, a microscopic model was established by M. Prada, and employed to extract the mixing parameter of the p- and d-orbitals in graphene $\alpha/\epsilon_d = 0.1581$ as well as the atomic spin-orbit coupling $\chi_d = 0.42\,\text{meV}$. These values had previously been estimated via density functional theory to be $(\alpha/\epsilon_d)_{est.} \approx 0.0871$ and $\chi_{d,est.} \approx 0.8\,\text{meV}$, respectively [16]. The presented results constitute an improvement of the theoretical predictions and contribute to the basic understanding of graphene. The presented theory is a work in progress which might reveal the role of Rashba and other spin-orbit coupling mechanisms in graphene. The findings from the angle-dependent ESR measurements are currently prepared for publication.

A sample with magnetic nanoparticles between substrate and graphene was prepared in collaboration with the group of Prof. Oepen [101, 102]. In magnetoresistance measurements, it was found to exhibit an unusually high charge carrier density of $n = 1.86 \cdot 10^{13}\,\text{cm}^{-2}$. With the magnetic field perpendicular to the sample plane, the ESR signal was greatly improved, which is probably

related to a local spin polarization in the graphene layer in the vicinity of the magnetic nanodots. The magnetoresistance measurements with an in-plane **B**-field showed an unexpected and direction-dependent response to microwave radiation. The microwave signal appears to induce switching in the magnetization of the magnetic nanoparticles, which can be observed in the resistivity of the graphene. An in-depth analysis can be found in the Master's thesis by T. Anlauf [110].

The presented measurements for graphene on magnetic nanoparticles offer a rich playground for future spin-related experiments. ESR studies with a high density of data points as well as high accuracy can be performed in order to determine the effective magnetic field of the nanoparticles, which should reveal a finite x-intercept in the linear resonance peak fit. Varying densities of nanoparticles on the substrate should be investigated in order to determine whether they could act as a spin-barrier for the charge carriers. Data acquisition for the current sample and the preparation for the abovementioned experiments are ongoing.

Complementary experiments can be performed with the available experimental systems. Prometheus has the capability of inducing a tunable strain in the graphene using a piezo-electric motor. The strain should impact the intrinsic spin-orbit coupling and thus, allow for the precise control of the band gap in graphene. First results are detailed in the thesis of J. L. Riemann [111]. Related experiments on Bi_2Se_3 topological insulator nanowires have been performed by C. Schindler, where the strain was demonstrated to shift the position of the Dirac point in the band structure. The details can be found in our publication [22], as multiple additional chapters would have been beyond the scope of this work.

Bibliography

[1] K. S. Novoselov. *Electric Field Effect in Atomically Thin Carbon Films*. Science **306**, 666–669 (2004).

[2] K. S. Novoselov, D. Jiang, F. Schedin, T. J. Booth, V. V. Khotkevich, S. V. Morozov, and A. K. Geim. *Two-dimensional atomic crystals*. Proceedings of the National Academy of Sciences **102**, 10451–10453 (2005).

[3] L. Zou, L. Wang, Y. Wu, C. Ma, S. Yu, and X. Liu. *Trends Analysis of Graphene Research and Development*. Journal of Data and Information Science **3**, 82–100 (2018).

[4] P. R. Wallace. *The Band Theory of Graphite*. Physical Review **71**, 622–634 (1947).

[5] J. W. McClure. *Diamagnetism of Graphite*. Physical Review **104**, 666–671 (1956).

[6] J. C. Slonczewski and P. R. Weiss. *Band Structure of Graphite*. Physical Review **109**, 272–279 (1958).

[7] K. S. Novoselov, A. K. Geim, S. V. Morozov, D. Jiang, M. I. Katsnelson, I. V. Grigorieva, S. V. Dubonos, and A. A. Firsov. *Two-dimensional gas of massless Dirac fermions in graphene*. Nature **438**, 197–200 (2005).

[8] Y. B. Zhang, Y. W. Tan, H. L. Stormer, and P. Kim. *Experimental observation of the quantum Hall effect and Berry's phase in graphene*. Nature **438**, 201–204 (2005).

[9] K. S. Novoselov, Z. Jiang, Y. Zhang, S. V. Morozov, H. L. Stormer, U. Zeitler, J. C. Maan, G. S. Boebinger, P. Kim, and A. K. Geim. *Room-Temperature Quantum Hall Effect in Graphene*. Science **315**, 1379–1379 (2007).

[10] Z. Jiang, Y. Zhang, Y. W. Tan, H. L. Stormer, and P. Kim. *Quantum Hall effect in graphene*. Solid State Communications **143**, 14–19 (2007).

[11] C. L. Kane and E. J. Mele. *Quantum Spin Hall Effect in Graphene*. Physical Review Letters **95**, 226801 (2005).

[12] C. L. Kane and E. J. Mele. *Z2 Topological Order and the Quantum Spin Hall Effect*. Physical Review Letters **95**, 146802 (2005).

[13] H. Min, J. E. Hill, N. A. Sinitsyn, B. R. Sahu, L. Kleinman, and A. H. MacDonald. *Intrinsic and Rashba spin-orbit interactions in graphene sheets*. Physical Review B **74**, 165310 (2006).

[14] Y. Yao, F. Ye, X.-L. Qi, S.-C. Zhang, and Z. Fang. *Spin-orbit gap of graphene: First-principles calculations*. Physical Review B **75**, 041401 (2007).

[15] M. Gmitra, S. Konschuh, C. Ertler, C. Ambrosch-Draxl, and J. Fabian. *Band-structure topologies of graphene: Spin-orbit coupling effects from first principles*. Physical Review B **80**, 235431 (2009).

[16] S. Konschuh, M. Gmitra, and J. Fabian. *Tight-binding theory of the spin-orbit coupling in graphene*. Physical Review B **82**, 245412 (2010).

[17] J. C. Boettger and S. B. Trickey. *First-principles calculation of the spin-orbit splitting in graphene*. Physical Review B - Condensed Matter and Materials Physics **75**, 6–8 (2007).

[18] R. G. Mani, J. Hankinson, C. Berger, and W. A. De Heer. *Observation of resistively detected hole spin resonance and zero-field pseudo-spin splitting in epitaxial graphene*. Nature Communications **3**, 996 (2012).

[19] T. J. Lyon, J. Sichau, A. Dorn, A. Zurutuza, A. Pesquera, A. Centeno, and R. H. Blick. *Upscaling high-quality CVD graphene devices to 100 micron-scale and beyond*. Applied Physics Letters **110**, 113502 (2017).

[20] T. J. Lyon, J. Sichau, A. Dorn, A. Centeno, A. Pesquera, A. Zurutuza, and R. H. Blick. *Probing Electron Spin Resonance in Monolayer Graphene*. Physical Review Letters **119**, 066802 (2017).

[21] J. Sichau, M. Prada, T. Anlauf, T. J. Lyon, B. Bosnjak, L. Tiemann, and R. H. Blick. *Resonance Microwave Measurements of an Intrinsic Spin-Orbit Coupling Gap in Graphene: A Possible Indication of a Topological State*. Physical Review Letters **122**, 046403 (2019).

[22] C. Schindler, C. Wiegand, J. Sichau, L. Tiemann, K. Nielsch, R. Zierold, and R. H. Blick. *Strain-induced Dirac state shift in topological insulator Bi 2 Se 3 nanowires*. Applied Physics Letters **111**, 171601 (2017).

[23] A. H. Castro Neto, F. Guinea, N. M. R. Peres, K. S. Novoselov, and A. K. Geim. *The electronic properties of graphene*. Reviews of Modern Physics **81**, 109–162 (2009).

[24] S. Reich, J. Maultzsch, C. Thomsen, and P. Ordejón. *Tight-binding description of graphene*. Physical Review B - Condensed Matter and Materials Physics **66**, 354121–354125 (2002).

[25] J. P. Hobson and W. A. Nierenberg. *The Statistics of a Two-Dimensional, Hexagonal Net*. Physical Review **89**, 662–662 (1953).

[26] M. I. Katsnelson. *Graphene: Carbon in Two Dimensions*. Cambridge University Press (2012). ISBN: 9780521195409.

[27] M. Z. Hasan and C. L. Kane. *Colloquium : Topological insulators*. Reviews of Modern Physics **82**, 3045–3067 (2010).

[28] A. K. Geim and K. S. Novoselov. *The rise of graphene*. Nature Materials **6**, 183–191 (2007).

[29] M. O. Goerbig. *Electronic properties of graphene in a strong magnetic field*. Reviews of Modern Physics **83**, (2011).

[30] G. P. Mikitik and Y. V. Sharlai. *Manifestation of berry's phase in metal physics*. Physical Review Letters **82**, 2147–2150 (1999).

[31] H. Suzuura and T. Ando. *Crossover from Symplectic to Orthogonal Class in a Two-Dimensional Honeycomb Lattice*. Physical Review Letters **89**, 266603 (2002).

[32] M. I. Katsnelson, K. S. Novoselov, and A. K. Geim. *Chiral tunnelling and the Klein paradox in graphene*. Nature Physics **2**, 620–625 (2006).

[33] M. I. Katsnelson. *Zitterbewegung, chirality, and minimal conductivity in graphene*. European Physical Journal B **51**, 157–160 (2006).

[34] E. V. Castro, M. P. López-Sancho, and M. A. H. Vozmediano. *Pinning and switching of magnetic moments in bilayer graphene*. New Journal of Physics **11**, 095017 (2009).

[35] Y. A. Bychkov and E. I. Rashba. *Oscillatory effects and the magnetic susceptibility of carriers in inversion layers*. Journal of Physics C: Solid State Physics **17**, 6039–6045 (1984).

[36] X. Jia, J. Campos-Delgado, M. Terrones, V. Meunier, and M. S. Dresselhaus. *Graphene edges: a review of their fabrication and characterization*. Nanoscale **3**, 86–95 (2011).

[37] R. Winkler and H. Deshpande. *Effective Hamiltonian for protected edge states in graphene*. Physical Review B **95**, 235312 (2017).

[38] K. Nakada, M. Fujita, G. Dresselhaus, and M. S. Dresselhaus. *Edge state in graphene ribbons: Nanometer size effect and edge shape dependence*. Physical Review B **54**, 17954–17961 (1996).

[39] M. Fujita, K. Wakabayashi, K. Nakada, and K. Kusakabe. *Peculiar Localized State at Zigzag Graphite Edge*. Journal of the Physical Society of Japan **65**, 1920–1923 (1996).

[40] S. M.-M. Dubois, Z. Zanolli, X. Declerck, and J.-C. Charlier. *Electronic properties and quantum transport in Graphene-based nanostructures*. The European Physical Journal B **72**, 1–24 (2009).

[41] T. Espinosa-Ortega, I. A. Luk'yanchuk, and Y. G. Rubo. *Density of states in randomly shaped graphene quantum dots*. Superlattices and Microstructures **49**, 283–287 (2011).

[42] M. A. Vozmediano, M. P. López-Sancho, T. Stauber, and F. Guinea. *Local defects and ferromagnetism in graphene layers*. Physical Review B - Condensed Matter and Materials Physics **72**, 17–19 (2005).

[43] A. Carpio, L. L. Bonilla, F. de Juan, and M. A. H. Vozmediano. *Dislocations in graphene*. New Journal of Physics **10**, 053021 (2008).

[44] N. M. R. Peres, L. Yang, and S.-W. Tsai. *Local density of states and scanning tunneling currents in graphene*. New Journal of Physics **11**, 095007 (2009).

[45] T. Stegmann and N. Szpak. *Current flow paths in deformed graphene: from quantum transport to classical trajectories in curved space*. New Journal of Physics **18**, 053016 (2016).

[46] T. J. Lyon. *An Investigation of the g-factor of Graphene*. PhD thesis. University of Wisconsin-Madison (2017)

[47] S. Adam, E. H. Hwang, V. M. Galitski, and S. Das Sarma. *A self-consistent theory for graphene transport*. Proceedings of the National Academy of Sciences **104**, 18392–18397 (2007).

[48] J. Xia, F. Chen, J. Li, and N. Tao. *Measurement of the quantum capacitance of graphene*. Nature Nanotechnology **4**, 505–509 (2009).

[49] K. Von Klitzing. *The quantized Hall effect*. Reviews of Modern Physics **58**, 519–531 (1986).

[50] A. S. Mayorov, R. V. Gorbachev, S. V. Morozov, L. Britnell, R. Jalil, L. A. Ponomarenko, P. Blake, K. S. Novoselov, K. Watanabe, T. Taniguchi, and A. K. Geim. *Micrometer-Scale Ballistic Transport in Encapsulated Graphene at Room Temperature*. Nano Letters **11**, 2396–2399 (2011).

[51] F. Pizzocchero, L. Gammelgaard, B. S. Jessen, J. M. Caridad, L. Wang, J. Hone, P. Bøggild, and T. J. Booth. *The hot pick-up technique for batch assembly of van der Waals heterostructures*. Nature Communications **7**, (2016).

[52] T. Stauber, N. M. R. Peres, and F. Guinea. *Electronic transport in graphene: A semiclassical approach including midgap states*. Physical Review B **76**, 205423 (2007).

[53] P. M. Ostrovsky, I. V. Gornyi, and A. D. Mirlin. *Electron transport in disordered graphene*. Physical Review B **74**, 235443 (2006).

[54] V. E. Calado, S.-E. Zhu, S. Goswami, Q. Xu, K. Watanabe, T. Taniguchi, G. C. A. M. Janssen, and L. M. K. Vandersypen. *Ballistic transport in graphene grown by chemical vapor deposition*. Applied Physics Letters **104**, 023103 (2014).

[55] O. M. Nayfeh, S. Kilpatrick, and M. Dubey. *Majority and minority carrier mobility behavior and device modeling of doped CVD monolayer graphene transistors*. IEEE (2010).

[56] M. Katsnelson and A. Geim. *Electron scattering on microscopic corrugations in graphene*. Philosophical Transactions of the Royal Society A: Mathematical, Physical and Engineering Sciences **366**, 195–204 (2008).

[57] E.-A. Kim and A. H. Castro Neto. *Graphene as an electronic membrane*. EPL (Europhysics Letters) **84**, 57007 (2008).

[58] V. P. Gusynin and S. G. Sharapov. *Unconventional integer quantum hall effect in graphene*. Physical Review Letters **95**, 2–5 (2005).

[59] J. Martin, N. Akerman, G. Ulbricht, T. Lohmann, J. H. Smet, K. Von Klitzing, and A. Yacoby. *Observation of electron-hole puddles in graphene using a scanning single-electron transistor*. Nature Physics **4**, 144–148 (2008).

[60] S. Wiedmann, H. J. van Elferen, E. V. Kurganova, M. I. Katsnelson, A. J. M. Giesbers, A. Veligura, B. J. van Wees, R. V. Gorbachev, K. S. Novoselov, J. C. Maan, and U. Zeitler. *Coexistence of electron and hole transport in graphene*. Physical Review B **84**, 115314 (2011).

[61] M. Hilke, M. Massicotte, E. Whiteway, and V. Yu. *Weak Localization in Graphene: Theory, Simulations and Experiments*. .

[62] S. Hikami, A. I. Larkin, and Y. Nagaoka. *Spin-Orbit Interaction and Magnetoresistance in the Two Dimensional Random System*. Progress of Theoretical Physics **63**, 707–710 (1980).

[63] B. L. Altshuler, D. Khmel'nitzkii, A. I. Larkin, and P. A. Lee. *Magnetoresistance and Hall effect in a disordered two-dimensional electron gas*. Physical Review B **22**, 5142–5153 (1980).

[64] P. A. Lee and T. V. Ramakrishnan. *Disordered electronic systems*. Reviews of Modern Physics **57**, 287–337 (1985).

[65] C. W. J. Beenakker and H. van Houten. *Boundary scattering and weak localization of electrons in a magnetic field*. Physical Review B **38**, 3232–3240 (1988).

[66] F. V. Tikhonenko, A. A. Kozikov, A. K. Savchenko, and R. V. Gorbachev. *Transition between Electron Localization and Antilocalization in Graphene*. Physical Review Letters **103**, 226801 (2009).

[67] E. McCann, K. Kechedzhi, V. I. Fal'ko, H. Suzuura, T. Ando, and B. L. Altshuler. *Weak-Localization Magnetoresistance and Valley Symmetry in Graphene*. Physical Review Letters **97**, 146805 (2006).

[68] M. A. Augustyniak-Jabokow, K. Tadyszak, M. Makowiak, and S. Lijewski. *ESR study of spin relaxation in graphene*. Chemical Physics Letters **557**, 118–122 (2013).

[69] T. Ando and Y. Uemura. *Theory of Oscillatory g Factor in an MOS Inversion Layer under Strong Magnetic Fields*. Journal of the Physical Society of Japan **37**, 1044–1052 (1974).

[70] R. J. Nicholas, R. J. Haug, K. v. Klitzing, and G. Weimann. *Exchange enhancement of the spin splitting in a GaAs-GaxAl1-xAs heterojunction*. Physical Review B **37**, 1294–1302 (1988).

[71] W. Desrat, F. Giazotto, V. Pellegrini, F. Beltram, F. Capotondi, G. Biasiol, L. Sorba, and D. K. Maude. *Magnetotransport in high-g-factor low-density two-dimensional electron systems confined in In0.75Ga0.25As/In0.75Al0.25As quantum wells*. Physical Review B - Condensed Matter and Materials Physics **69**, (2004).

[72] D. Huertas-Hernando, F. Guinea, and A. Brataas. *Spin-orbit-mediated spin relaxation in graphene*. Physical Review Letters **103**, 1–4 (2009).

[73] B. Trauzettel, D. V. Bulaev, D. Loss, and G. Burkard. *Spin qubits in graphene quantum dots*. Nature Physics **3**, 192–196 (2007).

[74] N. Tombros, C. Jozsa, M. Popinciuc, H. T. Jonkman, and B. J. Van Wees. *Electronic spin transport and spin precession in single graphene layers at room temperature*. Nature **448**, 571–574 (2007).

[75] W. Han, K. Pi, W. Bao, K. M. McCreary, Y. Li, W. H. Wang, C. N. Lau, and R. K. Kawakami. *Electrical detection of spin precession in single layer graphene spin valves with transparent contacts*. Applied Physics Letters **94**, 2007–2010 (2009).

[76] C. Józsa, T. Maassen, M. Popinciuc, P. J. Zomer, A. Veligura, H. T. Jonkman, and B. J. Van Wees. *Linear scaling between momentum and spin scattering in graphene*. Physical Review B - Condensed Matter and Materials Physics **80**, 1–4 (2009).

[77] M. Popinciuc, C. Józsa, P. J. Zomer, N. Tombros, A. Veligura, H. T. Jonkman, and B. J. van Wees. *Electronic spin transport in graphene field-effect transistors*. Physical Review B **80**, 214427 (2009).

[78] K. Pi, W. Han, K. M. McCreary, A. G. Swartz, Y. Li, and R. K. Kawakami. *Manipulation of spin transport in graphene by surface chemical doping*. Physical Review Letters **104**, 1–4 (2010).

[79] W. Han and R. K. Kawakami. *Spin relaxation in single-layer and bilayer graphene*. Physical Review Letters **107**, 1–4 (2011).

[80] S. Jo, D.-K. Ki, D. Jeong, H.-J. Lee, and S. Kettemann. *Spin relaxation properties in graphene due to its linear dispersion*. Physical Review B **84**, 075453 (2011).

[81] W. Han, R. K. Kawakami, M. Gmitra, and J. Fabian. *Graphene spintronics*. Nature Nanotechnology **9**, 794–807 (2014).

[82] D. V. Tuan, F. Ortmann, D. Soriano, S. O. Valenzuela, and S. Roche. *Pseudospin-driven spin relaxation mechanism in graphene*. Nature Physics **10**, 857–863 (2014).

[83] S. Roche and S. O. Valenzuela. *Graphene spintronics: Puzzling controversies and challenges for spin manipulation*. Journal of Physics D: Applied Physics **47**, (2014).

[84] C. Ertler, S. Konschuh, M. Gmitra, and J. Fabian. *Electron spin relaxation in graphene: the role of the substrate*. .

[85] S. Fratini, D. Gosálbez-Martínez, P. Merodio Cámara, and J. Fernández-Rossier. *Anisotropic intrinsic spin relaxation in graphene due to flexural distortions*. Physical Review B - Condensed Matter and Materials Physics **88**, 1–7 (2013).

[86] B. Dóra, F. Murányi, and F. Simon. *Electron spin dynamics and electron spin resonance in graphene*. EPL (Europhysics Letters) **92**, 17002 (2010).

[87] T. Y. Yang, J. Balakrishnan, F. Volmer, A. Avsar, M. Jaiswal, J. Samm, S. R. Ali, A. Pachoud, M. Zeng, M. Popinciuc, G. Güntherodt, B. Beschoten, and B. Özyilmaz. *Observation of long spin-relaxation times in bilayer graphene at room temperature*. Physical Review Letters **107**, 5–8 (2011).

[88] T. Maassen, F. K. Dejene, M. H. D. Guimarães, C. Józsa, and B. J. van Wees. *Comparison between charge and spin transport in few layer graphene*. .

[89] F. Volmer, M. Drögeler, E. Maynicke, N. Von Den Driesch, M. L. Boschen, G. Güntherodt, and B. Beschoten. *Role of MgO barriers for spin and charge transport in Co/MgO/graphene nonlocal spin-valve devices*. Physical Review B - Condensed Matter and Materials Physics **88**, 1–5 (2013).

[90] P. J. Zomer, M. H. D. Guimarães, N. Tombros, and B. J. Van Wees. *Long-distance spin transport in high-mobility graphene on hexagonal boron nitride*. Physical Review B - Condensed Matter and Materials Physics **86**, 2–5 (2012).

[91] T. Maassen, J. J. Van Den Berg, E. H. Huisman, H. Dijkstra, F. Fromm, T. Seyller, and B. J. Van Wees. *Localized states influence spin transport in epitaxial graphene*. Physical Review Letters **110**, 1–5 (2013).

[92] I. Neumann, J. Van De Vondel, G. Bridoux, M. V. Costache, F. Alzina, C. M. Torres, and S. O. Valenzuela. *Electrical detection of spin precession in freely suspended graphene spin valves on cross-linked poly(methyl methacrylate)*. Small **9**, 156–160 (2013).

[93] M. H. D. Guimarães, A. Veligura, P. J. Zomer, T. Maassen, I. J. Vera-Marun, N. Tombros, and B. J. Van Wees. *Spin transport in high-quality suspended graphene devices*. Nano Letters **12**, 3512–3517 (2012).

[94] W. Han, K. M. McCreary, K. Pi, W. H. Wang, Y. Li, H. Wen, J. R. Chen, and R. K. Kawakami. *Spin transport and relaxation in graphene*. Journal of Magnetism and Magnetic Materials **324**, 369–381 (2012).

[95] M. B. Lundeberg, R. Yang, J. Renard, and J. A. Folk. *Defect-mediated spin relaxation and dephasing in graphene*. Physical Review Letters **110**, 1–5 (2013).

[96] D. Kochan, M. Gmitra, and J. Fabian. *Spin relaxation mechanism in graphene: Resonant scattering by magnetic impurities*. Physical Review Letters **112**, 1–5 (2014).

[97] X. Liang, B. A. Sperling, I. Calizo, G. Cheng, C. A. Hacker, Q. Zhang, Y. Obeng, K. Yan, H. Peng, Q. Li, X. Zhu, H. Yuan, A. R. Hight Walker, Z. Liu, L.-m. Peng, and C. A. Richter. *Toward Clean and Crackless Transfer of Graphene*. ACS Nano **5**, 9144–9153 (2011).

[98] URL: `www.graphenea.com` (accessed on 11.9.2018)

[99] K. Nagashio, T. Yamashita, T. Nishimura, K. Kita, and A. Toriumi. *Electrical transport properties of graphene on SiO 2 with specific surface structures*. Journal of Applied Physics **110**, 024513 (2011).

[100] M. Her, R. Beams, and L. Novotny. *Graphene transfer with reduced residue*. Physics Letters A **377**, 1455–1458 (2013).

[101] H. Stillrich, A. Frömsdorf, S. Pütter, S. Förster, and H. P. Oepen. *Sub-20 nm Magnetic Dots with Perpendicular Magnetic Anisotropy*. Advanced Functional Materials **18**, 76–81 (2008).

[102] A. Neumann, N. Franz, G. Hoffmann, A. Meyer, and H. P. Oepen. *Fabrication of Magnetic Co/Pt Nanodots Utilizing Filled Diblock Copolymers*. The Open Surface Science Journal **4**, 55–64 (2012).

[103] *Liquid He Phase Diagrams.* URL: `https://superfluid.cz/supratekutost` (accessed on 10.10.2018)

[104] *MODEL SR830 DSP Lock-In Amplifier.* URL: `https://www.thinksrs.com/downloads/pdfs/manuals/SR830m.pdf` (accessed on 11.10.2018)

[105] S. Russo, M. F. Craciun, M. Yamamoto, A. F. Morpurgo, and S. Tarucha. *Contact resistance in graphene-based devices*. Physica E: Low-Dimensional Systems and Nanostructures **42**, 677–679 (2010).

[106] Q. Yu, L. A. Jauregui, W. Wu, R. Colby, J. Tian, Z. Su, H. Cao, Z. Liu, D. Pandey, D. Wei, T. F. Chung, P. Peng, N. P. Guisinger, E. A. Stach, J. Bao, S.-S. Pei, and Y. P. Chen. *Control and characterization of individual grains and grain boundaries in graphene grown by chemical vapour deposition*. Nature Materials **10**, 443–449 (2011).

[107] J. C. Slater and G. F. Koster. *Simplified LCAO Method for the Periodic Potential Problem*. Physical Review **94**, 1498–1524 (1954).

[108] J. K. Asbóth, L. Oroszlány, and A. Pályi. *A Short Course on Topological Insulators: Band-structure topology and edge states in one and two dimensions*. .

[109] P. Staeck. *Untersuchungen zur Wechselwirkung von magnetischen Nanostrukturen mittels Magnetotransport*. PhD thesis. (2017)

[110] T. Anlauf. *Microwave Studies of Graphene: The Influence of Spin-Orbit Coupling and Magnetism on Electron Spin Resonance*. Master's Thesis. Universität Hamburg (2019)

[111] J. L. Riemann. *Influence of Symmetry Breaking through Mechanical Deformation on the Transport Properties of 2D Systems*. Master's Thesis. Universität Hamburg (2019)

Publications

[1] J. Sichau, M. Prada, T. Anlauf, T. J. Lyon, B. Bosnjak, L. Tiemann, and R. H. Blick. *Resonance Microwave Measurements of an Intrinsic Spin-Orbit Coupling Gap in Graphene: A Possible Indication of a Topological State*. Physical Review Letters **122**, 046403 (2019).

[2] T. J. Lyon, J. Sichau, A. Dorn, A. Centeno, A. Pesquera, A. Zurutuza, and R. H. Blick. *Probing Electron Spin Resonance in Monolayer Graphene*. Physical Review Letters **119**, 066802 (2017).

[3] T. J. Lyon, J. Sichau, A. Dorn, A. Zurutuza, A. Pesquera, A. Centeno, and R. H. Blick. *Upscaling high-quality CVD graphene devices to 100 micron-scale and beyond*. Applied Physics Letters **110**, 113502 (2017).

[4] C. Schindler, C. Wiegand, J. Sichau, L. Tiemann, K. Nielsch, R. Zierold, and R. H. Blick. *Strain-induced Dirac state shift in topological insulator Bi2Se3nanowires*. Applied Physics Letters **111**, 171601 (2017).

Invited Talks

[1] J. Sichau, M. Prada, T. J. Lyon, B. Bosnjak, L. Tiemann, C. Schindler, C. Wiegand, K. Nielsch, R. Zierold, and R. H. Blick. *Experiments on Nanomembranes and 2D Materials*. 4th Condensed Matter Summer School - Interfaces: from Spins to Nanomembranes, Wroclaw, Poland (2018).

[2] J. Sichau, M. Prada, T. J. Lyon, B. Bosnjak, L. Tiemann, and R. H. Blick. *Resistively-detected Zero-Field Splitting due to Intrinsic Spin-Orbit Coupling in Graphene*. Electronic Properties of 2D Systems (EP2DS), Pennsylvania State University, USA (2017).

Contributed Talks

[1] J. Sichau, T. J. Lyon, and R. H. Blick. *Mechanically Modulated Graphene for THz-Nanoelectronics*. DPG-Frühjahrstagung, Berlin, Germany (2015).

Contributed Posters

[1] C. Schindler, C. Wiegand, J. Sichau, L. Tiemann, K. Nielsch, R. Zierold, and R. H. Blick. *Strain-induced Dirac State Shift in Bi 2 Se 3-Nanowires*. IEEE Magnetic Frontiers: Topological Insulators, Nancy, France (2017).

Danksagung

Ich möchte mich zuallererst bei Prof. Robert H. Blick für die stetige Unterstützung und das Vertrauen in meine Arbeit bedanken. Durch sein Engagement, seine Ideen und unsere häufigen Diskussionen ist mein Beitrag zu diesem Projekt überhaupt erst möglich geworden. Außerdem möchte ich mich bei Lars Tiemann bedanken, da ohne seine Expertise, Erfahrung und seine enorme Begeisterung und Einsatzbereitschaft nur die Hälfte aller Experimente hätten durchgeführt werden können. Meine Dankbarkeit gilt zudem Marta Prada, die immer ein offenes Ohr für Fragen hat und sich stets Zeit genommen hat, ihre Theorien ausführlich und geduldig zu erklären. Selbstverständlich ist ihr Beitrag zu den theoretischen Kapiteln dieser Arbeit unersetzlich. Ich möchte außerdem den Gutachtern und der Prüfungskomission meinen Dank dafür ausprechen, dass sie sich die Zeit nehmen, meine Dissertation zu lesen und zu bewerten. Timothy Lyon hat damals als Betreuer meiner Masterarbeit überhaupt erst die Begeisterung am Thema Graphen in mir geweckt und mir die grundlegenden Fähigkeiten beigebracht, um erfolgreich an meinem Doktorthema forschen zu können. Bojan Bosnjak und Cornelius Fendler waren meine langjährigsten Begleiter auf dieser Reise und haben sich sowohl professionell als auch zwischenmenschlich meinen allergrößten Respekt verdient. Bedanken möchte ich mich auch bei meinen ehemaligen Bachelor- und Masterstudenten, die ich betreuen durfte und die mit ihrer Arbeit einen großen Beitrag zu dieser Dissertation geleistet haben: Nick Guse, Clemens Schindler, Leonard Riemann und Tim Anlauf. Die technischen Mitarbeiter und Kollegen haben ein besonderes Lob verdient, da sie stets alles getan haben, damit die Geräte einwandtfrei funktionieren und der Forschung nichts im Wege steht. Allen anderen Postdocs und Doktoranden möchte ich für die Hilfe bei kleinen alltäglichen Problemen und die moralische Unterstützung danken, und natürlich für die schönen Abende bei Gruppenaktivitäten. Nicht zuletzt möchte ich mich herzlich bei meiner Famile und allen Freunden bedanken. Sie haben mich immer unterstützt und sie sind der Mittelpunkt meines Lebens.

Eidesstattliche Versicherung / Declaration on Oath

Hiermit versichere ich an Eides statt, die vorliegende Dissertationsschrift selbst verfasst und keine anderen als die angegebenen Hilfsmittel und Quellen benutzt zu haben.

Die eingereichte schriftliche Fassung entspricht der auf dem elektronischen Speichermedium.

Die Dissertation wurde in der vorgelegten oder einer ähnlichen Form nicht schon einmal in einem früheren Promotionsverfahren angenommen oder als ungenügend beurteilt.

Hamburg, den 10.05.2019

_____

Jonas Sichau